INFORMATION TO USERS

This manuscript has been reproduced from the microfilm master. UMI films the text directly from the original or copy submitted. Thus, some thesis and dissertation copies are in typewriter face, while others may be from any type of computer printer.

The quality of this reproduction is dependent upon the quality of the copy submitted. Broken or indistinct print, colored or poor quality illustrations and photographs, print bleedthrough, substandard margins, and improper alignment can adversely affect reproduction.

In the unlikely event that the author did not send UMI a complete manuscript and there are missing pages, these will be noted. Also, if unauthorized copyright material had to be removed, a note will indicate the deletion.

Oversize materials (e.g., maps, drawings, charts) are reproduced by sectioning the original, beginning at the upper left-hand corner and continuing from left to right in equal sections with small overlaps. Each original is also photographed in one exposure and is included in reduced form at the back of the book.

Photographs included in the original manuscript have been reproduced xerographically in this copy. Higher quality 6" x 9" black and white photographic prints are available for any photographs or illustrations appearing in this copy for an additional charge. Contact UMI directly to order.

UMI

A Bell & Howell Information Company
300 North Zeeb Road, Ann Arbor MI 48106-1346 USA
313/761-4700 800/521-0600

FIELD THEORY ANALYSIS AND DESIGN OF CIRCULAR WAVEGUIDE COMPONENTS

by

UMA BALAJI
B.E., Madurai Kamaraj University, Madurai, 1985
M.E., Anna University, Madras, 1987

A Dissertation Submitted in Partial Fulfillment of the
Requirements for the Degree of
DOCTOR OF PHILOSOPHY
in the
Department of Electrical and Computer Engineering

We accept this dissertation as conforming
to the required standard

Dr. R. Vahldieck, Supervisor, Dept. of Elect. & Comp. Engg.

Dr. J. Bornemann, Departmental Member, Dept. of Elect. & Comp. Engg.

Dr. W. J. R. Hoefer, Departmental Member, Dept. of Elect. & Comp. Engg.

Dr. S. Dost, Outside Member, Dept. of Mech. Engg.

Dr. J. Uher, External Examiner, Spar Aerospace Limited, Canada

University of Victoria

Supervisor: Dr. R. Vahldieck

ABSTRACT

RF/microwave terrestrial point-to-point and satellite communication systems employ a large number of waveguide components operating at microwave and millimeter wave frequencies. Accurate design of these components for optimum performance of the overall system is critical. To achieve this, computationally efficient and accurate numerical methods are indispensable tools in the design and optimization of components and subsystems.

Among the large variety of potentially suitable numerical methods, the mode matching method in conjunction with the generalized scattering matrix technique has been found to be one of the most reliable and straightforward techniques to design waveguide components. In the past the method has been mainly applied to eigenvalue and scattering problems in rectangular waveguides. In this thesis, the mode matching method is extended to ridge waveguide problems in circular waveguides and thus closes a gap in the literature that has existed for a long time.

The thesis begins with a study of the basic principles of the mode matching method as it is known from rectangular waveguides. These principles are then applied to the analysis of the rectangular ridged and coaxial waveguide, followed by an eigenvalue analysis of ridged circular waveguide. Rather than rectangular ridges, ridges of uniform angular thickness(conically shaped) are used in the circular waveguide to avoid a mixed coordinate system which would render the mode matching method computationally very inefficient. On the other hand, conically shaped ridges are as easy to fabricate as rectangular ridges and are not detrimental to the electrical performance of the component.

The thesis then continues to treat the discontinuity problem at the interface between the empty circular waveguide and ridged circular waveguide. To verify the computed scattering parameters, measurements were performed and good agreement was found. By cascading several discontinuities transformers and evanescent mode filters were designed. A fifth order filter was designed and fabricated and also here good agreement between measured and computed data was found.

The final chapter in the thesis analyses the coupling between orthogonal modes in the presence of an asymmetric discontinuity. Determining the coupling factor between orthogonal modes is an integral part of the design of polarizers and dual mode filters and, for conically shaped ridges, has not been published in the open literature yet. To realize various coupling coefficients, a single or double ridges must be placed at an arbitrary angle to the exciting wave. The mode matching method is extended to include also this case and various convergence tests have been performed to validate the algorithm. As a final example, the algorithm has been applied to design a circular polarizer with two ridges.

Although only two-port problems are treated in this thesis, the basic framework for the mode matching method in circular waveguide has been established and can now be extended to three-port problems. This will be the subject of future work to analyze and design power dividers and orthomode transducers.

Examiners:

Dr. R. Vahldieck, Supervisor, Dept. of Elect. & Comp. Engg.

Dr. J. Bornemann, Departmental Member, Dept. of Elect. & Comp. Engg.

Dr. W. J. R. Hoefer, Departmental Member, Dept. of Elect. & Comp. Engg.

Dr. S. Dost, Outside Member, Dept. of Mechanical Engg.

Dr. J. Uher, External Examiner, Spar Aerospace Limited, Canada

Table of Contents

List of Tables

List of Figures

Acknowledgements

I am very grateful to my supervisor, Dr. R. Vahldieck of the Department of Electrical and Computer Engineering, for the constant encouragement, valuable suggestions and advice as well as continuous support that he provided during the entire duration of this study and research. His remarkable patience and the confidence he has expressed in me have made it possible for me to complete this major undertaking successfully.

I would like to express my acknowledgement and gratitudes to the Canadian Commonwealth Scholarship and Fellowship plan and its various administrators during the period of my study for providing the financial assistance enabling me to undertake this work in the University of Victoria, Canada. I also wish to acknowledge my gratitudes to the Government of India for nominating me as a candidate for this scholarship.

My special thanks to all the members of the examining committee for reviewing my dissertation and determining its value to the field. I would also like to place on record my gratitudes to the many researchers and contributors in the field relevant to this work, from whose research papers and books I have gained considerably and have been able to further improve my understanding of the subject for completing this work.

A word of gratitude to all my friends at the University of Victoria for their encouragement and help during the course of my study. My special thanks to the members of LLiMiC group for their valuable critique, discussions and support.

Finally, I would like to thank my husband and my daughter for their patience, forbearance and encouragement in the pursuit of my academic and career goals. I also wish to thank my mother-in-law and my mother for their support and finally for the encouragement and support that I received from my father and father-in-law, who are both no more but whose blessings, I am sure, are always with me.

Chapter 1

Introduction

Advances in the field of telecommunications have been very rapid and substantial in recent years. Wireless communication is progressing at geometric proportions in response to the massive information exchange that is taking place globally. The active role of radio frequency and microwave components in the telecommunication industry has directly lead to the demands for miniaturized components with improved performance. This is particularly so in satellite systems where specifications are stringent and compactness and light-weights are assets. However, smaller components satisfying the specifications with great accuracy require precision in manufacturing, thus increasing the investment in fabrication greatly. Consequently, the microwave industry relies greatly on efficient computer aided analysis and design tools that eliminate the costly and time consuming cut and try procedure in the fabrication. In addition, the computer aided design process should be capable of handling optimization, as a measure of meeting the stringent specifications.

The microwave components can be either passive or active. The present work focuses on passive components only and therefore the discussions here are limited to issues related to them. A couple of decades ago, passive microwave components such as filters were first designed on the basis of low frequency prototypes. The microwave filter was then realized by replacing the lumped elements in them using distributed elements evaluated from the equivalent circuit approximations. Some of the commercially available software packages like Touchstone, Spice and Super-compact still use this theory for the design of components. Although slowly, depending on the application, field-theory based methods replace network approaches. In microstrip and similar technology, where the electromagnetic field behavior is quasistatic, the equivalent circuit approximations are valid over a broad frequency band. For such cases, the behaviour of the microwave realization is somewhat close to the expected performance. Despite this, a rigorous numerical analysis is still worthwhile in order to predict the exact behavior and a number of them have been developed recently. Also, the complexity of such circuits has increased substantially due to the miniaturization. Proximity of such components during system integration can degrade their performance. Under such circumstances, numerical analysis of the electromagnetic field is a key to meet the design goals.

Unlike for quasistatic cases, the equivalent circuit approximation for waveguides is valid over a narrow band of frequency alone. Hence, this technique of realization of waveguide components from the low frequency prototypes no longer meets, the modern days demands of accurate performance requirements. Over the last two decades, a variety of numerical techniques have been developed for rigorous analysis and design in order to predict accurately the characteristics of the components over a wide band of frequency. Every numerical technique has unique features and merits that make them suitable for certain type of components. The search for the best technique in terms of efficiency and accuracy has continued to be a challenge. The characteristics of waveguide components are sensitive to dimensions, and a numerical technique that can handle optimization of the initial design is an ideal candidate.

The numerical technique used in this work for the design and analysis of waveguide components is called the Mode Matching Method (MMM) and it was first proposed for the solution of rectangular waveguide discontinuities [1]. Subsequently a number of researchers have used this technique to design various waveguide components. The fact that this technique lends itself to the approach of building components from the basic discontinuities in them makes it suitable for handling components composed of many successive discontinuities. Also, an integrated system can be analyzed rigorously once the components in it have been individually analyzed. The most important feature of the MMM is that it is rigorous and yet enables the optimization of the parameters of the initial design.

The first section in this chapter gives a brief overview of the various numerical techniques that can be used to analyze different types of passive microwave components along with their merits and demerits.

This research focuses on the computer aided analysis and design of certain passive components for antenna feeds in satellite systems. The main objective has been to develop computer aided design algorithms for the design of components in circular waveguide technology using a field theoretical approach. Antenna beam forming networks in satellite systems, however, have recently used rectangular coaxial lines (RCL) as an attractive alternative to waveguides due to their smaller size. However, all components in the satellite systems cannot afford the use of RCL as certain components demand for example rectangular, circular or coaxial waveguides, finlines and microstrip lines for various reasons. Each transmission line has its own distinct advantages and disadvantages and preference of one over another depends upon the requirements of the system.

The present work begins with a study on the analysis of some of the well known structures in rectangular waveguides and RCL. The principles of this study have later been utilized to rigorously design components in circular waveguides with good numerical efficiency and using original modeling techniques. Some of the discontinuities discussed in this work are not available in the published literature and hence measurements have been carried out in order to validate the numerical algorithms presented. A detailed outline of the dissertation follows at the end of this chapter. The contribution of this work is in the area of filters, matching networks and polarizers in circular waveguide technology.

1.1 Numerical techniques - An overview

Electric and magnetic fields that are independent of time are called static fields. The basic field problem in electrostatics is to solve Poisson's or Laplace's equation for a potential function that satisfies the boundary condition. For some boundary value problems a direct analytical solution of these is possible while for others a numerical evaluation is the only approach.

For time-varying fields the electric and magnetic fields are described by Maxwell's equations:

$$\nabla \times H = J + \frac{\partial D}{\partial t} \tag{1.1}$$

$$\nabla \times E = -\frac{\partial B}{\partial t} \tag{1.2}$$

$$\nabla \cdot D = \rho \tag{1.3}$$

$$\nabla \cdot B = 0 \tag{1.4}$$

For a homogeneous, isotropic, source free region Maxwell's equations can be reformulated to obtain the Helmoltz equation. The Helmholtz equation is of the form:

$$\nabla^2 \overrightarrow{v} + k^2 \overrightarrow{v} = 0 \tag{1.5}$$

where $k = \omega\sqrt{\mu\epsilon}$. For simple cases, it is possible to determine $\overrightarrow{v}$, the vector potential, from which the field in a homogeneous source free region can be evaluated explicitly. However, for cases where analytic solutions are not possible a numerical evaluation is sought. The numerical techniques themselves can be classified as time domain and frequency domain techniques depending on whether the solution is obtained using spatial discretization (frequency domain method) alone or spatial and time discretization (time domain method) of the Maxwell's equation. Some of these methods are discussed below.

Finite Difference Frequency Domain method (FDFD):

This method is one of the oldest techniques to solve Maxwells equations. The partial differential equations are solved by approximating the derivatives of functions of continuous variables in space, by finite differences using Taylor's series. Thus, the region inside a specified boundary where the electromagnetic field problem needs to be solved is divided into a rectangular mesh. The value of the function at the intersecting points of the mesh, called the nodes, are derived from the value of the functions at the neighboring points. The number of nodes that are used to form the mesh are increased until a convergence in the value of the function is observed. A technique called the Richardsons extrapolation can be used to increase the accuracy of the solutions. Examples of this method have been discussed in [2].

In order to get accurate solutions the number of nodes can be large for certain cases. With an increase in the number of nodes the solution using finite difference technique needs more memory space and computation time. Hence, some problems can become unwieldy using this method. But this method can handle arbitrary and complicated shapes, like curved boundaries using stair step approximations. Because of the general approach to solve problems, commercial packages are available. MAFIA is one such tool to solve electromagnetic field problems.

Finite Difference Time Domain method (FDTD):

This method to solve Maxwells equation was first proposed by Yee [3]. Since the electromagnetic fields vary both in time and space, in this method the partial derivatives with respect to time and space are approximated by finite differences. This method requires a closed region in order to have a finite number of nodes. To handle problems involving open boundaries special absorbing boundary conditions have been derived. Complicated geometries can be handled here too as in FDFD. The frequency domain response is obtained from the time domain characteristics using Fourier transforms. Examples of this method have also been discussed in [2].

Transmission Line Matrix method in Time Domain (TDTLM) and Frequency Domain (FDTLM):

Here, the electromagnetic field problem is converted to a three dimensional equivalent network problem based on Huygen's principle of wave propagation [4]. This method is very general and can handle arbitrarily shaped structures and open boundaries with special absorbing boundary conditions. Once again here too, the computation time and memory space needed can be large for some problems.

The frequency domain TLM method was proposed by Jin and Vahldieck [5]. The same discretization scheme as in the TDTLM is used. However, there is no need to use a Fourier transform to obtain the frequency domain response since the entire algorithm works in the frequency domain. In particular, for narrow band problems, this method is faster than the TDTLM.

Method of Moments (MoM):

This method is more analytical [6] when compared to the above three methods. A sum of basis functions with unknown coefficients is used as an approximate solution to a differential or integral equation. By taking the inner product of the resulting equation with a weighting function, a set of linear equations is obtained which is solved to get the approximate solution to the problem. The choice of basis functions depends on the problem itself and the boundary conditions. The weighting function can be a delta function, pulse function or the same as the basis function. When the choice of the weighting function is the same as the basis functions, the method is also called Galerkin's method. The general MoM is also equivalent to a variational method. A judicious choice of the functions used in this approach can minimize computation time and memory and yet produce numerically accurate results.

Finite Element Method (FEM):

A variational formulation of the differential equation for the specified boundary condition is first obtained. The region of interest is divided into a number of subregions called finite elements. The elements can be any polygon. A triangle is the simplest of the surface elements but it can approximate very well most of the arbitrary shaped structures. In this small element, the function is approximated by a polynomial with unknown coefficients. The choice on the order of the polynomial is an additional degree of freedom while using this method. Rayleigh-Ritz procedure transforms the variational form into a linear system of algebraic equations. The system of equations is then solved to obtain the unknown coefficients of the functions. Using a number of small elements with higher order polynomials to approximate the function, accurate solutions to field problems can be obtained using this method. Eigenvalue analysis of various structures like finlines in rectangular and circular waveguide housings [7], ridged circular waveguides [8,9] have been performed using FEM. The analysis of rectangular waveguide components using FEM is available in [10,11,12]

Since the procedure is general and can be used on arbitrary shapes, commercial CAD packages like HFSS (High Frequency Structure Solver from Hewlett Packard) are available. However, memory space and computational time required are high in this method as well.

Other methods like integral equation method (IEM) [13] and boundary element method (BEM) [14] have been frequently used to solve waveguide discontinuity problems. These methods deal with the discretization of the boundary rather than the whole region of the problem as other discretization approaches do. Hence, they are computationally efficient. However, they require more analytical effort.

Spectral Domain Method (SDM):

This method is well suited for analysis of planar transmission lines such as microstrips, finlines and coplanar waveguides [15]. Basis functions are chosen to approximate the current in the strips on the transmission line. Galerkin's method is then used to yield a homogeneous system of equations to determine the propagation constants, current distribution and the characteristic impedance of the transmission lines. Since the method is highly analytical, the computational efficiency is excellent.

Method of Lines (MoL):

Although this method was available to solve problems in theoretical physics, it was first proposed by Pregla [16] to solve electromagnetic field problems. To solve a two dimensional electromagnetic field problem, discretization of space is applied in one dimension while analytical formulations are possible in the other. This semianalytical procedure saves computation time and memory. In dealing with structures like multilayered transmission lines, this method is often used. As the method can handle arbitrary shapes, analysis of finlines in circular and elliptical waveguide housings [17, 18] have been published using this method.

Mode Matching Method (MMM):

As stated earlier, the Mode Matching Method was first proposed by Wexler to handle waveguide discontinuity problems. In this method the fields on both sides of the discontinuity are first expanded in terms of their respective modal functions. Using the continuity condition of the field at the interface of regions along with application of orthogonality property of the modal functions, results in a set of algebraic equations. The solution of these algebraic equations yields the eigenvalues or the scattering parameters of the fundamental and higher order modes. The modal representation of the fields directly provides the generalized scattering matrix which enables one to evaluate the field at any point close to the discontinuity including the effects of evanescent higher order modes along with the propagating fundamental mode. Consequently, a rigorous analysis of the components is possible by cascading the generalized scattering matrices of subsequent discontinuities in close proximity. The technique to cascade individual discontinuities is called the Generalized Scattering Matrix Technique (GSMT) [19]. An extension of the conventional scattering matrix technique, it was introduced by Mittra and Pace.

For an efficient design of components, optimization is essential. Optimization of any function can take several iterations before the function converges and therefore it can be time consuming, especially when the evaluation of the objective function is computationally intensive. But as MMM in conjunction with GSMT is a numerically efficient approach, optimization of components is possible within a reasonable amount of computation time. However, it should be noted that the MMM can handle only those structures where the modal functions can be expressed analytically. This means that highly arbitrary shaped structures cannot be analyzed using this method. On the other hand, most waveguide structures are of rectangular or circular shapes, and therefore explicit expressions for modal functions can be found analytically.

The equivalent circuit approximation of several waveguide discontinuities have been discussed in great detail by Marcuvitz [20]. Using these closed form expressions, Matthaei, Young and Jones have presented practical designs of many components in [21]. Accurate design of waveguide components presently relies more on MMM. Numerous paper quoted in the references have applied MMM to analyze and design components such as matching networks, filters and polarizers which involve scattering problems in rectangular waveguide technology [22-32], finlines [33-35], and microstrip lines [36,37]. The propagation characteristics for a finline structure, shielded microstrip lines and ridged waveguides have been investigated in [38-40]. However, only little work has been published on the analysis of components in circular waveguides using MMM. Analysis and design of mode converters using circular waveguides have been presented in [41,42]. Metal insert circular waveguide filter, analogous to the E-plane filter in rectangular waveguide technology, was first developed by Filolie and Vahldieck [43] where the insert was approximated by a bow-tie shaped structure. The present work builds on this idea to design filters, matching networks and polarizers in ridged circular waveguide technology. A more detailed discussion will follow in the next section.

In view of the advantages of MMM, many researchers recently have focussed attention on the combination of discretization schemes with MMM [44,45]. This scheme has been applied when there are rectangular elements in a circular housing or, in general, to problems which involve mixed coordinate system. For a combination of FEM and

MMM or FD and MMM, the eigenvalue analysis of the arbitrarily shaped structure is done using FEM or FD. Subsequently, the discontinuity from a structure that is well suited for a MMM analysis is made possible by a combination of techniques. Since the structure that is discretized is sandwiched on either sides by a region where fields can be expressed as modes, application of the matching condition and orthogonality of modes results in integrals which can be performed as summation. Therefore, the modal representation gets directly incorporated and a generalized scattering matrix is obtained. Such hybrid techniques are attractive due to the ability to handle structures that are, at least to some degree, arbitrarily shaped. In this work, however, only such structures are investigated and designed for which the MMM analysis can be used entirely. Measurements have been carried out to validate the theory proposed.

1.2 Organisation of the dissertation

Chapter 2 begins with the study of MMM. A full-wave analysis of double plane step rectangular waveguide discontinuity is first discussed as an example. Eigenvalue analysis in ridged rectangular waveguides and rectangular coaxial line have been performed. A step discontinuity in rectangular coaxial line is also analyzed and compared with the literature.

Chapter 3 discusses the eigenvalue analysis in ridged circular waveguides using MMM. The analysis of one to four ridges placed equiangularly has been analyzed and compared with the literature. The ridges have been shaped conically in order to fit the cylindrical coordinate system. It is worth mentioning here that it is possible to fabricate such shapes as well. Besides, a comparison with literature shows that for very thin ridges, it is possible to approximate the rectangular cross-section as conically shaped ones in the analysis.

The eigenvalue solutions are necessary before the scattering parameters of a discontinuity can be determined. Using the results from Chapter 3, a discontinuity from

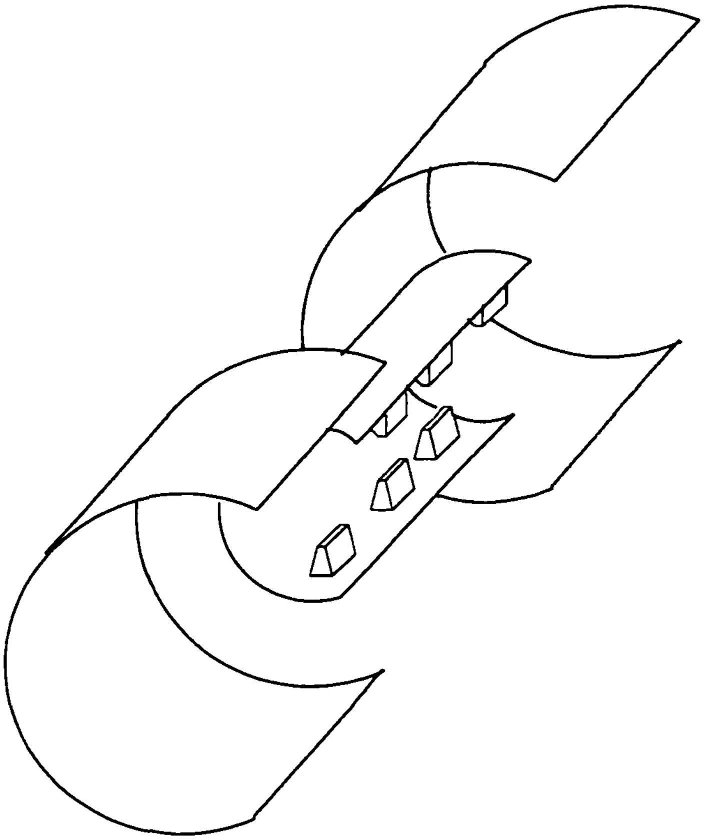

Figure 1.1: Three resonator evanescent mode circular waveguide filter

an empty circular waveguide to a ridged circular waveguide has been analyzed in Chapter 4. Based on this analysis. evanescent mode circular waveguide filters using ridged circular waveguide resonators have been designed. fabricated and measured. Also ridged circular waveguide transformers have been designed. All designs have been optimized. Figures 1.1 and 1.2 show an evanescent mode filter and a double ridged circular waveguide transformer. respectively.

Circular waveguides can support orthogonal fundamental polarization. Asymmetric structures couple energy from one polarization to the other. Such structures are an essential feature in dual mode filters and polarizers. A typical dual mode filter and a polarizer are shown in Figures 1.3 and 1.4. The dual mode filter has a coupling

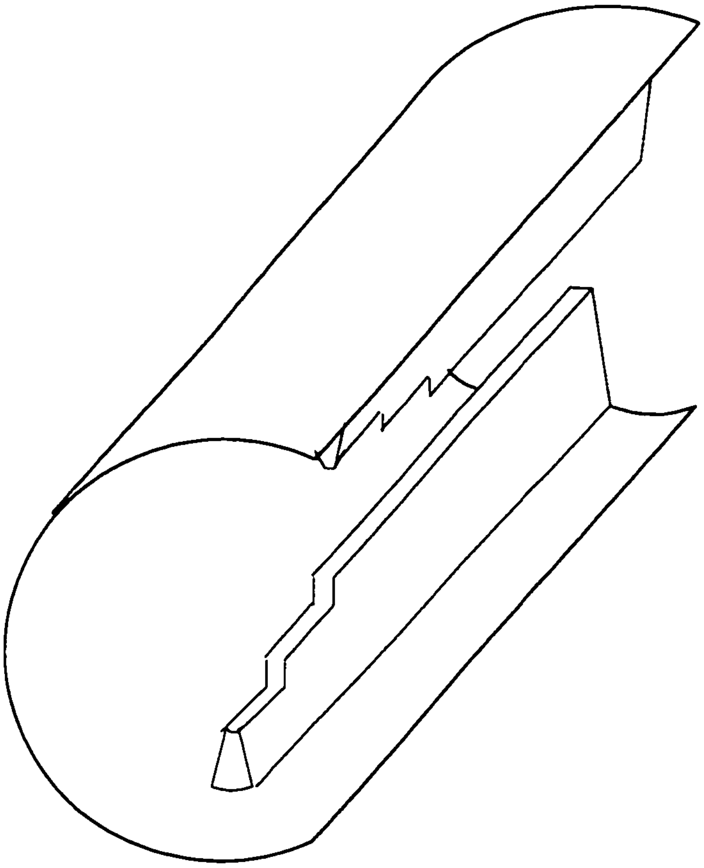

Figure 1.2: Circular ridged waveguide transformer

screw placed asymmetrically (usually at 45 degree) to the excitation. There are two other screws called the tuning screws placed horizontally and vertically. These screws are needed to tune the filter in order to overcome the discrepancies that can occur in practise. However the tuning screws can be eliminated if an accurate design is available for practical realization. Such filters, without the use of tuning screws, have been designed using a combination of FEM and MMM [45]. The hybrid approach was needed because the coupling screw was simulated as rectangular post. Chapter 5 deals with the analysis of discontinuities where the ridges in the circular waveguides have been placed asymmetrically to the excitation as in the case of a dual mode filter.

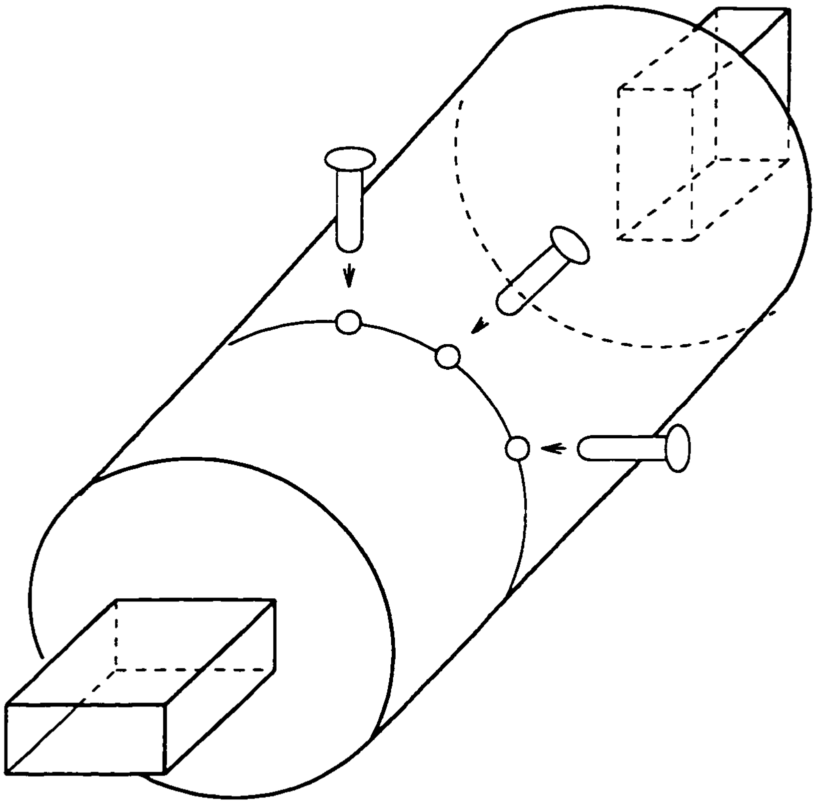

Figure 1.3: A two-pole dual-mode filter

As the ridges have been shaped conically, a rigorous analysis of a discontinuity between empty circular waveguide and single ridged or double ridged circular waveguide oriented at any arbitrary angle has been derived using MMM. The ridged region of a dual mode filter and polarizer shown in Figures 1.3 and 1.4 has been modified to the one as shown in Figure 1.5 for the analysis in the present work. The conclusions and recommendations for further work has been presented in Chapter 6.

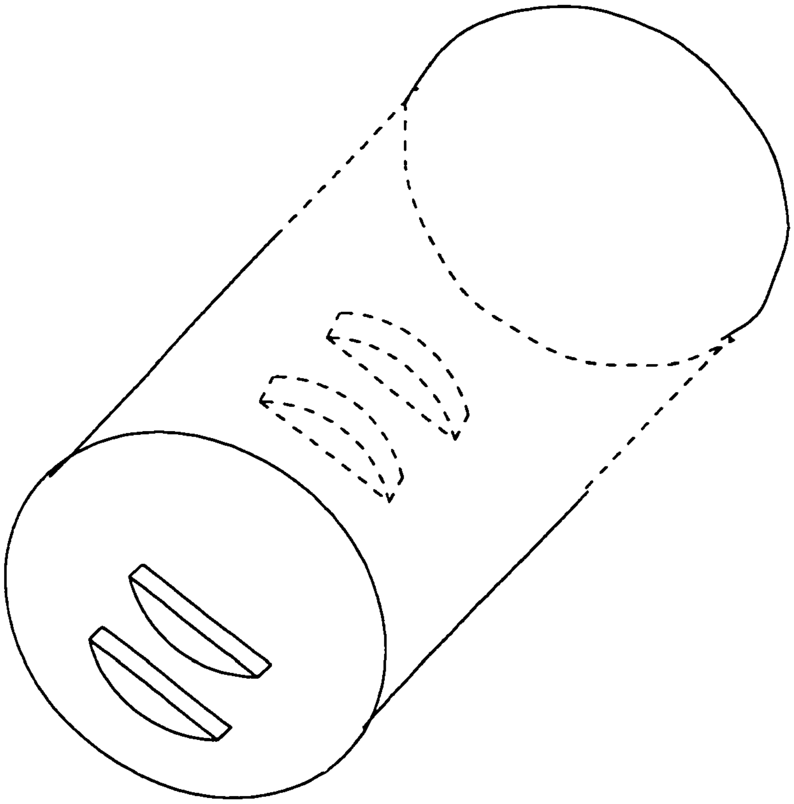

Figure 1.4: A circular waveguide polarizer

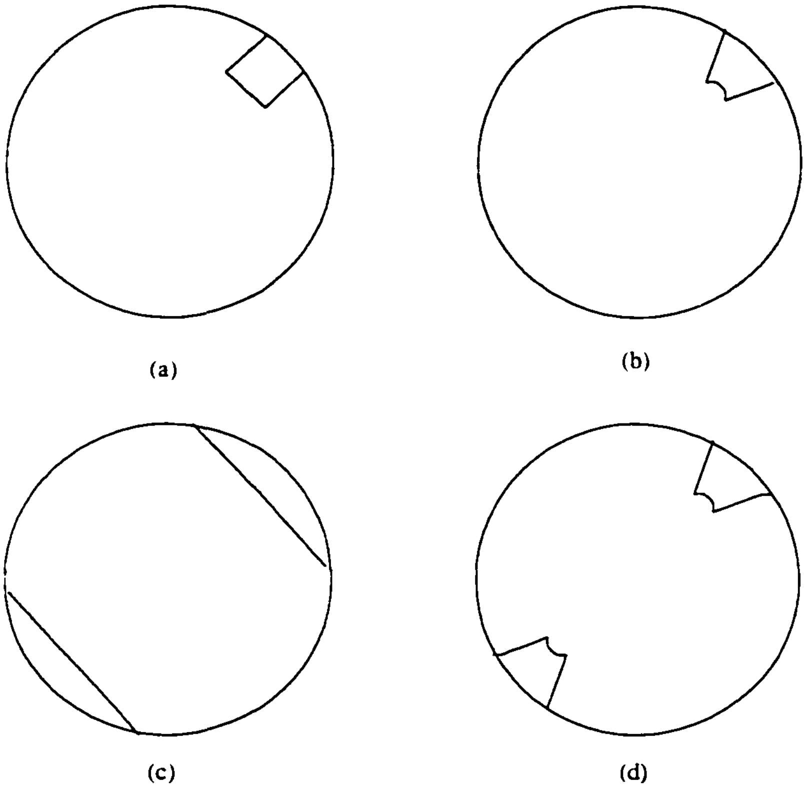

Figure 1.5: (a) Ridged section in a dual-mode filter (b) Modified ridged section as used in the present work (c) Corrugated section in a circular waveguide polarizer (d) Ridged section as used in the present work

Chapter 2

Analysis of Rectangular Coaxial Lines Using Mode Matching Method

2.1 Introduction

The Rectangular Coaxial Line (RCL) has been used in beam forming networks [46] as an alternative to the rectangular waveguide. The RCL has reduced dimensions compared to the rectangular waveguides which makes it attractive for satellite applications. The power handling capability and loss characteristics of RCL are comparable to that of circular coaxial line. Besides, manufacturing components using RCL is more economical compared to that in circular coaxial lines. Computer aided design of RCL components is important to further reduce manufacturing cost and to reduce the design-manufacturing cycle.

This chapter begins with a description of the Mode Matching Method as the "engine" for the analysis of a variety of discontinuities utilized in the design of filters, polarizers and beam forming networks. The double step discontinuity in rectangular waveguides is analyzed first. Since, the Mode Matching Method analysis of step discontinuities in rectangular coaxial lines is an extension to this type of discontinuity it will be discussed second. The mode matching analysis of components in circular waveguides discussed in the later chapters can be derived straightforwardly from discontinuities in rectangular waveguides.

In order to characterize discontinuities using the Mode Matching Method, the eigenvalues of the cross-section left and right from the discontinuity plane must be known. The eigenvalues of the RCL cross-section cannot be written analytically as in a rectangular waveguide or a circular coaxial line. Hence, in order to analyze discontinuities in the rectangular coaxial lines an eigenvalue analysis of the cross-section has to be done first. There are four possible symmetries in the rectangular coaxial lines cross-section. For a particular symmetry of RCL, the structure is that of a single ridged rectangular waveguide which has been analyzed in the literature before. This symmetry is discussed first, followed by the eigenvalue analysis of a RCL for various other symmetries. The Transverse Electromagnetic cell(TEM cell) which is used in electromagnetic interference and compatibility tests has the cross-section of a RCL with very thin inner conductor. The eigenvalues of the RCL obtained using the MMM are compared with the literature for a TEM cell. The characteristic impedance of the RCL is another important parameter for the discontinuity analysis and has been obtained in this chapter using the Mode Matching Method and the finite difference method. Finally, a step discontinuity in the RCL has been analysed and compared with measurements from the literature.

2.2 Full wave analysis of a double step discontinuity in rectangular waveguide

The analysis of any discontinuity using the MMM involves the following steps.

1. The fields on both sides of the discontinuity are expanded in terms of a series of modes of incident and reflected waves.

2. The magnitude of power carried by each of the modes is set to unity.

3. The continuity conditions for the tangential components of the electric and magnetic fields are imposed.
4. Using the principle of orthogonality of modes, the equations of the continuity conditions are transformed into matrices relating the expansion coefficients of incident and reflected waves at the discontinuity.
5. The matrices are rearranged and inverted suitably to obtain the generalized scattering matrix which describes the discontinuity in terms of the dominant and higher order modes.

Theoretically, the generalized scattering matrix is of infinite dimensions corresponding to the infinite number of eigenmodes. The matrix is truncated to a finite size for numerical calculations. Hence a larger matrix has to be inverted if more modes are included in the analysis. The test for the maximum number of modes to be included for the most accurate result or, in other words, a test of convergence of the evaluated scattering parameters is hence an important part of every analysis using the MMM. Since there is a choice on the number of modes included in the two or more regions of the discontinuity, the best possible ratio between the number of modes also has to be identified. This phenomenon of relative convergence has been extensively studied in the literature [47] and a further discussion will be presented later at the end of this section.

A fact that is worth observing before beginning an analysis of a discontinuity is to find if the fundamental mode that is excited in the discontinuity couples energy to all the higher order modes included in the analysis. If the fundamental mode that is excited in the discontinuity does not couple energy to some of the higher order modes, then such modes can be eliminated from the analysis. By including these modes, however, the scattering parameters of the fundamental mode do not get altered. This certainly involves more computational effort in calculating the elements of the matrices or inverting them. On the other hand, at certain discontinuities, it

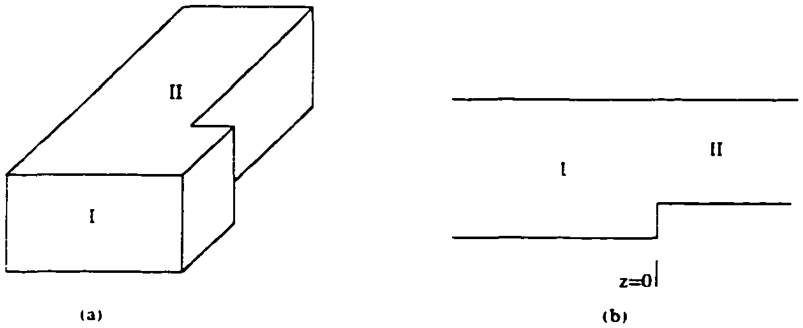

Figure 2.1: H-plane step discontinuity

is sometimes necessary to include higher order modes that are not necessary for the analysis of that discontinuity. This is so because at subsequent discontinuities these higher order modes may get excited and, if the two types of discontinuities are in close proximity to each other, all modes that can possibly be excited will interact and affect the performance of the component. An example of such a situation is discussed in Chapter 4. A knowledge of which modes must be included in the analysis can be derived from the symmetries of a discontinuity and the symmetry in the fundamental mode that is incident. For instance, at a H-plane discontinuity, as shown in Figure 2.1, the fundamental mode ($TE_{1,0}$ mode) excitation will not excite modes other than the $TE_{m,0}$ modes (where $m = 1, 2, 3, \cdots$). At a discontinuity that has no symmetries whatsoever, it is essential to include all the higher order modes in the analysis and check for convergence to get the accurate values of the S-parameters.

The double plane step discontinuity as shown in Figure 2.2 is a symmetric one. The incident fundamental $TE_{1,0}$ mode will excite only modes with magnetic wall and electric wall symmetry as shown in Figure 2.2. This implies that it is sufficient to include only modes with such symmetry namely the $TE_{m,n}$ and $TM_{m,n}$ with m odd and n even. However, at an asymmetric step shown in Figure 2.3(b) all the modes have to be included in the mode matching analysis. The analysis of the double plane step discontinuity is well known and has already been been presented in a number of

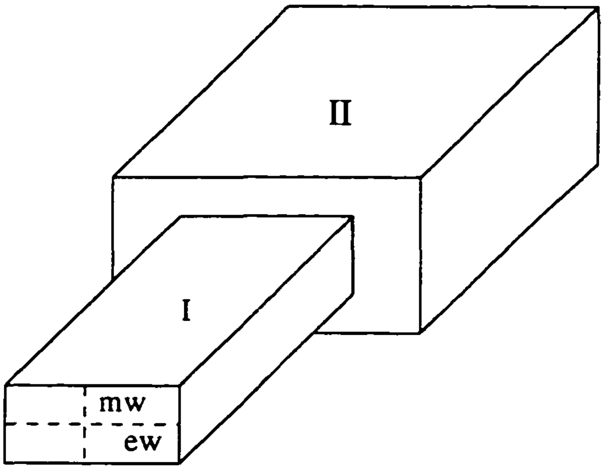

Figure 2.2: Double plane step discontinuity in rectangular waveguides

papers. [23,24]. It has been repeated here for introducing the principles of MMM.

The full-wave analysis presented in the following is based on the matching of the tangential field components at the discontinuity. The fields are derived from the superposition of the electric and magnetic vector potentials. The two potential vectors are represented in terms of mode functions that are transverse electric ($TE^z_{m,n}$) and transverse magnetic ($TM^z_{m,n}$) to either the z coordinate (usually the direction of wave propagation) or the x ($TE^x_{m,n}$ and $TM^x_{m,n}$) or y ($TE^y_{m,n}$ and $TM^y_{m,n}$) coordinates. The alternative field descriptions other than the one in propagation direction is necessary either for improving the efficiency of the method or for analyzing certain types of discontinuities. However, in the following analysis the z-component of the vector potentials is used to describe the field components as this is more appropriate for the discussions in later chapters.

The six field components are obtained from the superposition of the potential vectors $\overrightarrow{\psi}_z^{(h)}$ and $\overrightarrow{\psi}_z^{(e)}$.

$$\overrightarrow{E} = \nabla \times \overrightarrow{\psi_z}^{(h)} + \frac{1}{j\omega\epsilon_o}\nabla \times \nabla \times \overrightarrow{\psi_z}^{(e)} \tag{2.1}$$

$$\overrightarrow{H} = \frac{-1}{j\omega\mu_o}\nabla \times \nabla \times \overrightarrow{\psi_z}^{(h)} + \nabla \times \overrightarrow{\psi_z}^{(e)} \tag{2.2}$$

The potential vectors $\overrightarrow{\psi_z}^{(h)}$ and $\overrightarrow{\psi_z}^{(e)}$ individually satisfy the Helmholtz equation from which the fields are derived. Superscripts h and e denote the magnetic and electric potentials respectively. They can be written as an infinite sum of the incident and reflected normal modes in both regions of the discontinuity. The coefficients $C_{p,q}$ and $A_{m,n}$ are the incident wave amplitudes of TM and TE, respectively, while $D_{p,q}$ and $B_{m,n}$ are the reflected wave amplitudes, respectively, as indicated in Figure 2.3.

$$\overrightarrow{\psi_{m,n}}^{(Rh)}(x,y,z) = \sum_{m=0}^{\infty}\sum_{n=0}^{\infty}\sqrt{Z_{m,n}^{(Rh)}}\,\psi_{m,n}^{(Rh)}(x,y)(A_{m,n}^{(R)}e^{-j\beta_{m,n}^{(Rh)}z} + B_{m,n}^{(R)}e^{j\beta_{m,n}^{(Rh)}z}) \tag{2.3}$$

$$\overrightarrow{\psi_{p,q}}^{(Re)}(x,y,z) = \sum_{p=1}^{\infty}\sum_{q=1}^{\infty}\sqrt{Y_{p,q}^{(Re)}}\,\psi_{p,q}^{(Re)}(x,y)(C_{p,q}^{(R)}e^{-j\beta_{p,q}^{(Re)}z} - D_{p,q}^{(R)}e^{j\beta_{p,q}^{(Re)}z}) \tag{2.4}$$

where, $R \in I, II$ are the two regions of the discontinuity. The wave impedance Z and admittance Y are as follows:

$$Z_{m,n}^{(Rh)} = \frac{\omega\mu_o}{\beta_{m,n}^{(Rh)}} \tag{2.5}$$

$$Y_{p,q}^{(Re)} = \frac{\omega\epsilon_o}{\beta_{p,q}^{(Re)}} \tag{2.6}$$

It can be observed that the coefficients of the field components namely A, B, C and D have two indices. This is a direct consequence of the separation of variable solution to

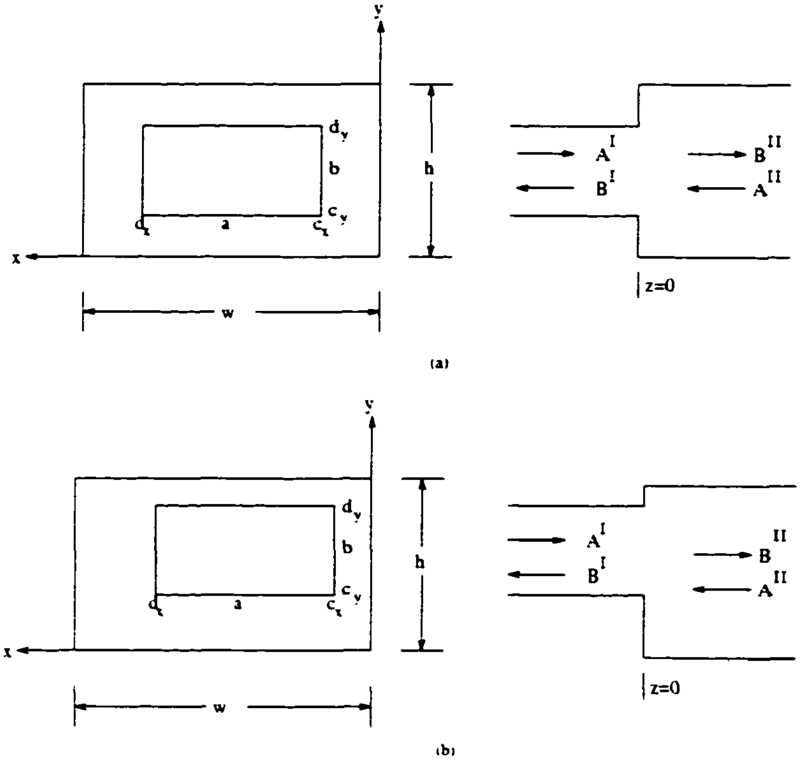

Figure 2.3: (a)Symmetric double plane step discontinuity in rectangular waveguide (b) Asymmetric double plane step discontinuity in rectangular waveguide

the Helmholtz equation. However, these coefficients form a vector during the analysis, since m, n or p, q represent one particular mode with a certain value of propagation constant $\beta_{m,n}$ or $\beta_{p,q}$. The transverse component of the potential functions in the region II can be written as:

$$\psi_{m,n}^{(IIh)}(x,y) = T_{m,n}^{(IIh)} \frac{\cos(k_{x_m}^{(II)}x)\cos(k_{y_n}^{(II)}y)}{\sqrt{1+\delta_{0,m}}\sqrt{1+\delta_{0,n}}} \tag{2.7}$$

$$\psi_{p,q}^{(IIe)}(x,y) = T_{p,q}^{(IIe)} \sin(k_{x_p}^{(II)}x)\sin(k_{y_q}^{(II)}y) \tag{2.8}$$

where $k_{x_m}^{(II)} = m\pi/w$, $k_{y_n}^{(II)} = n\pi/h$, $k_{x_p}^{(II)} = p\pi/w$ and $k_{y_q}^{(II)} = q\pi/h$ when w is the width and h is the height of the rectangular waveguide in region II.

Similarly in region I the potential functions are as follows:

$$\psi_{m,n}^{(Ih)}(x,y) = T_{m,n}^{(Ih)} \frac{\cos(k_{x_m}^{(I)}(x-c_x))\cos(k_{y_n}^{(I)}(y-c_y))}{\sqrt{1+\delta_{0,m}}\sqrt{1+\delta_{0,n}}} \tag{2.9}$$

$$\psi_{p,q}^{(Ie)} = T_{p,q}^{(Ie)} \sin(k_{x_p}^{(I)}(x-c_x))\sin(k_{y_q}^{(I)}(y-c_y)) \tag{2.10}$$

where $k_{x_m}^{(I)} = m\pi/a$, $k_{y_n}^{(I)} = n\pi/b$, $k_{x_p}^{(I)} = p\pi/a$ and $k_{y_q}^{(I)} = q\pi/b$ with a as the width and b as the height of the rectangular waveguide.

The propagation constants in either regions (R), can be evaluated from

$$\beta_{i,j}^{(R)^2} = k_o^2\epsilon_r - k_{x_i}^{(R)^2} - k_{y_j}^{(R)^2} \tag{2.11}$$

The power carried by each mode and in each of the region is evaluated from

$$P_i^{(R)} = \frac{1}{2}\Re\left\{\int_{S^{(R)}} \left(\overrightarrow{E_i}^{(R)} \times \overrightarrow{H_i}^{(R*)}\right)\cdot d\overrightarrow{A}\right\} \tag{2.12}$$

where $S^{(R)}$ is the surface area of the cross-section of that region. The coefficients $T_{m,n}^{(hR)}$ and $T_{p,q}^{(eR)}$ of the potential functions are chosen so that the magnitude of the power carried in the corresponding mode is unity. Thus,

$$P = \begin{cases} 1W & \text{for propagating modes} \\ +jW & \text{for evanescent } TE \text{ modes} \\ -jW & \text{for evanescent } TM \text{ modes} \end{cases} \tag{2.13}$$

This yields,

$$T_{m,n}^{(IIh)} = \frac{2}{\sqrt{(\frac{m\pi}{w})^2 + (\frac{n\pi}{h})^2}\sqrt{wh}} \tag{2.14}$$

$$T_{p,q}^{(IIe)} = \frac{2}{\sqrt{(\frac{p\pi}{w})^2 + (\frac{q\pi}{h})^2\sqrt{wh}}} \tag{2.15}$$

$$T_{m,n}^{(Ih)} = \frac{2}{\sqrt{(\frac{m\pi}{a})^2 + (\frac{n\pi}{b})^2\sqrt{ab}}} \tag{2.16}$$

$$T_{p,q}^{(Ie)} = \frac{2}{\sqrt{(\frac{p\pi}{a})^2 + (\frac{q\pi}{b})^2\sqrt{ab}}} \tag{2.17}$$

At the junction of the discontinuity (z=0) formed by two rectangular waveguides. with their axis in line. as shown in Figure 2.3. the continuity condition is applied as follows

$$\begin{aligned} E^{(I)}(x.y) &= E^{(II)}(x.y) && x \in [c_x.d_x] \;\; y \in [c_y.d_y] && (2.18) \\ &= 0 && \text{otherwise} && (2.19) \\ H^{(I)}(x.y) &= H^{(II)}(x.y) && x \in [c_x.d_x]. \;\; y \in [c_y.d_y] && (2.20) \end{aligned}$$

The above two continuity conditions of tangential electric and magnetic fields can be separated into four sets of coupling equations using the property of orthogonality of modes. The resulting coupling equations after matching the tangential electric fields at the discontinuity and applying orthogonality is of the following form:

$$A_{i,j}^{(II)} + B_{i,j}^{(II)} = V_{hh}(A_{m,n}^{(I)} + B_{m,n}^{(I)}) + V_{he}(C_{p,q}^{(I)} + D_{p,q}^{(I)}) \tag{2.21}$$

$$C_{i,j}^{(II)} + D_{i,j}^{(II)} = V_{ee}(C_{p,q}^{(I)} + D_{p,q}^{(I)}) + V_{eh}(A_{m,n}^{(I)} + B_{m,n}^{(I)}) \tag{2.22}$$

It must be noted that though the coefficients of the field components. namely $A. B. C$ and D when they form a vector are arranged in ascending order of the cutoff frequencies of the corresponding modes. The elements of the matrices V_{hh}. V_{eh}. V_{he} and V_{ee} can be computed from the equations below.

$$V_{hh}(ij,mn) = \sqrt{\frac{\beta^{(IIh)}_{i,j}}{\beta^{(Ih)}_{m,n}}}\int_{c_x}^{d_x}\int_{c_y}^{d_y}(\overrightarrow{\epsilon}^{(Ih)}_{mn})\cdot(\overrightarrow{\epsilon}^{(IIh)}_{ij})dxdy \tag{2.23}$$

$$V_{ee}(ij,pq) = \sqrt{\frac{\beta^{(Ie)}_{p,q}}{\beta^{(IIe)}_{i,j}}}\int_{c_x}^{d_x}\int_{c_y}^{d_y}(\overrightarrow{\epsilon}^{(Ie)}_{pq})\cdot(\overrightarrow{\epsilon}^{(IIe)}_{ij})dxdy \tag{2.24}$$

$$V_{eh}(ij,mn) = \frac{k_o}{\sqrt{\beta^{(IIe)}_{i,j}\beta^{(Ih)}_{m,n}}}\int_{c_x}^{d_x}\int_{c_y}^{d_y}(\overrightarrow{\epsilon}^{(IIe)}_{ij})\cdot(-\overrightarrow{\epsilon}^{(Ih)}_{mn})dxdy \tag{2.25}$$

$$V_{he}(ij,mn) = \frac{\sqrt{\beta^{(IIh)}_{i,j}\beta^{(Ie)}_{m,n}}}{k_o}\int_{c_x}^{d_x}\int_{c_y}^{d_y}(\overrightarrow{\epsilon}^{(Ie)}_{mn})\cdot(-\overrightarrow{\epsilon}^{(IIh)}_{ij})dxdy \tag{2.26}$$

The vectors ϵ are the tangential electric fields evaluated from the potential functions and are obtained using Appendix A or the equations below:

$$\overrightarrow{\epsilon}^{(Ih)}_{mn} = \hat{z}\times\nabla_z\psi^{Ih}_{mn} \tag{2.27}$$

$$\overrightarrow{\epsilon}^{(Ie)}_{pq} = \nabla_z\psi^{Ie}_{pq} \tag{2.28}$$

$$\overrightarrow{\epsilon}^{(IIh)}_{ij} = \hat{z}\times\nabla_z\psi^{IIh}_{mn} \tag{2.29}$$

$$\overrightarrow{\epsilon}^{(IIe)}_{ij} = \nabla_z\psi^{IIe}_{ij} \tag{2.30}$$

It can be verified that V_{he} is zero. This has been analytically proved in [48]. Matching the H-fields and applying orthogonality again results in

$$A^{(I)}_{i,j} - B^{(I)}_{i,j} = V^t_{hh}(A^{(II)}_{m,n} - B^{(II)}_{m,n}) + V^t_{eh}(C^{(II)}_{p,q} - D^{(II)}_{p,q}) \tag{2.31}$$

$$C^{(I)}_{i,j} - D^{(I)}_{i,j} = V^t_{ee}(C^{(II)}_{p,q} - D^{(II)}_{p,q}) \tag{2.32}$$

It can be verified that the coupling matrices in the above equations are transposes of the V_{hh}, V_{eh} and V_{ee} obtained in the E-field matching. Rearranging the four sets of equations, we have

$$\underbrace{\begin{pmatrix} U & 0 & V_{hh}^t & V_{eh}^t \\ 0 & U & 0 & V_{ee}^t \\ -V_{hh} & 0 & U & 0 \\ -V_{eh} & -V_{ee} & 0 & U \end{pmatrix}}_{K_1} \begin{pmatrix} B^{(I)} \\ D^{(I)} \\ A^{(II)} \\ C^{(II)} \end{pmatrix} =$$

$$\underbrace{\begin{pmatrix} U & 0 & V_{hh}^t & V_{eh}^t \\ 0 & U & 0 & V_{ee}^t \\ V_{hh} & 0 & -U & 0 \\ V_{eh} & V_{ee} & 0 & -U \end{pmatrix}}_{K_2} \begin{pmatrix} A^{(I)} \\ C^{(I)} \\ B^{(II)} \\ D^{(II)} \end{pmatrix} \qquad (2.33)$$

where U is the unit matrix.

The generalized scattering matrix of a step discontinuity is hence given by

$$S = K_1^{-1} K_2 \qquad (2.34)$$

An alternative scheme of inversion [49] is given in the Appendix B. That scheme is computationally more efficient, since the size of the matrix to be inverted is smaller compared to that in the equation (2.34). Hence, the inversion technique in Appendix B has been used in all the analyses presented in this work.

The symmetric double step discontinuity can also be analyzed using the $TE_{m,n}^x$ approach, as the fundamental mode $TE_{1,0}^x$ is the same as $TE_{1,0}^z$. In this approach, the fields at the discontinuity are evaluated based on the magnetic vector potential ψ_x^h ($E_x = 0$) alone. This approach is not a rigorous one as the ψ_x^e potential vector is ignored due to the fact that the E_x field is very small at the discontinuity. Although this type of analysis produces a computationally efficient algorithm, it has been shown in [50] that for certain types of component analysis, like resonant-iris waveguide filters, this approach can result in inaccurate results. An improved version of the $TE^x_{m,n}$ approach has been presented in the same reference [50].

2.2.1 Convergence analysis

In order to overcome the phenomenon of relative convergence in the MMM, the number of modes included in the regions left and right of the discontinuity are truncated suitably. This phenomenon has been discussed extensively in [47]. For rectangular waveguides, where the potential vector is a double sum in the two coordinates of the cross-section, best convergence is observed when the truncation ratio of the modal indices in the two regions is equal to the corresponding dimension ratio. The convergence of the S-parameters for a symmetric step discontinuity occurs with only about 20 TE and TM included in the waveguide with greater dimensions. The variations of S_{11} and S_{12} with frequency is shown in Figures 2.4 and 2.5. The results agree very well with literature [26].

2.3 Eigenvalue analysis using MMM

The MMM can be applied to solve for the eigenvalues in complex structures including microstrip lines, coplanar waveguides and finlines. A rectangular single ridged waveguide has been treated here as an example. Since the structure is symmetric, a magnetic wall or electric wall symmetry can be assumed to obtain the eigenvalues of the corresponding modes. One half of the symmetric ridged waveguide is once again divided into two subregions as shown in Figure 2.6. The potential functions in each of these regions can be expressed in terms of x and y dependent terms that satisfy the Helmholtz equation and the boundary conditions in the two subregions. The electric and magnetic potential functions for a magnetic wall symmetry is written as:

$$\psi^{(e1)} = \sum_{m=1}^{M} A_m \sin \frac{m\pi y}{q} \cos(k_{x_m}^{(1e)}(x - a/2)) \tag{2.35}$$

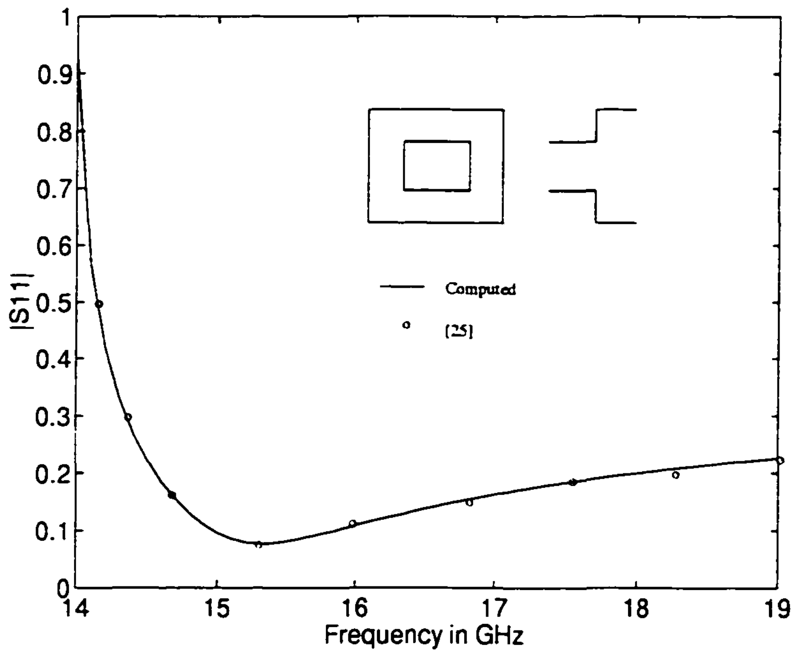

Figure 2.4: Magnitude of reflection coefficient from a input waveguide of dimension 10.7mm × 4.32mm to a output waveguide of dimension 15.8mm × 7.9mm

$$v^{(e2)} = \sum_{n=1}^{N} B_n \sin\frac{n\pi y}{u}\frac{1}{k_{x_n}^{(2e)}}\sin(k_{x_n}^{(2e)}x) \tag{2.36}$$

$$v^{(h1)} = \sum_{m=0}^{M} C_m \cos\frac{m\pi y}{q}\frac{1}{k_{x_m}^{(1h)}}\sin(k_{x_m}^{(1h)}(x-a/2)) \tag{2.37}$$

$$v^{(h2)} = \sum_{n=0}^{N} D_n \cos\frac{n\pi y}{u}\cos(k_{x_n}^{(2h)}x) \tag{2.38}$$

The propagation constant in the x direction in the above equations (2.35) to (2.38) can be obtained from the equations below.

$$\begin{pmatrix} k_{x_m}^{(1h)^2} \\ k_{x_n}^{(2h)^2} \end{pmatrix} = k_o^2 - k_z^{(IIh)^2} - \begin{pmatrix} \left(\frac{m\pi}{q}\right)^2 \\ \left(\frac{n\pi}{u}\right)^2 \end{pmatrix} \tag{2.39}$$

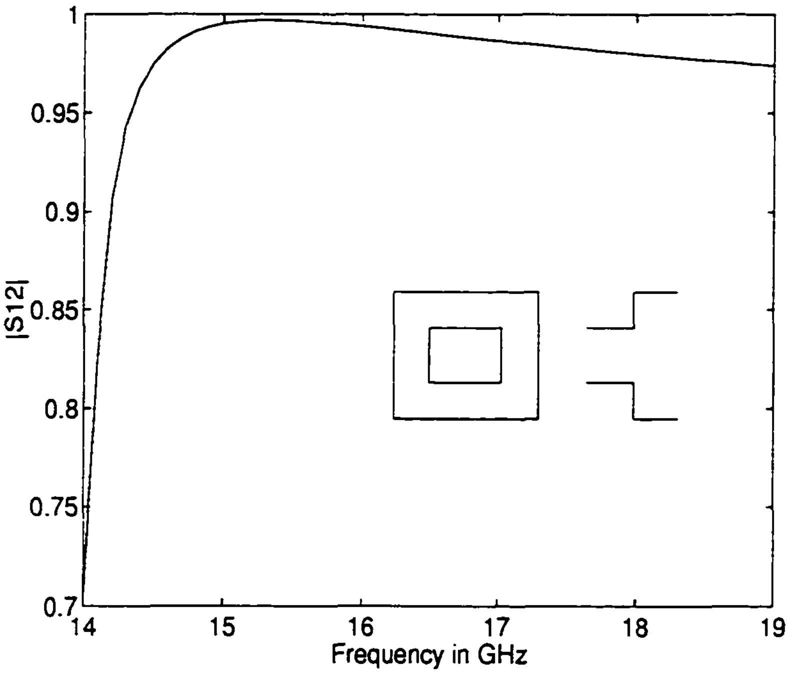

Figure 2.5: Magnitude of transmission coefficient from a input waveguide of dimension 10.7mm × 4.32mm to a output waveguide of dimension 15.8mm × 7.9mm

$$\begin{pmatrix} k_{x_m}^{(1e)^2} \\ k_{x_n}^{(2e)^2} \end{pmatrix} = k_o^2 - k_z^{(IIe)^2} - \begin{pmatrix} \left(\frac{m\pi}{q}\right)^2 \\ \left(\frac{n\pi}{u}\right)^2 \end{pmatrix} \qquad (2.40)$$

At cutoff, k_z is zero and the cutoff wavenumber is defined as $k_c^2 = k_x^2 + k_y^2$. Hence, in equations (2.39) and (2.40) k_z is set to zero for the eigenvalue analysis. The tangential components of E_y, H_z (for TE modes) or H_y, E_z (for TM modes) are evaluated from the potential functions using the formulas in Appendix A. These field components are matched at the interface of subregions 1 and 2. In order that the fields be described completely, the summation of the potential functions should be infinite, i.e M and N should be infinite. However, for numerical purposes they are truncated. Using

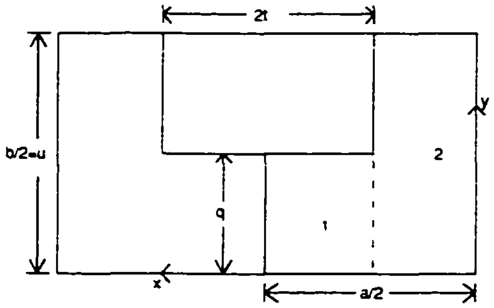

Figure 2.6: Single ridged rectangular waveguide

orthogonality a system of homogeneous equations is obtained. It is of the form:

$$[F][X] = 0 \tag{2.41}$$

The vector $[X]$ is an array of the unknown coefficients C_m and D_n for TE modes and A_m and B_n for TM modes. The characteristic equation for the TE modes is given below:

$$\begin{pmatrix} P & Q \\ R & S \end{pmatrix} \begin{pmatrix} C \\ D \end{pmatrix} = \begin{pmatrix} 0 \\ 0 \end{pmatrix} \tag{2.42}$$

where the elements of the submatrices of F can be obtained as:

$$P(m,n) = \begin{cases} q\frac{1}{k_{x_n}^{(1h)}} \sin\left(k_{x_n}^{(1h)}(t - a/2)\right) & \text{if } m{=}n{=}0 \\ \frac{q}{2}\frac{1}{k_{x_n}^{(1h)}} \sin\left(k_{x_n}^{(1h)}(t - a/2)\right) & \text{if } m{=}n \text{ and } m \neq 0 \\ 0 & \text{otherwise} \end{cases} \tag{2.43}$$

$$Q(m,n) = -\cos k_{x_m}^{(2h)} t \int_0^q \cos\frac{n\pi y}{q} \cos\frac{m\pi y}{u} dy \tag{2.44}$$

$$S(m,n) = \begin{cases} u \sin\left(k_{x_n}^{(2h)} t\right) & \text{if } m{=}n{=}0 \\ u/2 \sin\left(k_{x_n}^{(2h)} t\right) & \text{if } m{=}n \text{ and } m \neq 0 \\ 0 & \text{otherwise} \end{cases} \tag{2.45}$$

$$R(m,n) = \cos k_{x_n}^{(1h)}(t - a/2) \int_0^q \cos \frac{m\pi y}{q} \cos \frac{n\pi y}{u} dy \tag{2.46}$$

In order for the coefficients of the potential functions to be non zero or, in other words, to get a nontrivial solution, the determinant of the characteristic matrix F should be zero. Hence, the cutoff wave number of all the modes can be obtained by searching for the zero of the determinant at various k_o. As the value of M and N is increased a convergence behavior can be observed. The ratio of M to N can be set equal to the ratio of the ridge gap to waveguide height in order to overcome the relative convergence phenomenon. It has been shown that the Singular Value Decomposition(SVD) of the characteristic matrix [51] can be used to determine the eigenvalues.

Using the SVD, a matrix can be decomposed as below

$$(A) = (U)(S)(V) \tag{2.47}$$

where (S) is a diagonal matrix formed by the singular values in decreasing order and (U) and (V) are columns of left and right singular vectors. The cutoff wavenumbers are obtained using a search for the minimum of the smallest singular value while using SVD. The poles of the determinant of F do not affect the singular values and hence the values of M and N can be chosen for the best convergence. Using this procedure, the eigenvalues of TE and TM modes of the single ridged rectangular waveguide have been obtained and summarized in Table 2.1. Results are in close agreement with [52] where the eigenvalue solutions are obtained using variational technique.

Mode Pattern	Eigenvalue of rect. WG rad/mm	Utsumi's [52] solution rad/mm	MMM solutions rad/mm
$TE_{1,0}$	.1653	.0930	.0943
$TE_{1,1}$	.3697	.3332	.3322
$TE_{3,0}$	.4960	.3881	.3820
$TE_{3,1}$	.5962	.5265	.5282
$TE_{1,2}$	.6817	.6654	.6654
$TE_{5,0}$	.8267	.6917	.6918
$TE_{3,2}$	.8267	.7456	.7458
$TE_{5,1}$	.8904	.8298	.8321
$TM_{1,1}$	.3697	.4665	.4708
$TM_{1,2}$	.6817	.7358	.7408
$TM_{3,2}$	.8267	.9427	.9379

Table 2.1: Eigenvalues of single ridged rectangular waveguide of dimension a=19mm. u=9.5mm. q=1.7mm and t=0.15mm

2.4 Analysis of rectangular coaxial line step discontinuity using MMM

Step discontinuities in rectangular coaxial lines (Figure 2.7) can be analyzed using the MMM [53]. However. unlike in the case of rectangular waveguide or circular coaxial lines. knowledge of higher order modes is not available analytically. Hence. the first step involves the eigenvalue analysis for the determination of higher order TE and TM modes. The fundamental mode is the TEM type and its solution is obtained from Laplace's equation.

2.4.1 Step 1: Eigenvalue Analysis

The solution for the fundamental transverse electromagnetic mode is obtained by solving Laplaces equation

$$\nabla^2 V = 0 \tag{2.48}$$

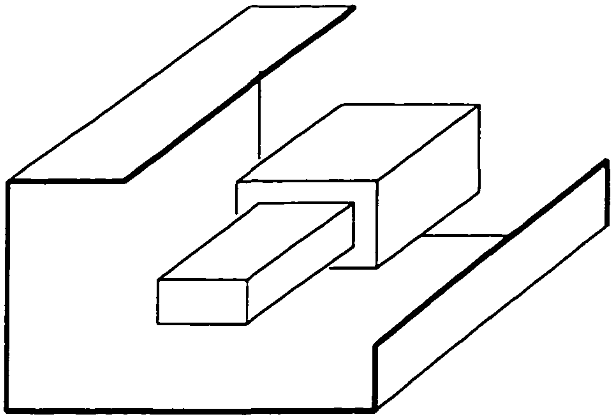

Figure 2.7: Symmetric inner conductor step discontinuity in RCL

Using a magnetic wall along the two lines of symmetry it is sufficient to analyze one quarter of the cross-section alone. This is again divided into two subregions as shown in Figure 2.8. The inner line is assumed to be at potential V_o and the outer line at zero potential. The solution for the potentials in both regions is obtained from Laplaces equation with unknown coefficients. At the interface of the two subregions the continuity of the potential is applied. The solution for the potentials in the two regions is found as:

$$V(x,y)^{(1)} = \frac{V_o y}{q} \tag{2.49}$$

$$V(x,y)^{(2)} = \sum_{n=1,3}^{\infty} \frac{4V_o}{bq} \frac{1}{(\frac{n\pi}{b})^2} \frac{\sin \frac{n\pi}{b} q}{\sinh(\frac{n\pi}{b}(\frac{a}{2} - t))} \sin \frac{n\pi y}{b} \sinh \frac{n\pi x}{b} \tag{2.50}$$

The value of n is odd due to symmetry. For numerical purpose the summation in equation (2.50)is truncated. The TEM electric field components in the two subregions are obtained using

$$E = -\nabla V \tag{2.51}$$

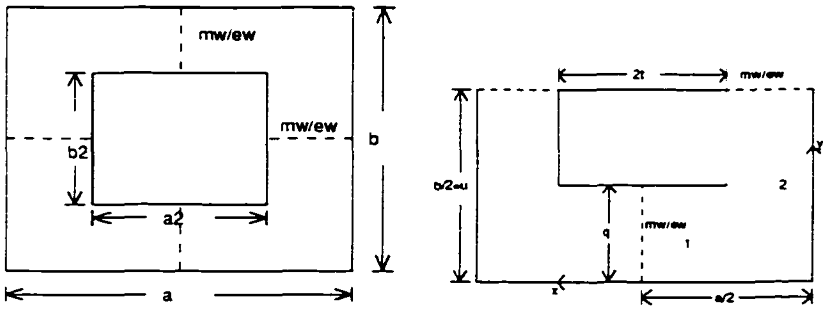

(a) (b)

Figure 2.8: (a)Cross-section of RCL (b) Expanded view of half the cross-section of RCL

If the inner conductor of the RCL is infinitely thin, the potential functions can be obtained by setting $q = b/2$ in equations (2.49) and (2.50). The capacitance per unit length of the line is obtained using Gauss law to solve for the charge Q on the center conductor and then evaluated using the relation given below.

$$C = \frac{Q}{V_o} \tag{2.52}$$

The characteristic impedance is evaluated from the following relation

$$Z = \frac{1}{Cv} \tag{2.53}$$

where v is the velocity of light.

The characteristic impedance for certain dimensions has also been obtained using the finite difference technique in order to compare the solutions with the above technique. This comparison has been summarized in Table 2.2. The difference between the two methods may be due to the edge condition not being satisfied completly at the interface of the two subregions while using MMM.

Sl. no.	Dimensions in cms a. b a2. b2	MMM impedance solution (Ohms)	Finite Difference (Ohms)
1.	1.1. 1.0 0.416.0.416	47.24	49.60
2.	1.1. 1.0 0.7. 0.6	23.95	24.64
3.	610. 730 406. 0.157	47.32	

Table 2.2: Characteristic impedance of RCL

The variation of the characteristic impedance with the increase in the width of the inner conductor. while keeping its thickness constant. is shown in Figure 2.9.

The cutoff frequencies of all the higher order modes in RCL can be obtained by considering suitable symmetries. There are four possible symmetries for the RCL as there are two lines of symmetry as shown in Figure 2.8 which can be either electric or magnetic walls. Each of the higher order modes evaluated can be traced to the $TE_{m,n}$ or the $TM_{m,n}$ mode in an empty rectangular waveguide of the same dimensions where the inner conductor of the RCL is absent. Hence. in the RCL they are referred to by the same mode nomenclature as in a rectangular waveguide though the field components are significantly altered. The cutoff frequencies of the higher order modes corresponding to the magnetic wall along the y direction and electric wall along the x direction ($TE_{odd,even}$ and $TM_{odd,even}$) can be evaluated using the equations presented in section 1.3 for the single ridged rectangular waveguide because the quarter cross-section of RCL for such a symmetry is the same as that of the single ridged rectangular waveguide. Similarly. for the symmetry with electric wall along the y direction and magnetic wall along the x direction ($TE_{even,odd}$ and $TM_{even,odd}$). the quarter cross-section reduces to that of a single ridged rectangular

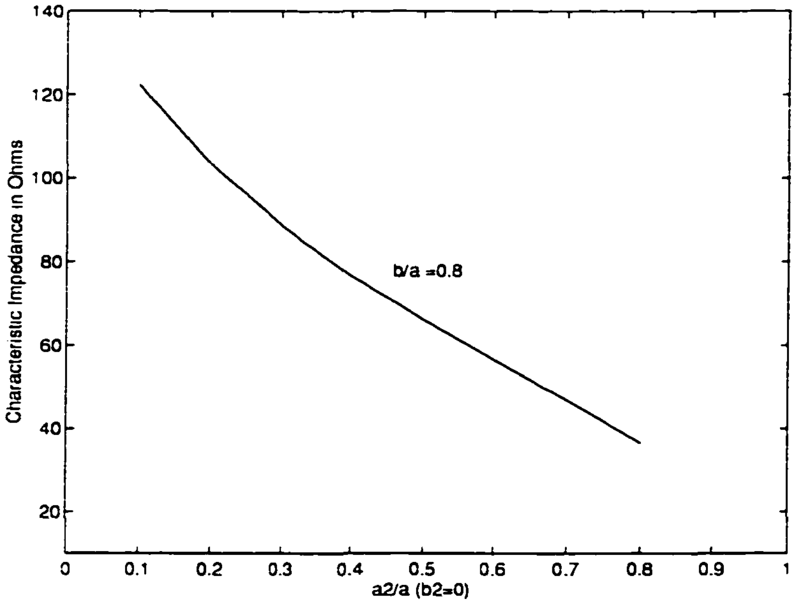

Figure 2.9: Characteristic Impedance of RCL's

waveguide. But the axes are interchanged. This change is applied to the analysis in section 2.3 to determine the corresponding eigenvalues. For the case of $TE_{odd,odd}$ and $TM_{odd,odd}$ symmetry (magnetic walls along both the lines of symmetry), the equations for potential functions are given as:

$$\psi^{(e1)} = \sum_{m=1}^{M} A_m \sin\frac{m\pi y}{q}\cos(k_{x_m}^{(1e)}(x - a/2)) \tag{2.54}$$

$$\psi^{(e2)} = \sum_{n=1}^{N} B_n \sin\frac{(2n-1)\pi y}{2u}\frac{1}{k_{x_n}^{(2e)}}\sin(k_{x_n}^{(2e)}x) \tag{2.55}$$

$$\psi^{(h1)} = \sum_{m=0}^{M} C_m \cos\frac{m\pi y}{q}\frac{1}{k_{x_m}^{(1h)}}\sin(k_{x_m}^{(1h)}(x - a/2)) \tag{2.56}$$

$$\psi^{(h2)} = \sum_{n=0}^{N} B_n \cos\frac{(2n+1)\pi y}{2u}\cos(k_{x_n}^{(2h)}x) \tag{2.57}$$

The procedure described for the eigenvalue analysis has been followed once again to evaluate the cutoff frequencies of $TM_{odd,odd}$ and $TE_{odd,odd}$ modes. The eigenvalues for a case of rectangular coaxial line with a very thin inner conductor, called the Transverse Electromagnetic cell (TEM cell), has been evaluated and compared with the FEM [54] and the TLM [55] method. It should however be noted that the FEM and TLM methods have assumed the thickness of the center conductor zero although, physically, the thickness of center conductor of the TEM cell is finite. This assumption is made because otherwise a fine discretization is necessary in order to account for the finite thickness of the inner conductor while using these methods. This may increase the memory requirements and cpu time needed to solve the problem. However, an approximation of zero conductor thickness does not introduce an appreciable error in the cutoff frequencies of the TEM cell.

The values denoted '*' in the Table 2.3 indicate that the cut-off frequencies have been evaluated using waveguide formula because the line of symmetry for those modes are electric wall along the direction of the center conductor. As the thickness of the center conductor is assumed to be zero, it is appropriate to use the waveguide cut-off formula. The analysis for this symmetry however, have been evaluated using the rigorous procedure described, as the inner conductor thickness is assumed non-zero. The potential functions for such a symmetry have been given below.

$$\psi^{(e1)} = \sum_{m=1}^{M} A_m \sin\frac{m\pi y}{q}\frac{1}{k_{xm}^{(1e)}}\sin(k_{xm}^{(1e)}(x-a/2)) \tag{2.58}$$

$$\psi^{(e2)} = \sum_{n=1}^{N} B_n \sin\frac{n\pi y}{u}\frac{1}{k_{xn}^{(2e)}}\sin(k_{xn}^{(2e)}x) \tag{2.59}$$

$$\psi^{(h1)} = \sum_{m=0}^{M} C_m \cos\frac{m\pi y}{q}\cos(k_{xm}^{(1h)}(x-a/2)) \tag{2.60}$$

$$\psi^{(h2)} = \sum_{n=0}^{N} D_n \cos\frac{n\pi y}{u}\cos(k_{xn}^{(2h)}x) \tag{2.61}$$

The eigenvalue solutions for a TEM cell using MMM are in close agreement with that of the FEM and TLM.

Mode Pattern	TLM method[55] fc in MHz	FEM method[54] fc in MHz	MMM in MHz
$TE_{0,1}$	15.1	15.5	16.0
$TE_{1,0}$	24.6^*	24.6^*	24.6
$TE_{1,1}$	31.1	31.2	31.4
$TE_{0,2}$	41.1^*	41.1^*	41.1
$TE_{2,1}$	45.4	45.3	46.1
$TE_{1,2}$	47.8^*	47.8^*	47.8
$TE_{2,0}$	49.2^*	49.2^*	49.2
$TE_{0,3}$		54.2	54.4
$TE_{1,3}$		62.1	62.5
$TE_{2,2}$		64.1^*	64.1
$TE_{2,3}$		73.2	72.4
$TE_{3,0}$		73.8^*	73.8
$TE_{3,1}$		76.9	75.6
$TE_{3,2}$		84.4^*	84.4
$TE_{3,3}$		87.2	87.1
TM_{11}	47.6	47.9	47.5
TM_{12}	47.8	47.8^*	47.9
TM_{21}		64.3	63.0
TM_{22}		64.1^*	64.1
TM_{13}			82.0

Table 2.3: Cutoff frequencies of TEM cell of dimensions a=6.1m, b=7.3m, a2=4.06m, b2=0.157cm

2.4.2 Step 2: Analysis of a step discontinuity in rectangular coaxial line

A symmetric step discontinuity in circular coaxial line has been analyzed considering only TEM and $TM_{0,m}$ modes [56,57]. In the case of rectangular coaxial line discontinuity shown in Figure 2.8, however, an incident TEM mode which has magnetic walls along the two lines of symmetry, will excite $TE_{odd,odd}$ and $TM_{odd,odd}$ modes.

The cut off frequency of higher order modes with magnetic walls along the lines of symmetry is found using the steps discussed above for the eigenvalue analysis. The coefficients for the potential functions in the equations (2.54), (2.55), (2.56), (2.57) can be obtained by solving the homogeneous characteristic equation (2.41) at the cut off frequency. This is achieved by initially setting one of the coefficients in either subregions to unity and then calculating the remaining coefficients. The potential functions in the RCL cross-section can be written as the sum of the potential functions in the two subregions in which they satisfy the boundary conditions. The respective modal amplitude coefficients are obtained at all the cutoff wavenumbers. For instance, the magnetic potential functions are written as the sum of the potential function in the subregions 1 and 2 as given in equations (2.56) and (2.57) with their appropriate modal amplitude coefficients and the value of k_x obtained from the eigenvalue analysis. These amplitude coefficients are then normalized so that the magnitude of the power carried by each of the TE and TM modes is 1 watt. This is done by adding the power evaluated in the subregions 1 and 2 for that mode. For the TEM mode which is included as a special case of TM mode in the discontinuity analysis, the power carried is determined by V_o^2/Z_o where Z_o is the characteristic impedance. It can be noted that the TEM fields in a rectangular coaxial line is represented as a series in subregion 2 and is truncated suitably.

At the junction between two rectangular coaxial lines with different dimensions, there are subregions on both sides where the tangential components of electric and magnetic fields have to be matched. Hence, a small length of a waveguide of the dimension of the outer coaxial line is assumed initially (Figure 2.10) in the analyis of the discontinuity [49]. The tangential components of E-fields at the junction between the rectangular coaxial line and the waveguide are matched. A set of equations is obtained using the property of orthogonality of modes, and the coupling integrals

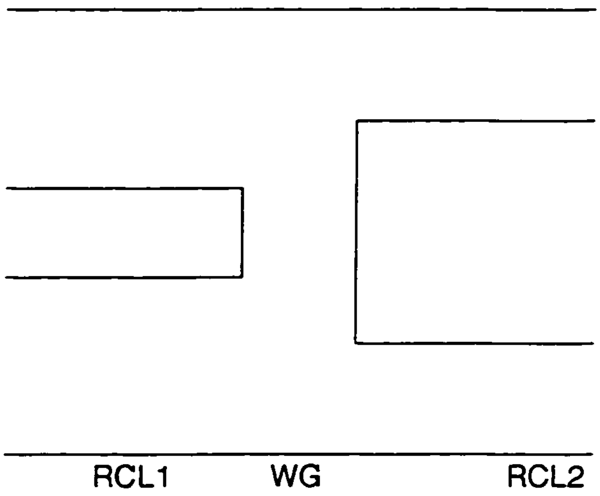

Figure 2.10: A junction between two RCL with an assumed waveguide section in between them

can all be evaluated analytically. The H-field matching condition is obtained by transposing the matrices that result from the matching condition of the E-field as discussed in section 2.2. The generalized S-matrix of the step RCL discontinuity (RCL1 - RCL2) is obtained from the above S-matrices for the two junctions (RCL1-WG and WG-RCL2) by letting the waveguide length, as shown in Figure 2.10, go to zero. It should be noted that there is no TEM mode in the empty waveguide but while cascading generalized scattering matrices, the TEM mode S-parameters from one RCL to another RCL is obtained because the TEM mode is present in both the RCLs.

A RCL cascaded step discontinuity has been analyzed using the above procedure and compared with the literature. The characteristic impedance of the two lines are nearly 50 Ohms and 25 Ohms (Table 2.2). The outer conductor dimensions of the 50 Ohm and 25 Ohm line are 11 × 10 mm. The inner conductor dimensions of the 25 Ohm line is 7 × 6 mm and that of the 50 Ohm line is 4.16 × 4.16 mm. The length of the 25 Ohm section is 20mm. The S-parameters of such a cascaded step discontinuity

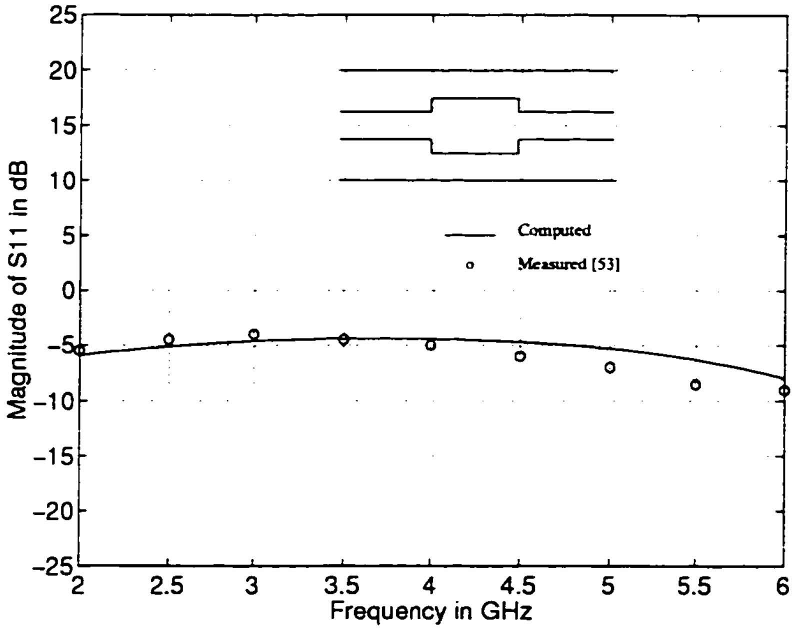

Figure 2.11: Magnitude of reflection coefficient of cascaded inner conductor step discontinuity in RCL (50 Ohm RCL input/output to 25 Ohm of length 20mm)

are compared with measured data available in [53]. A good agreement is found using the full-wave analysis as shown in Figures 2.11 and 2.12.

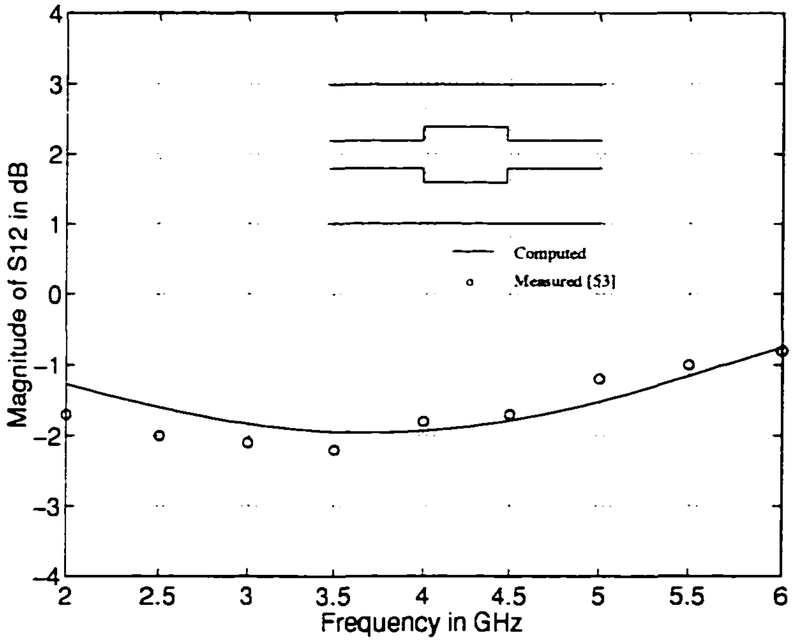

Figure 2.12: Magnitude of transmission coefficient of cascaded inner conductor step discontinuity in RCL (50 Ohm RCL input/output to 25 Ohm of length 20mm)

Chapter 3

Eigenvalue Analysis of Ridged Circular Waveguides

3.1 Introduction

An overview of the mode matching method with regard to the analysis of rectangular waveguide structures has been dealt with up to this point. This chapter deals with the eigenvalue analysis and the evaluation of characteristic impedance of certain types of ridged circular waveguides. As indicated earlier. the ridges have been shaped conically for mathematical ease in formulation. Ridged circular waveguides find application in filters. matching transformers. orthomode transducers. septum polarizers. magnetrons and gyratrons to name a few. A knowledge of the propagation characteristics and characteristic impedance of the individual waveguide section is of utmost importance in the design of these components.

This chapter is divided into two sections. The first section examines the technique to determine the eigenvalues of fundamental and various higher order transverse electric and transverse magnetic modes for different types of ridged circular waveguides. The second section deals with the evaluation of the characteristic impedance.

3.2 Eigenvalue analysis

3.2.1 Single ridged circular waveguide

To start with, we first consider the cross-section of the single ridged circular waveguide of Figure 3.1(a) and (b). The eigenvalues of double, triple and quadruple ridged circular waveguide can be easily derived by following the same theory below and considering electric wall(ew) and magnetic wall(mw) symmetry suitably. The eigenvalues of the orthogonal dominant modes and higher order modes of such a structure can be obtained from the solution of the Helmholtz equation in cylindrical coordinates.

$$\frac{1}{\rho}\frac{\partial}{\partial\rho}(\rho\frac{\partial\psi}{\partial\rho}) + \frac{1}{\rho^2}\frac{\partial^2\psi}{\partial\phi^2} + \frac{\partial^2\psi}{\partial z^2} + k^2\psi = 0 \tag{3.1}$$

Assuming propagation in the z direction, the structure as shown in Figure 3.1(a) can be divided into two homogeneous subregions. Solving the Helmholtz equation in each homogeneous subregion by applying the boundary condition, the potential function for subregions 1 and 2 of Figure 3.1(a) for TE modes can be written as follows:

$$\psi^{(1h)} = \sum_{n=r}^{N1} A_n J_n(k_c^h\rho)\begin{cases}\sin n\phi & r = 1 \text{ for mw}\\ \cos n\phi & r = 0 \text{ for ew}\end{cases} \tag{3.2}$$

$$\begin{aligned}\psi^{(2h)} &= \sum_{m=r}^{N2} C_m[J_l(k_c^h\rho)N_l'(k_c^h b) - J_l'(k_c^h b)N_l(k_c^h\rho)]\\ &\quad\cdot\begin{cases}\cos l(\phi-\theta) & r = 1,3,\ldots \text{ and } l = \frac{m\pi}{2(\pi-\theta)} \text{ for mw}\\ \cos l(\phi-\theta) & r = 0,1,\ldots \text{ and } l = \frac{m\pi}{\pi-\theta} \text{ for ew}\end{cases}\end{aligned} \tag{3.3}$$

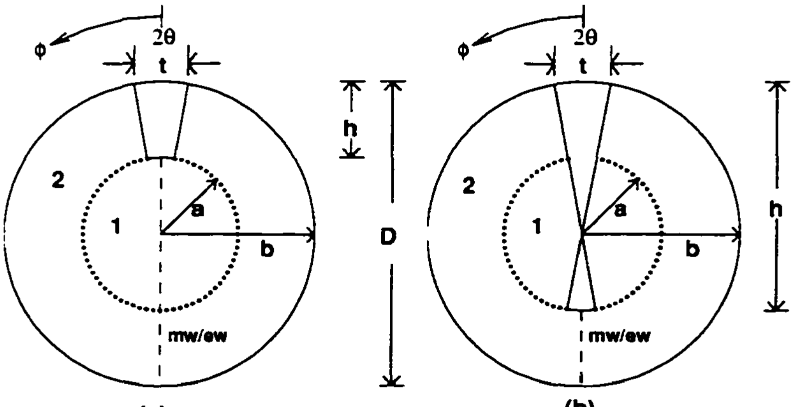

(a) (b)

Figure 3.1: Single ridged circular waveguide

The functions J_n are the Bessel functions of order n and N_l are the Neumann functions of non-integer order l. The unknown coefficients of the eigenfunctions are A_n and C_m and b is the radius of the circular waveguide.

Similarly, the potential functions for the TM modes for both symmetries are given by

$$\psi^{(1e)} = \sum_{n=r}^{N1} B_n J_n(k_c^e \rho) \begin{cases} \cos n\phi & r = 0 \text{ for mw} \\ \sin n\phi & r = 1 \text{ for ew} \end{cases} \tag{3.4}$$

$$\begin{aligned} \psi^{(2e)} &= \sum_{m=r}^{N2} D_m [J_l(k_c^e \rho) N_l(k_c^e b) - J_l(k_c^e b) N_l(k_c^e \rho)] \\ &\cdot \begin{cases} \sin l(\phi - \theta) & r = 1, 3, \ldots \text{ and } l = \frac{m\pi}{2(\pi - \theta)} \text{ for mw} \\ \sin l(\phi - \theta) & r = 1, 2, \ldots \text{ and } l = \frac{m\pi}{\pi - \theta} \text{ for ew} \end{cases} \end{aligned} \tag{3.5}$$

From the potential functions, the field components in each of the regions can be derived using Appendix D. The continuity condition of the tangential components of the electric and magnetic fields is then applied at the interface of the two subregions:

$$E_\phi^{(1)} = E_\phi^{(2)} \qquad \rho = a, \phi \in [\theta, 2\pi - \theta] \tag{3.6}$$

$$= 0 \qquad \rho = a, \phi \in [-\theta, \theta] \tag{3.7}$$

$$H_z^{(1)} = H_z^{(2)} \qquad \rho = a, \phi \in [\theta, 2\pi - \theta] \tag{3.8}$$

$$H_\phi^{(1)} = H_\phi^{(2)} \qquad \rho = a, \phi \in [\theta, 2\pi - \theta] \tag{3.9}$$

$$E_z^{(1)} = E_z^{(2)} \qquad \rho = a, \phi \in [\theta, 2\pi - \theta] \tag{3.10}$$

$$= 0 \qquad \rho = a, \phi \in [-\theta, \theta] \tag{3.11}$$

Equating E_ϕ and H_z for TE modes and E_z and H_ϕ for TM modes at the interface of the two subregions and using the orthogonality property, a system of linear equations of infinite size as a function of k_c is obtained. The size of this system of equations is made finite depending on the truncation index $N1$ and $N2$. They represent the number of modes included for the analysis in the two subregions. The ratio between the number of modes in the two subregions is chosen to be close to the ratio of the angular widths of region 1 and region 2 to avoid relative convergence problems [47]. The set of linear homogeneous characteristic equations of finite size is of the form:

$$F[X] = 0 \tag{3.12}$$

where $[X]$ is a vector of unknown coefficients of the potential functions and F, the characteristic matrix, is a function of k_c. If the matrix F is written in terms of submatrices P, Q, R and S as in equation 2.34 with $[X]$ as a vector of the unknown coefficients of the potential functions, then the elements of the submatrices of F for TE modes are as follows:

$$P_{nm} = \begin{cases} J_n'(k_c^h b)\pi & \text{if } n = m \\ 0 & \text{otherwise} \end{cases} \tag{3.13}$$

$$\begin{aligned} Q_{nm} &= [J_l'(k_c^h a)N_l'(k_c^h b) - J_l'(k_c^h b)N_l'(k_c^h a)] \\ &\quad - \int_{\theta}^{2\pi-\theta} \cos\frac{m\pi(\phi-\theta)}{2(\pi-\theta)} \sin n\phi d\phi \end{aligned} \tag{3.14}$$

$$S_{nm} = \begin{cases} (\pi-\theta)[J_l(k_c^h a)N_l'(k_c^h b) - J_l'(k_c^h b)N_l(k_c^h a)] & \text{if } m = n \\ 0 & \text{otherwise} \end{cases} \tag{3.15}$$

$$R_{nm} = J_n(k_c^h a) \int_{\theta}^{2\pi-\theta} \sin n\phi \cos\frac{m\pi(\phi-\theta)}{2(\pi-\theta)} d\phi \tag{3.16}$$

The eigenvalues of the system are obtained either by searching for the minimum of the smallest singular value of the characteristic matrix or by searching for the zeros of the determinant(det[F]=0). The SVD technique has been used here for evaluation of the eigenvalues.

There are two special cases for the ridge depth that have to be distinguished.

3.2.1.1 Special Case 1 : Ridge depth = Radius

In this case, subregion 1 vanishes when the ridge depth is equal to the radius of the circular waveguide. The potential functions of the TE modes for this case is similar to [58].

$$\psi = J_n(k_c\rho)\cos n(\phi - \theta) \tag{3.17}$$

where, $n = 0, \frac{\pi}{2(\pi-\theta)}, \frac{2\pi}{2(\pi-\theta)}, \ldots$

The cutoff wavelength for the dominant and higher order modes can now simply be obtained from the search for the zeros of the function $J_n'(k_c b)$ (as this makes $E_\phi = 0$ for $\rho = b$) instead of using equation 3.12.

3.2.1.2 Special Case 2 : Ridge depth > Radius

When the ridge depth is greater than the radius of the circular waveguide (Figure 3.1(b)). the potential functions for TE modes for both symmetries is the same as equation (3.3) for subregion 2. while for region 1 it is

$$\psi^{(1h)} = \sum_{n=0}^{N1} A_n J_q(k_c^h \rho) \cos \frac{n\pi(\phi-\theta)}{(\pi-2\theta)} \tag{3.18}$$

where $q = \frac{n\pi}{(\pi-2\theta)}$. In contrast to case 1 the cutoff frequencies are now computed from equation 3.12.

Similarly for the TM modes. the potential function in subregion 2 is the same as equation (3.5). while in region 1 for both the symmetries it is

$$\psi^{(1e)} = \sum_{n=0}^{N1} A_n J_q(k_c^e \rho) \sin \frac{n\pi(\phi-\theta)}{(\pi-2\theta)} \tag{3.19}$$

The cutoff frequencies for all the symmetries have been determined for the single ridged circular waveguide. The nomenclature of $TE_{n,m}$ and $TM_{n,m}$ modes of the empty circular waveguide is maintained even though the presence of metallic ridges distorts the field distribution of these modes. Using the above mode nomenclature means nothing else than that those modes can be traced back to the corresponding ones in the empty (undisturbed) circular waveguide.

Figure 3.2 shows the cutoff characteristics of a single ridged circular waveguide. The results of the fundamental mode have been compared with a finite element solution [59] and good agreement was found. It is sufficient to include 7 mode in each of the subregions to achieve convergence of the eigenvalues shown in Figure 3.2. It is observed that the cutoff frequencies of the orthogonally polarized degenerate TE modes of the circular waveguide move in the opposite direction when the penetration depth of the ridge increases. For the polarization with $E_{\rho_{max}}$ along the direction of the

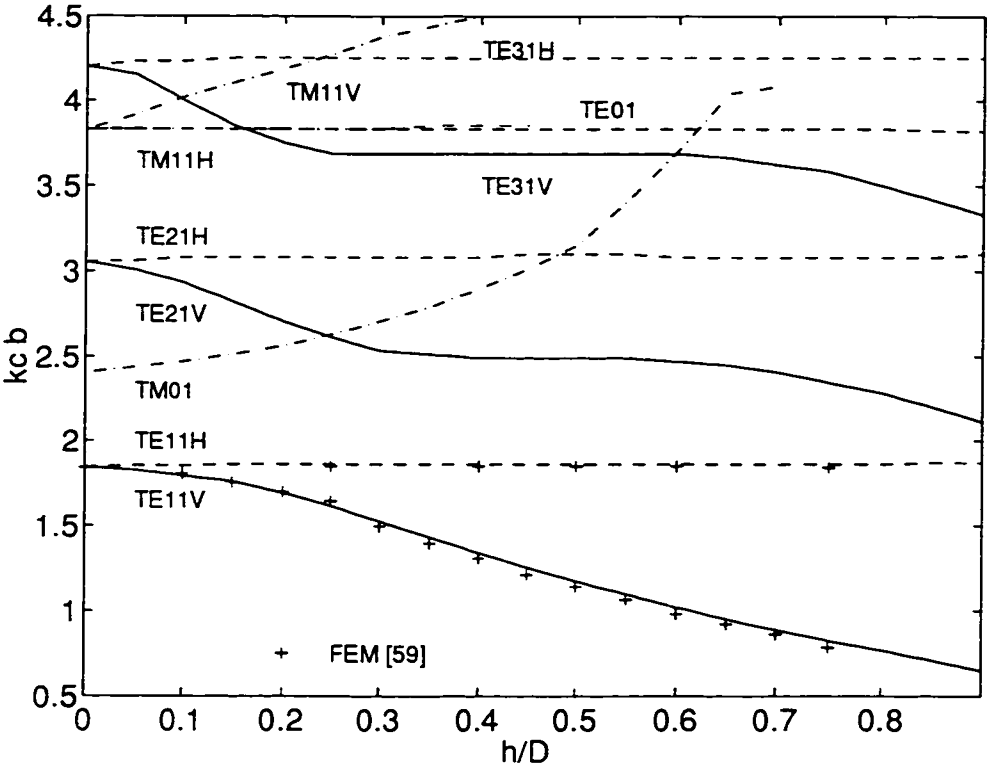

Figure 3.2: Cutoff characteristics of single ridged circular waveguide (t/D=0.04)

ridge, the loading by the ridge is capacitive while for the polarization with $E_{\rho_{max}}$ perpendicular to the ridge the loading is inductive. Since the ridge is positioned to load either inductively or capacitively for the orthogonal polarizations of the TE modes, mode splitting occurs. The mode splitting phenomenon for TE and TM modes is represented as V(Vertical polarization or magnetic wall symmetry) and H(Horizontal polarization or electric wall symmetry) in the Figure 2.2 and the following figures of this chapter. Since the $TE_{0,m}$ modes and $TM_{0,m}$ modes are axially symmetric, they exist only for electric wall symmetry or magnetic wall symmetry, respectively. Therefore, those modes are not identified by V or H index. For the TM modes, the ridges act as inductive load for both the symmetries and hence the cutoff frequency increases with the penetration of the ridge. An interesting conclusion that is of direct importance in the design of septum polarizers can be drawn from Figure 3.2. In [59] it was reported that the low port isolation of a septum polarizer was due to the onset of the $TM_{0,1}$ mode. However, as Figure 3.2 clearly shows, by exceeding certain ridge penetration depths, the cutoff frequency of the $TE_{2,1}V$ mode is lower than that of the $TM_{0,1}$ and it is rather this mode that is responsible for the limited port isolation reported in [59].

3.2.2 Double ridged circular waveguide

The double ridged circular waveguide cross-section is as shown in Figure 3.3. Unlike in single ridged circular waveguide, an additional line of symmetry can be considered here making it possible to analyze only one quarter of the cross-section. There are four possible combinations of electric and magnetic walls along the lines of symmetry. However, the most important symmetry is the one with magnetic wall along the direction of the double ridges and electric wall perpendicular to it. This structure is useful in the design of components like bandpass filters and transformers. Analysis of all the four possible symmetries is essential for the design of a polarizers where the ridges are placed at 45° to the $\phi = 0^\circ$ or the $\phi = 180^\circ$ planes.

The potential functions for TE modes in subregions 1 and 2 for a double ridged circular waveguide for all possible symmetries is as follows:

$$\begin{aligned}\psi^{(1h)} &= \sum_{n=r}^{N1} A_n J_n(k_c^h \rho) \\ &\cdot \begin{cases} \sin n\phi & r = 1,3,\ldots \text{ for mw\&ew},\ r = 2,4,\ldots \text{ for mw\&mw} \\ \cos n\phi & r = 0,2,\ldots \text{ for ew\&ew},\ r = 1,3,\ldots \text{ for ew\&mw} \end{cases}\end{aligned} \tag{3.20}$$

In the above and following set of equations it should be noted that the first line of symmetry is the one that is along the direction of the ridge and the next one

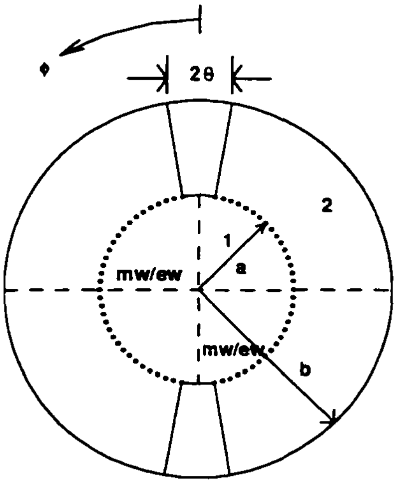

Figure 3.3: Double ridged circular waveguide

is perpendicular to the ridge. For instance, mw&ew in equation (3.20) indicate that there is a magnetic wall along the direction of the ridge and electric wall perpendicular to the ridge.

$$\psi^{(2h)} = \sum_{m=r}^{N2} C_m[J_l(k_c^h\rho)N_l'(k_c^h b) - J_l'(k_c^h b)N_l(k_c^h\rho)]$$

$$\cdot\begin{cases} \cos l(\phi-\theta) & r=0,1,\dots \text{ and } l=\frac{m\pi}{\pi/2-\theta} \text{ for mw\&ew or ew\&ew} \\ \cos l(\phi-\theta) & r=1,3,\dots \text{ and } l=\frac{m\pi}{\pi-2\theta} \text{ for ew\&mw or mw\&mw} \end{cases} \quad (3.21)$$

Similarly, the potential functions for the TM modes for all the symmetries are given by

$$\psi^{(1e)} = \sum_{n=r}^{N1} B_n J_n(k_c^e\rho)$$

$$\cdot\begin{cases} \cos n\phi & r=1,3,\dots \text{ for mw\&ew, } r=0,2,4,\dots \text{ for mw\&mw} \\ \sin n\phi & r=1,2,\dots \text{ for ew\&ew, } r=1,3,\dots \text{ for ew\&mw} \end{cases} \quad (3.22)$$

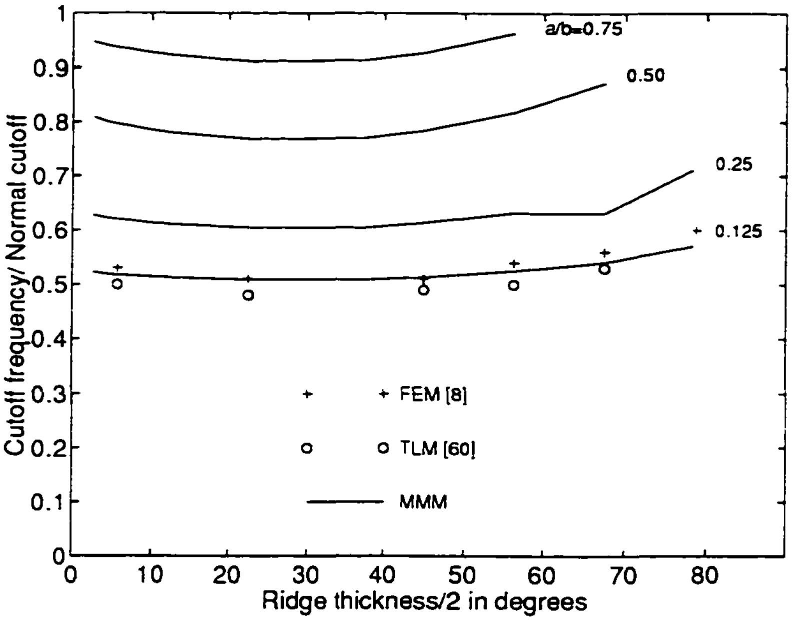

Figure 3.4: Cutoff characteristics of fundamental mode of double ridged circular waveguide

$$\psi^{(2e)} = \sum_{m=r}^{N2} D_m \left[J_l(k_c^e \rho) N_l(k_c^e b) - J_l(k_c^e b) N_l(k_c^e \rho) \right]$$

$$\cdot \begin{cases} \sin l(o-\theta) & r = 1,2,\dots \text{ and } l = \frac{m\pi}{(\pi/2-\theta)} \text{ for mw\&ew or ew\&ew} \\ \sin l(o-\theta) & r = 1,3,\dots \text{ and } l = \frac{m\pi}{\pi-2\theta} \text{ for ew\&mw or mw\&mw} \end{cases} \quad (3.23)$$

Figure 3.4 shows the fundamental mode (E field parallel to the ridges) cutoff characteristics of a double ridge circular waveguide for varying ridge parameters. The results are again in good agreement with the FEM [8] and TLM [60] solutions. As illustrated in the Figure 3.4, the effect of ridge thickness on the cutoff frequency of the fundamental mode is relatively small. The variation of the cut off frequency of the higher order modes with respect to ridge penetration depth is shown in Figure 3.5. Mode splitting of the orthogonally polarized $TE_{1,1}$, $TE_{2,1}$ and $TM_{1,1}$ is clearly shown. Also here the splitting of these modes is due to the same reasons as explained for single ridged waveguide.

3.2.3 Triple ridged circular waveguide

The triple ridged circular waveguide has one line of symmetry as in single ridged circular waveguide. But the results of the eigenvalues are interesting to note. There are three subregions in this structure as shown in Figure 3.6 and hence the size of characteristic matrix becomes larger.

The electric and magnetic potential functions for the subregion 1 is the same as in equations (3.2) and (3.4) for the single ridged circular waveguide. However, for the subregions 2 and 3 they are as follows:

$$\begin{aligned} \psi^{(2h)} &= \sum_{m=r}^{N2} C_m[J_l(k_c^h\rho)N_l'(k_c^hb) - J_l'(k_c^hb)N_l(k_c^h\rho)] \\ &\quad \cdot \begin{cases} \sin l\phi & r = 1, 3, \dots \text{ and } l = \frac{m\pi}{\phi_o} \text{ for mw} \\ \cos l\phi & r = 0, 1, \dots \text{ and } l = \frac{m\pi}{\phi_o/2} \text{ for ew} \end{cases} \end{aligned} \tag{3.24}$$

$$\begin{aligned} \psi^{(3h)} &= \sum_{m=r}^{N2} C_m[J_l(k_c^h\rho)N_l'(k_c^hb) - J_l'(k_c^hb)N_l(k_c^h\rho)] \\ &\quad \cdot \begin{cases} \cos l(\phi - \phi_o/2 - 2\theta) & r = 0, 1, \dots \text{ and } l = \frac{m\pi}{\phi_o} \text{ for mw} \\ \cos l(\phi - \phi_o/2 - 2\theta) & r = 0, 1, \dots \text{ and } l = \frac{m\pi}{\phi_o} \text{ for ew} \end{cases} \end{aligned} \tag{3.25}$$

$$\begin{aligned} \psi^{(2e)} &= \sum_{m=r}^{N2} D_m[J_l(k_c^e\rho)N_l(k_c^eb) - J_l(k_c^eb)N_l(k_c^e\rho)] \\ &\quad \cdot \begin{cases} \cos l\phi & r = 1, 3, \dots \text{ and } l = \frac{m\pi}{\phi_o} \text{ for mw} \\ \sin l\phi & r = 2, 4, \dots \text{ and } l = \frac{m\pi}{\phi_o} \text{ for ew} \end{cases} \end{aligned} \tag{3.26}$$

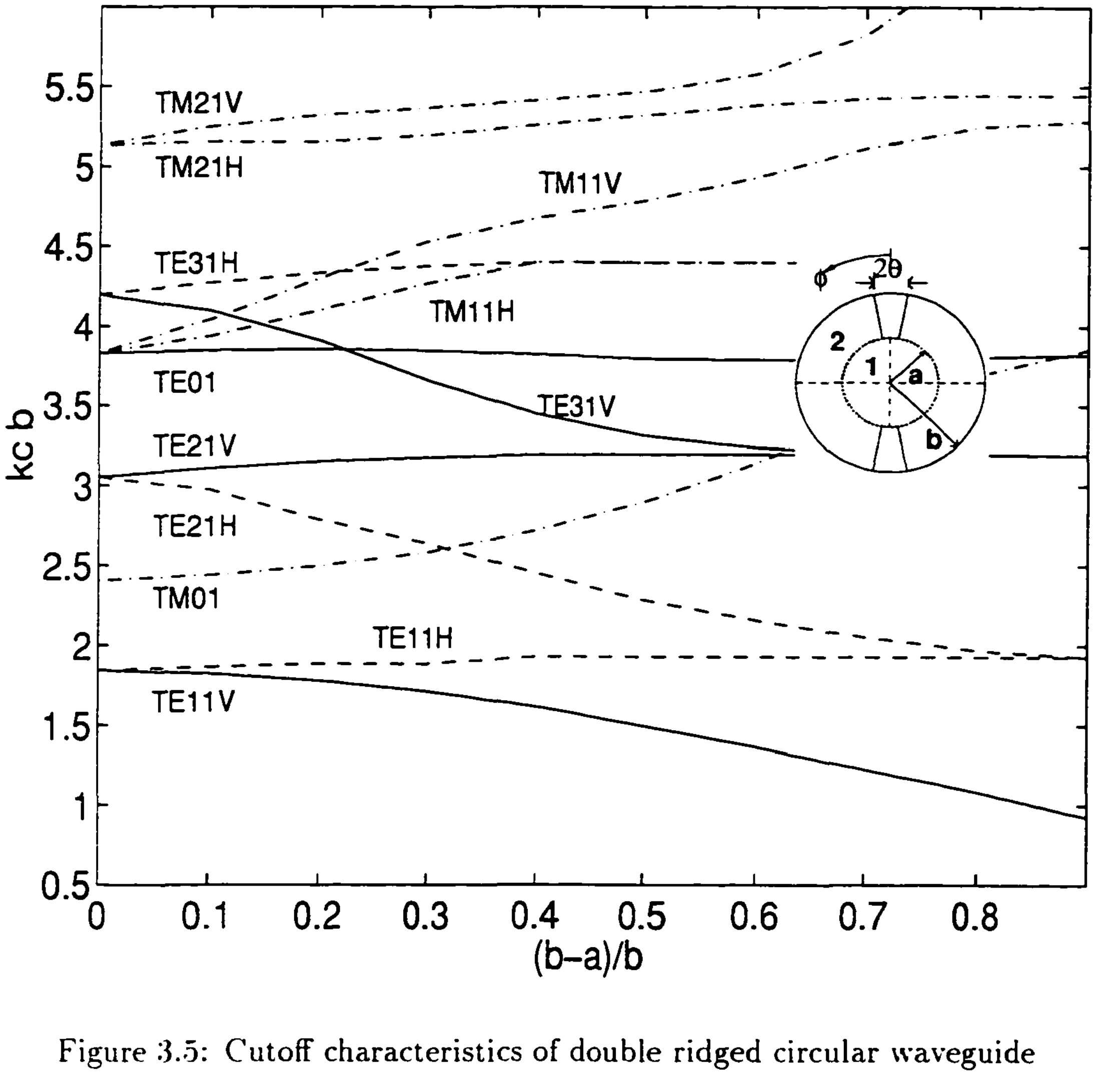

Figure 3.5: Cutoff characteristics of double ridged circular waveguide

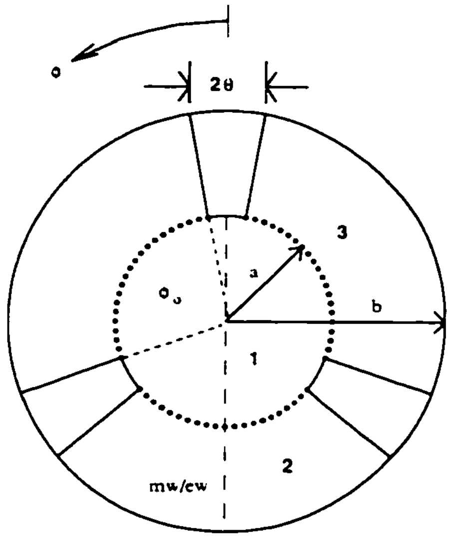

Figure 3.6: Triple ridged Circular waveguide

$$v^{(3e)} = \sum_{m=r}^{N2} D_m[J_l(k_c^e\rho)N_l(k_c^e b) - J_l(k_c^e b)N_l(k_c^e\rho)]$$

$$\cdot\begin{cases} \sin l(\phi - \phi_o/2 - 2\theta) & r = 1,2,\ldots \text{ and } l = \frac{m\pi}{\phi_o} \text{ for mw} \\ \sin l(\phi - \phi_o/2 - 2\theta) & r = 1,2,\ldots \text{ and } l = \frac{m\pi}{\phi_o} \text{ for ew} \end{cases} \qquad (3.27)$$

where ϕ_o is as shown in Figure 3.6. Alternatively, the triple ridged circular waveguide can be viewed as 3 slots of 120 degree. Since the structure is periodic, the field component at the boundary between two slots can be written as:

$$v(r,\phi + \frac{2\pi}{3}) = v(r,\phi)e^{-j2\pi k/3} \qquad (3.28)$$

In general for a structure with P slots,

$$v(r,\phi + \frac{2\pi}{P}) = v(r,\phi)e^{-j2\pi k/P} \qquad (3.29)$$

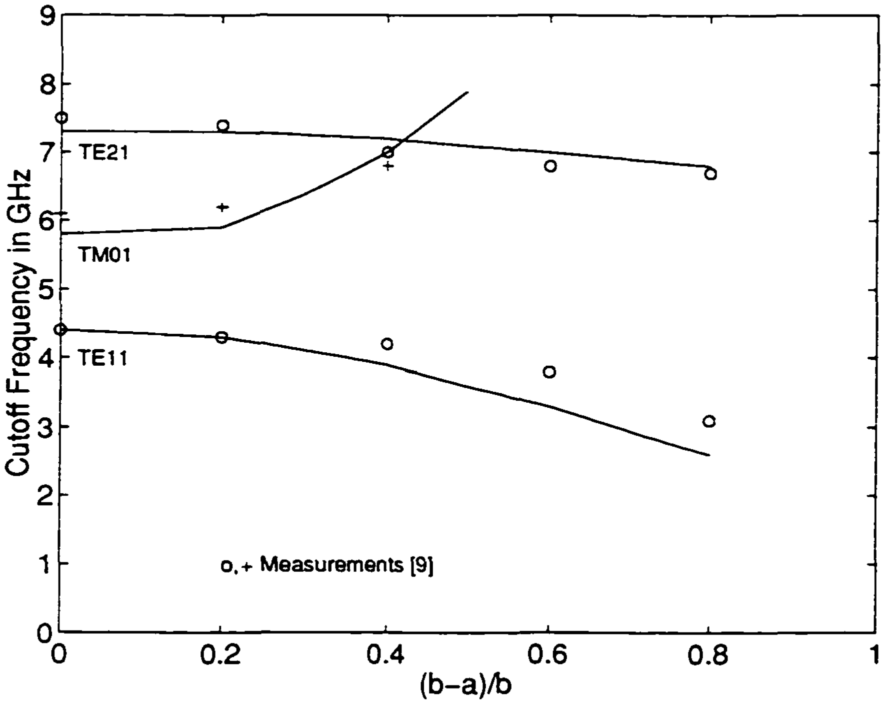

Figure 3.7: Cutoff characteristics of triple ridged circular waveguide

Since the structure closes on itself, $v(r, 2\pi) = v(r, 0)$. Hence for a triple ridged waveguide k in equation 3.28 takes the integer values 1,2 and 3. For the boundary conditions with $k = 1$ and $k = 2$, the phase of the field at one edge of the slot leads or lags the other edge of the slot by 120 degree. Hence for the conditions $k = 1$ and $k = 2$, the eigenvalue solutions obtained are the same. From the boundary condition $k = 3$ the axisymmetric modes are obtained. This implies that the modes of orthogonal polarizations are degenerate.

The cutoff frequency variation of a triple ridged circular waveguide versus ridge penetration depth is shown in Figure 3.7. Also here a good agreement with measurements [9] is observed. The bandwidth of the triple ridged circular waveguide is the largest of all the cases investigated in this chapter since the modes do not split.

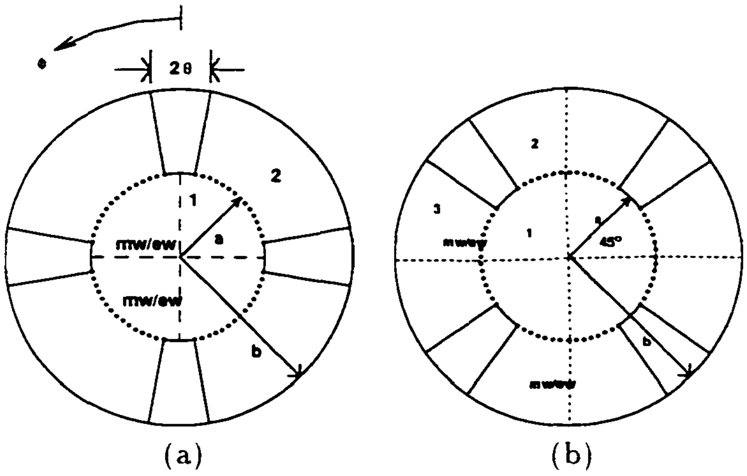

(a) (b)

Figure 3.8: (a)Quadruple ridged circular waveguide (b) Slotted circular waveguide

3.2.4 Quadruple ridged circular waveguide

It is sufficient to analyze one quarter of the cross-section of a quadruple ridged circular waveguide (Figure 3.8(a)) just like the double-ridged circular waveguide. However, it is important to note that the symmetry planes can be rotated by 45 degrees and the quadruple ridged waveguide appears as in Figure 3.8(b) which can be regarded as a slotted circular waveguide.

The electric and magnetic potential functions in subregion 1 of the quadruple ridged circular waveguide of Figure 3.8(a) are the same as in equations (3.20) and (3.21) of a double ridged circular waveguide. However, the potential functions in subregion 2 are below:

$$\begin{aligned}\psi^{(2h)} &= \sum_{m=r}^{N2} C_m[J_l(k_c^h\rho)N_l'(k_c^h b) - J_l'(k_c^h b)N_l(k_c^h\rho)]\cos l(\phi-\theta) \\ & r = 0, 1, \dots \text{ and } l = \frac{m\pi}{\pi/2-\theta} \text{ for all polarizations} \qquad (3.30)\end{aligned}$$

$$\psi^{(2e)} = \sum_{m=r}^{N2} D_m[J_l(k_c^e\rho)N_l(k_c^e b) - J_l(k_c^e b)N_l(k_c^e\rho)]\sin l(\phi - \theta)$$

$$r = 1, 2, \ldots \text{ and } l = \frac{m\pi}{(\pi/2-\theta)} \text{ for all polarizations} \qquad (3.31)$$

The number of subregions in the case of slotted circular waveguide (Figure 3.8(b)) is three and hence the potential functions and the characteristic matrix differ from the above. But the results of the eigenvalue analysis are just the same as for the case of a quadruple ridged circular waveguide due to the periodicity of the quadruple ridged structure. While certain modes are degenerate, some others get split. Physical reason for mode degeneracy and mode splitting of quadruple ridged circular waveguide are explained below. However, they can be explained from equation (3.29) as well.

The cutoff characteristics for the fundamental and higher order modes of a quadruple ridged circular waveguide is shown in Figure 3.9. The modes with magnetic wall along one line of symmetry and electric wall along the other line of symmetry ($TE_{1,1}$, $TE_{3,1}$, $TE_{1,2}$ etc. or in general $TE_{2m+1,n}$) have the same structure for both polarizations and hence the same eigenvalues. In contrast, the modes such as $TE_{2,1}$, $TE_{4,1}$ and $TE_{2,2}$ (in general, $TE_{2m,n}$) will have either electric or magnetic walls along both lines of symmetry for the orthogonal polarization and, therefore, the loading by the ridges is either inductive or capacitive and mode splitting occurs. In comparison to the single ridge and double ridge case, the loading is higher because of the presence of additional ridges and, hence, the cutoff frequencies of such modes increase or decrease more rapidly. This is of practical importance in applications where the $TE_{2m,n}$ modes can get excited. In such a case, the bandwidth is greatly limited when the penetration depth of the ridge is increased. This is in contrast to a structure involving total symmetry, for example an orthomode transducer [61] which is a quadruple ridged circular waveguide to circular waveguide transformer. Since in this case the stepped ridged discontinuities are symmetric, only $TE_{2m+1,n}$ and $TM_{2m+1,n}$ modes get excited. Hence, the performance of the orthomode transducer is not affected by the TE_{21} mode. Similar to the corresponding TE modes, the $TM_{1,1}$, $TM_{3,1}$ modes (modes with magnetic wall along one line of symmetry and electric wall along the other) do not split up. However, modes like $TM_{2,1}$, $TM_{4,1}$ and $TM_{2,2}$ (modes with electric walls or magnetic walls along both lines of symmetry) do split up which is a phenomenon that has not been reported in [62,63]. But unlike for TE modes, the loading by the ridges is always inductive for TM modes and the loading is higher in comparison to the single and double ridged waveguide due to the presence of the additional ridges.

3.3 Characteristic Impedance

The characteristic impedance of the ridged circular waveguide can be obtained using the power-voltage definition:

$$Z_o = \frac{V^2}{2P} \tag{3.32}$$

The slot voltage for the double ridged and quadruple ridged waveguide can be obtained using the relation:

$$V = -2\int_0^a E_\rho^{(1)}|_{(\phi=0,z=0)} d\rho \tag{3.33}$$

For the fundamental mode, the slot voltage is as given below for one expansion term used in the region I of the double and quadruple rudged waveguide. The value of k_c in the following equation is that of the fundamental mode of the corresponding ridged circular waveguide as obtained from the eigenvalue analysis.

$$V = -2A_1\int_0^a J_1(k_c\rho)\frac{1}{\rho}d\rho \tag{3.34}$$

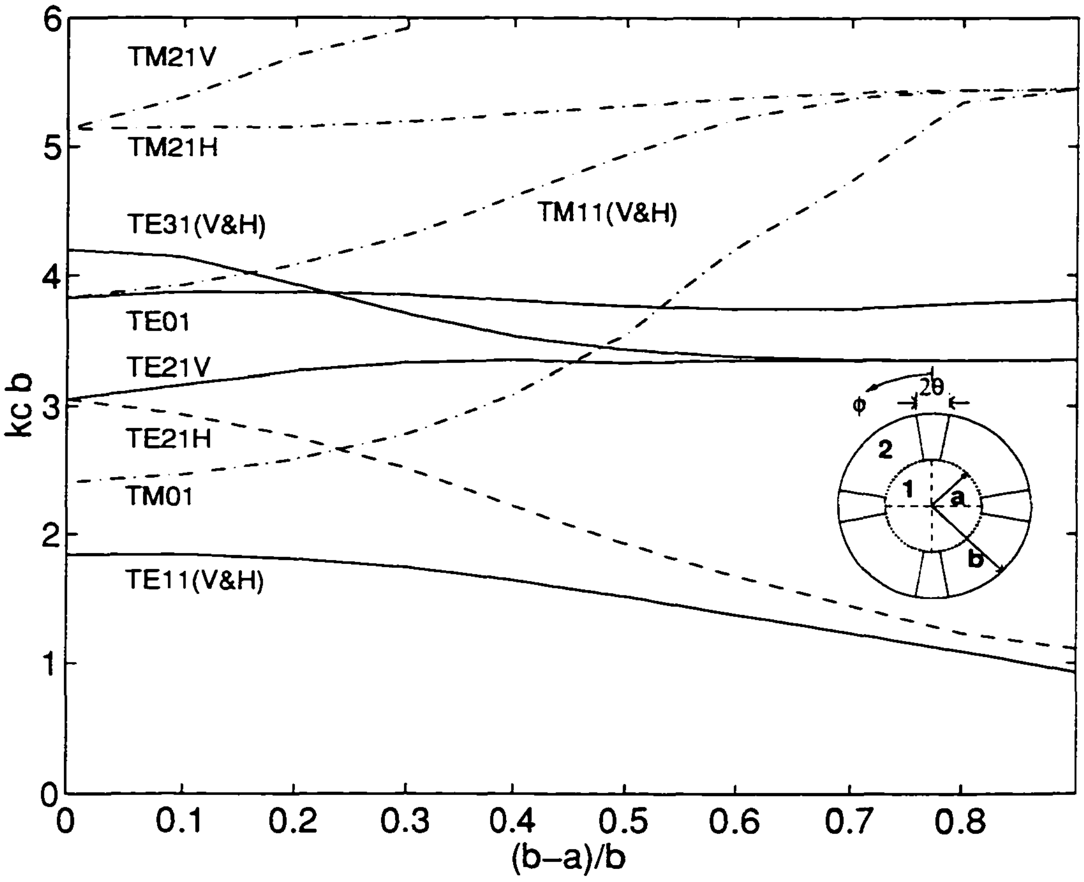

Figure 3.9: Cutoff characteristics of quadruple ridged circular waveguide

The integral of the above kind can be evaluated numerically using the recurrence relation of Bessel functions given in Appendix E. However, the integrand is not a function of the propagation constant and therefore need not be evaluated repeatedly at all the frequencies.

It is essential to know the relationship between the coefficients of the potential functions in the two subregions of the discontinuity for the evaluation of the power flowing in the guide. The coefficient of the potential function corresponding to the first expansion term in subregion 1 is assumed unity and then the coefficients for the fields for the fundamental mode are evaluated by solving the homogeneous characteristic equation (3.12) for k_c as determined in the eigenvalue analysis.

The average power P transported in the quarter cross-section of the ridged guide is determined using the relation

$$P = \frac{1}{2}\Re\sum_{q=1}^{2}\int_{S_q}(E^{(q)} \times H^{*(q)}).ds \tag{3.35}$$

There are only two subregions ($q = 1, 2$ for double and quadruple ridged circular waveguide) over which the surface integral is computed. The power in region 1 and 2 for the fundamental mode in double ridged circular waveguide is given as

$$P^{(1)} = \frac{\beta}{2\omega\mu}\sum_{n=1,3}^{N1} A_n^2 \int_0^a \int_0^{\pi/2}\left[\frac{1}{\rho^2}J_n^2(k_c\rho)\cos^2 no + J_n'^2(k_c\rho)\sin^2 no\right]\rho d\rho do \tag{3.36}$$

$$\begin{aligned} P^{(2)} = & \frac{\beta}{2\omega\mu}\left(\sum_{m=0}^{N2} C_m^2 \int_a^b \int_\theta^{\pi/2}\{[N_l'(k_cb)J_l'(k_c\rho) - J_l'(k_cb)N_l'(k_c\rho)]^2\cos^2\frac{l\pi(o-\theta)}{o_o}\right. \\ & \left. +\frac{1}{\rho^2}[J_l(k_c^h\rho)N_l'(k_c^hb) - J_l'(k_c^hb)N_l(k_c^h\rho)]^2 sin^2\frac{l\pi(o-\theta)}{o_o}\}\rho d\rho do\right) \end{aligned} \tag{3.37}$$

where. $l = m\pi/o_o$ and $o_o = \pi/2 - \theta$. The total power over the double ridged circular waveguide cross section is four times the the sum of $P^{(1)}$ and $P^{(2)}$. For the quadruple ridged circular waveguide the limits of o dependent integral in subregion 2 in equation (3.37) are from θ to $\pi/2 - \theta$ and $o_o = \pi/2 - 2\theta$

The characteristic impedance of double and quadruple ridged circular waveguide have not been investigated in the literature before but is of practical importance in the design of components such as transformers and orthomode transducers. The characteristic impedance of double ridged circular waveguide for various penetration depth is shown in Figure 3.10 and that of the quadruple ridged circular waveguide is shown in Figure 3.11. Only the impedance for the polarization parallel to the ridges is shown. because the double ridged circular waveguide is used in applications where this type of polarized mode propagates. Besides. the orthogonal polarization does not get excited at symmetric discontinuities. The variation of the characteristic impedance of the quadruple and double ridged circular waveguide with the ridge penetration depth at three different frequencies is shown in Figure 3.12. In comparison to the double ridged circular waveguide. the decrease in the characteristic impedance of the quadruple ridged waveguide with the increased ridge penetration depth is slightly higher because of the presence of the two additional ridges. Otherwise the characteristic impedance behaves very similar in both cases.

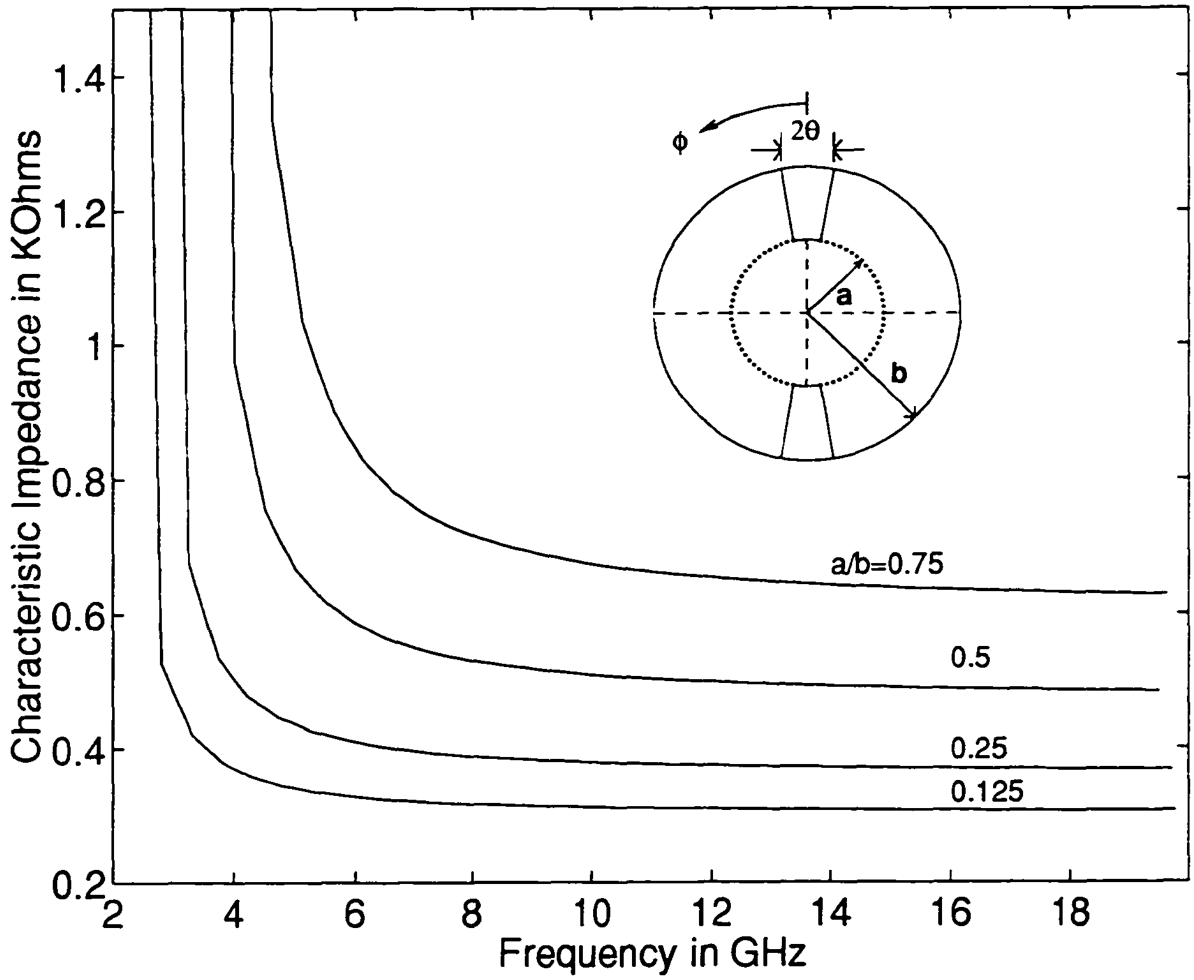

Figure 3.10: Characteristic impedance of double ridged circular waveguide, b=2cm, ridge thickness(2θ)=10 degree

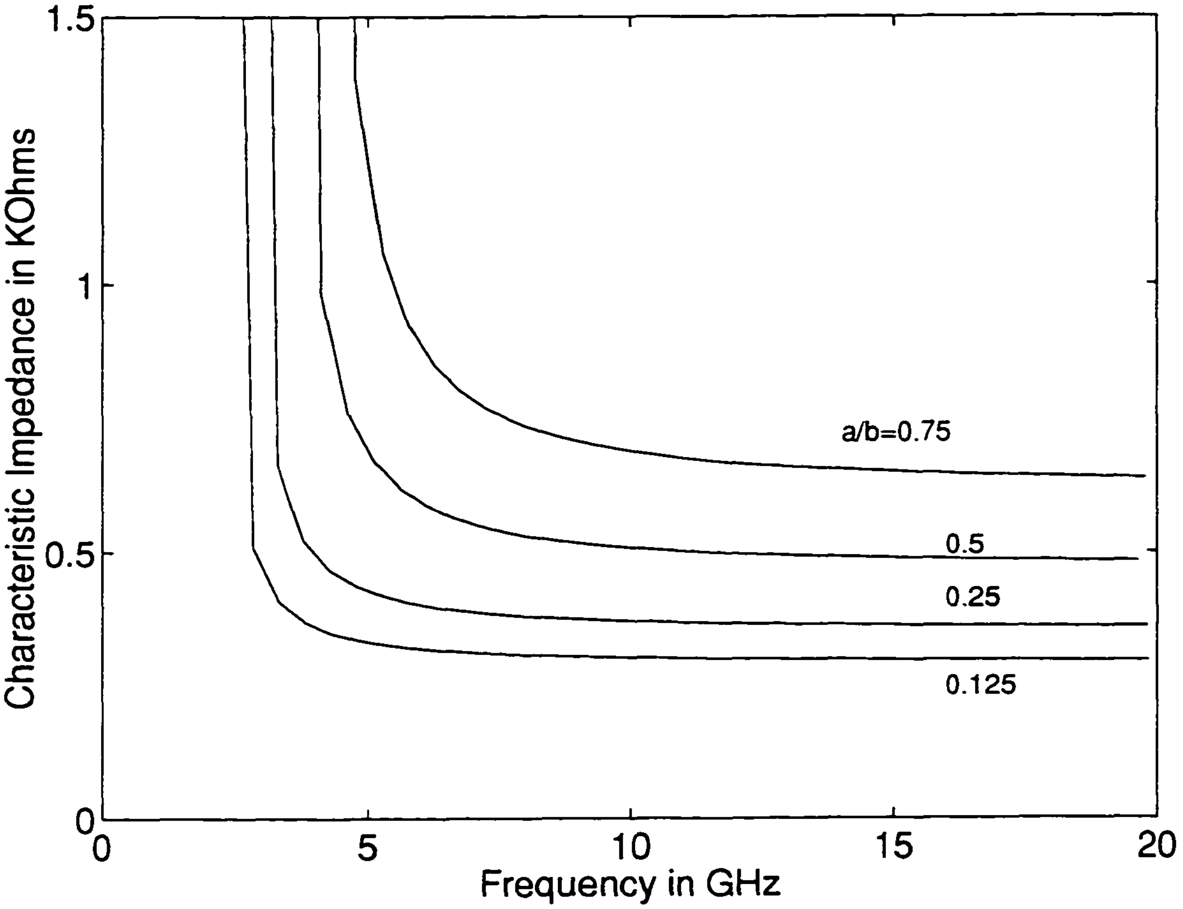

Figure 3.11: Characteristic impedance of quadruple ridged circular waveguide, b=2cm, ridge thickness=10 degree

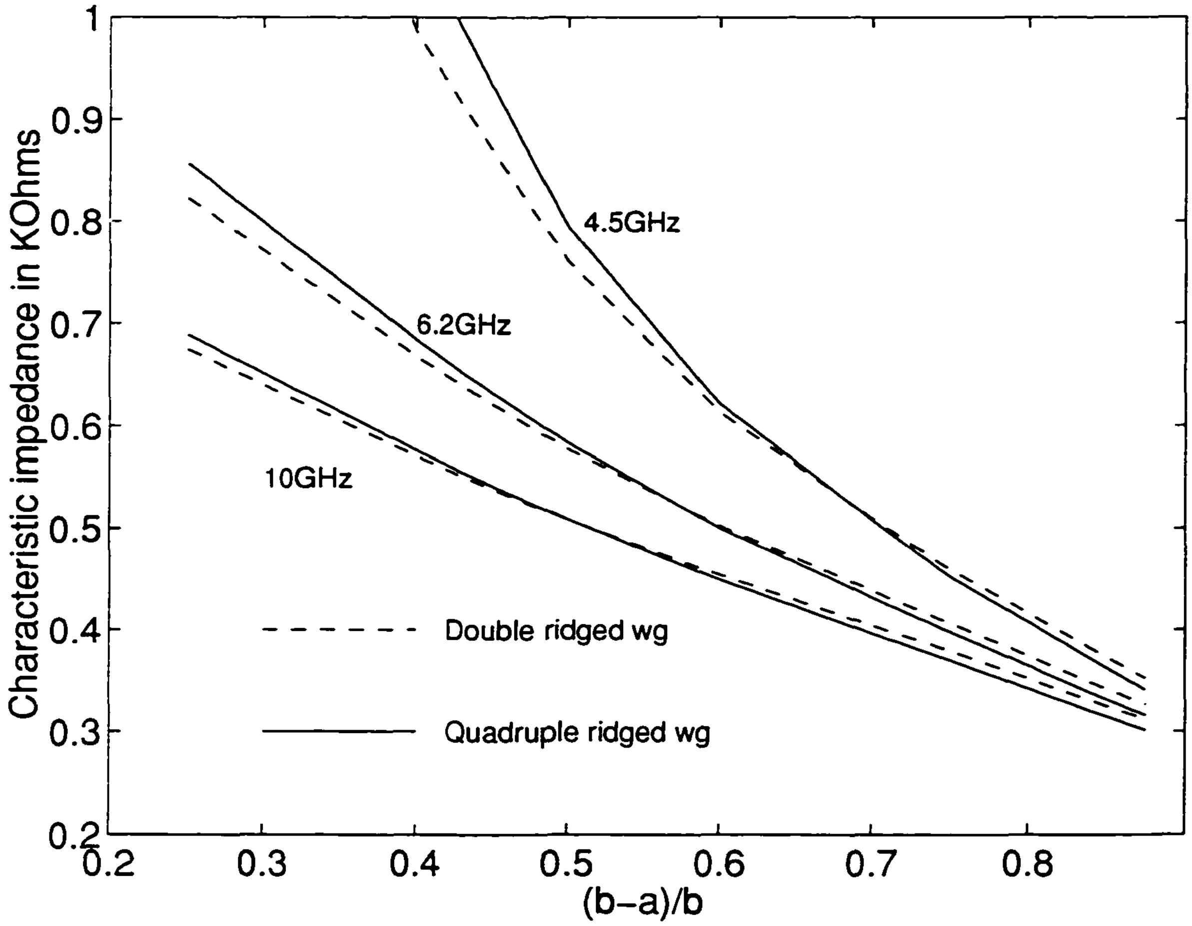

Figure 3.12: Characteristics impedance of quadruple and double ridged circular waveguide versus ridge depth, b=2cm, ridge thickness=10 degree

Chapter 4

Discontinuities in Ridged Circular Waveguides

4.1 Introduction

The eigenvalue analysis of various types of ridged circular waveguides was discussed in the previous chapter. However, this is only the first step in the design of components in ridged circular waveguides. For a rigorous design of components involving ridged circular waveguides it is essential to evaluate the S-parameters of every discontinuity based on the interaction of the fundamental and higher order modes. Once again here, the ridges have been shaped conically. This enables the coupling between the fundamental and higher order modes to be evaluated analytically at least in certain subregions of the discontinuity.

In this chapter, first a discontinuity from a circular waveguide into a double-ridged circular waveguide is analyzed. Subsequently, the generalized scattering matrix technique is utilized to analyze and design components. Based on the characteristic impedance evaluated in the previous chapter, Chebychev transformers in double and quadruple ridged circular waveguides have been designed and optimized. Similarly, an evanescent mode circular waveguide filter has also been designed. A very thin metal sheet of rectangular cross-section has been approximated as a conically shaped one in the numerical analysis. Using this approximation, a filter has been fabricated, measured and compared with the theoretical analysis.

4.2 Circular to double ridged circular waveguide discontinuity

The geometry of the discontinuity is shown in Figure 4.1. The excitation of such a discontinuity is the fundamental mode namely $TE_{1,1}$. From the geometry, it is clear that there can be two lines of symmetry for this excitation. For the orientation of the ridge and excitation shown, the lines of symmetry are magnetic wall along the line joining the ridges and electric wall along the line perpendicular to this.

The solution to the Helmholtz equation in cylindrical coordinates is written for both regions of discontinuity as a sum of incident and reflected waves of unknown amplitudes.

$$\overrightarrow{\psi^{(ih)}}(\rho, \phi, z) = \sqrt{Z^{ih}}\psi^{(ih)}(\rho, \phi)(F^{(ih)}\epsilon^{(-jk_z^{(ih)}z)} + B^{(ih)}\epsilon^{(+jk_z^{(ih)}z)}) \tag{4.1}$$

$$\overrightarrow{\psi^{(ie)}}(\rho, \phi, z) = \sqrt{Y^{ie}}\psi^{(ie)}(\rho, \phi)(F^{(ie)}\epsilon^{(-jk_z^{(ie)}z)} + B^{(ie)}\epsilon^{(+jk_z^{(ie)}z)} \tag{4.2}$$

where, the superscript i refers to region I or II of the discontinuity. The wave impedance Z^{ih} and the wave admittance Y^{ie} for a mode with propagation constant k_z are given as:

$$Z^{ih} = \frac{\omega\mu_o}{k_z^{(ih)}} \tag{4.3}$$

$$Y^{ie} = \frac{\omega\epsilon_o}{k_z^{(ie)}} \tag{4.4}$$

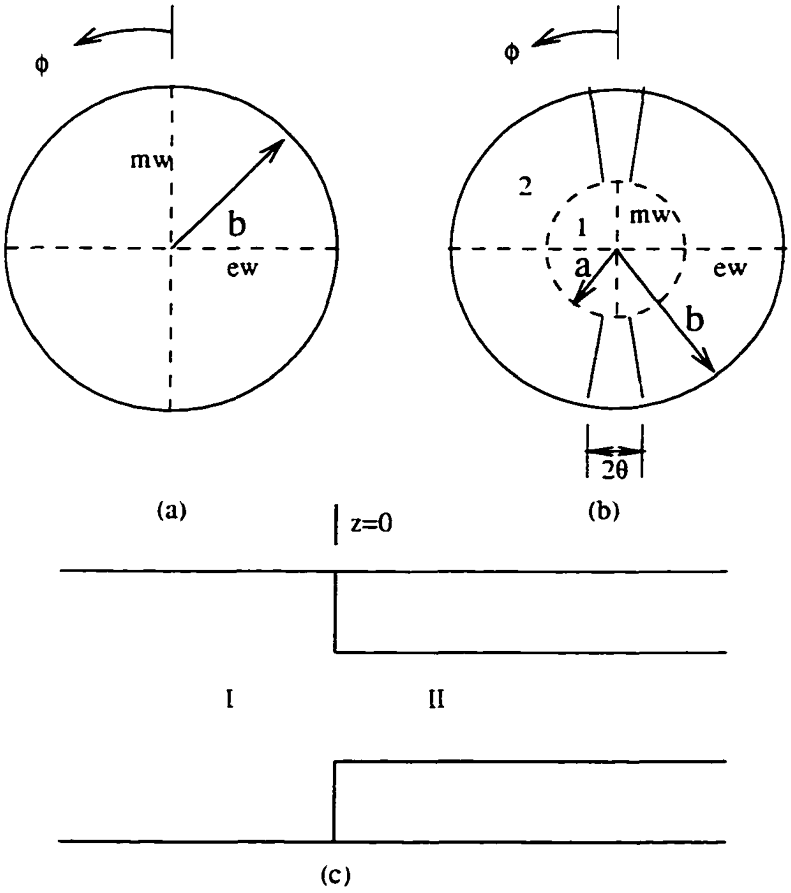

Figure 4.1: Discontinuity regions (a) circular waveguide (region I) (b) double ridged circular waveguide (region II) (c) side-view

The transverse component of electric and magnetic potential functions in the empty circular waveguide(region I) for such a symmetry can be written as follows:

$$\psi^{(Ih)}(\rho,\phi) = \sum_{m=1}^{M^h} \sum_{n=1,3}^{N^h} P^{Ih}_{n,m} J_n(k^{Ih}_{c_{n,m}}\rho) \sin n\phi \tag{4.5}$$

$$\psi^{(Ie)}(\rho,\phi) = \sum_{m=1}^{M^e} \sum_{n=1,3}^{N^e} P^{Ie}_{n,m} J_n(k^{Ie}_{c_{n,m}}\rho) \cos n\phi \tag{4.6}$$

The eigenvalues of the circular waveguide for TM and TE modes can be determined from the zeros of the Bessel functions and their derivatives respectively. The coefficients P represent the power normalization constants and are obtained by setting the magnitude of the power carried in each of the modes to unity. For a circular waveguide of radius b this yields.

$$P^{Ih}_{n,m} = \begin{cases} \sqrt{\frac{\pi}{2}}\sqrt{k^{Ih}_{c_{n,m}}b - n^2}J_n(k^{Ih}_{c_{n,m}}b) & n \neq 0 \\ \sqrt{\pi}\sqrt{k^{Ih}_{c_{0,m}}b}J_n(k^{Ih}_{c_{0,m}}b) & n = 0 \end{cases} \tag{4.7}$$

$$P^{Ie}_{n,m} = \begin{cases} \sqrt{\frac{\pi}{2}}k^{Ie}_{c_{n,m}}bJ'_n(k^{Ie}_{c_{n,m}}b) & n \neq 0 \\ \sqrt{\pi}k^{Ie}_{c_{0,m}}bJ_1(k^{Ie}_{c_{0,m}}b) & n = 0 \end{cases} \tag{4.8}$$

The values of M^h. M^e and N^h. N^e in equations (4.5) and (4.6) depend on the truncation of the number of TE and TM modes used in the evaluation of the generalized scattering matrix.

In the region II of the discontinuity the electric and magnetic potential functions are expressed as the sum of those in subregions 1 and 2. They are as follows:

$$\psi^{(IIh)}(\rho.\phi) = \sum_{r=1}^{R_h}(\psi^{(1h)}(\rho.\phi) + \psi^{(2h)}(\rho.\phi)) \tag{4.9}$$

$$\psi^{(IIe)}(\rho.\phi) = \sum_{r=1}^{R_e}(\psi^{(1e)}(\rho.\phi) + \psi^{(2e)}(\rho.\phi)) \tag{4.10}$$

The magnetic potential functions in the ridged circular waveguide subregions 1 and 2. shown in Figure 4.1 for a ridge thickness of 2θ can be written as follows:

$$\psi^{(1h)}(\rho.\phi) = \sum_{n=1.3}^{N1} A_nJ_n(k^{IIh}_{c_r}\rho)\sin n\phi \tag{4.11}$$

$$\psi^{(2h)}(\rho.\phi) = \sum_{m=0}^{N2} C_m[N'_l(k^{IIh}_{c_r}b)J_l(k^{IIh}_{c_r}\rho) - J'_l(k^{IIh}_{c_r}b)N_l(k^{IIh}_{c_r}\rho)]\cos l(\phi - \theta) \tag{4.12}$$

where $l = \frac{m\pi}{\frac{\pi}{2}-\theta}$. Similarly, the electric potential functions in the subregions 1 and 2 are written as follows:

$$\psi^{(1e)}(\rho,\phi) = \sum_{n=1,3}^{N1} B_n J_n(k_{c_r}^{IIe}\rho)\cos n\phi \tag{4.13}$$

$$\psi^{(2e)}(\rho,\phi) = \sum_{m=1}^{N2} D_m[N_l(k_{c_r}^{IIe}b)J_l(k_{c_r}^{IIe}\rho) - J_l(k_{c_r}^{IIe}b)N_l(k_{c_r}^{IIe}\rho)]\sin l(\phi-\theta) \tag{4.14}$$

where, once again $l = \frac{m\pi}{\frac{\pi}{2}-\theta}$.

It should be noted that each r in $\psi^{(IIh)}$ corresponds to a set of indices n in $\psi^{(1h)}$ and m in $\psi^{(2h)}$ and has a particular value for k_c^{IIh}. It is similar for $\psi^{(IIe)}$. In other words, the modal indices are different in each of the two subregions 1 and 2 as a result of the differing boundary conditions in the two subregions. It should also be noted that the potential functions in subregion 2 has Bessel functions and Neumann functions of non-integer orders.

The value of $k_{c_r}^{IIh}$ and $k_{c_r}^{IIe}$ in the potential functions has been evaluated using the procedure in chapter 3. The coefficients are evaluated as mentioned in the procedure for the determination of the characteristic impedance in Chapter 2. The modal coefficients are normalized so that the magnitude of power in each mode is unity.

From the potential functions described above in the two regions of discontinuity the electric and magnetic fields in each of the regions of Figure 4.1 can be derived, using the equations in Appendix D.

At the interface of the two regions ($z = 0$), the continuity of the tangential components of E and H-field of the incident and reflected waves is applied:

$$\begin{aligned} E_T^I &= E_T^{II} \; r \in [0,a],\ \phi \in [0,2\pi];\ r \in [a,b],\ \phi \in [(\theta,\pi-\theta);(\pi+\theta,2\pi-\theta)] \\ &= 0 \qquad\qquad r \in [a,b],\ \phi \in [-\theta,+\theta],\phi \in [\pi-\theta,\pi+\theta] \qquad (4.15) \\ H_T^I &= H_T^{II} \; r \in [0,a]\ \phi \in [0,2\pi];\ \text{and } r \in [a,b],\ \phi \in [(\theta,\pi-\theta),(\pi+\theta,2\pi-\theta)] \end{aligned}$$

Using the orthogonality property of the modes, the above equation results in four sets of equations relating the unknown wave amplitudes of the incident(F) and reflected(B) waves. For instance, the continuity of the tangential components of the E-field results in the two sets of equations given below:

$$\begin{aligned} (F^{Ih} + B^{Ih}) &= [V_{hh}](F^{IIh} + B^{IIh}) & (4.16) \\ (F^{Ie} + B^{Ie}) &= [V_{ee}](F^{IIe} + B^{IIe}) + [V_{eh}](F^{IIh} + B^{IIh}) & (4.17) \end{aligned}$$

where the $[V]$ matrices give the coupling between the fundamental and higher order TE and TM modes. The coupling matrices are given below.

$$V_{hh}(x, y) = (\sum_{n=1,3}^{N1} Term_1 + \sum_{m=0}^{N2} Term_2)\sqrt{\frac{k_z^{Ih}(x)}{k_z^{IIh}(y)}} \tag{4.18}$$

where the $Term_1$ and $Term_2$ are given below. The x refers to the mode that is excited in cross section I while y refers to that in II. Also, k_z represent the propagation constants of the corresponding TE and TM modes in regions I and II. The modal coefficients of the subregions 1 and 2 A_n, B_n, C_m and D_m have been absorbed into the respective power normalization constants in the following equations of the coupling integrals.

$$\begin{aligned} Term_1 &= P_{s,p}^{Ih} P_{n,r}^{IIh} \pi \\ & \cdot \int_0^a [\frac{ns}{\rho^2} J_s(k_{c_{s,p}}^{Ih}\rho) J_n(k_{c_r}^{IIh}\rho) + J_s'(k_{c_{s,p}}^{Ih}\rho) J_n'(k_{c_r}^{IIh}\rho)]\rho d\rho \quad \text{if n=s} \\ &= 0 \quad \text{if n} \neq \text{s} \qquad (4.19) \end{aligned}$$

$$Term_2 = P_{s,p}^{Ih} P_{m,r}^{IIh} \int_a^b -\frac{ls}{\rho^2} J_s(k_{c_{s,p}}^{Ih}\rho)[J_l(k_{c_r}^{IIh}\rho) N_l'(k_{c_r}^{IIh}b) -$$

$$J_l'(k_{c_r}^{IIh}b)N_l(k_{c_r}^{IIh}\rho)]\rho d\rho\cdot 4\int_\theta^{\pi/2}\cos s\phi\sin l(\phi-\theta)d\phi+$$

$$P_{s,p}^{(Ih)}P_{m,r}^{(IIh)}\int_a^b J_s'(k_{c_{s,p}}^{Ih}\rho)[J_l'(k_{c_r}^{IIh}\rho)N_l'(k_{c_r}^{IIh}b)-$$

$$J_l'(k_{c_r}^{IIh}b)N_l'(k_{c_r}^{IIh}\rho)]\rho d\rho\cdot 4\int_\theta^{\pi/2}\sin s\phi\cos l(\phi-\theta)d\phi \tag{4.20}$$

where $l=\frac{m\pi}{\phi_o}$: $\phi_o=(\pi/2-\theta)$ double ridged circular waveguide as region II.

$$V_{ee}(x,y)=(\sum_{n=1,3}^{N1}Term_3+\sum_{m=1}^{N2}Term_4)\sqrt{\frac{k_z^{IIe}(x)}{k_z^{Ie}(y)}} \tag{4.21}$$

$$\begin{aligned}
Term_3 &= P_{s,p}^{Ie}P_{n,r}^{IIe}\pi\\
&\quad\cdot\int_0^a[\frac{ns}{\rho^2}J_s(k_{c_{s,p}}^{Ie}\rho)J_n(k_{c_r}^{IIe}\rho)+J_s'(k_{c_{s,p}}^{Ie}\rho)J_n'(k_{c_r}^{IIe}\rho)]\rho d\rho \quad \text{if n=s}\\
&= 0 \quad \text{if n} \neq \text{s}
\end{aligned} \tag{4.22}$$

$$\begin{aligned}
Term_4 &= P_{s,p}^{Ie}P_{m,r}^{IIe}\int_a^b-\frac{ls}{\rho^2}J_s(k_{c_{s,p}}^{Ie}\rho)[J_l(k_{c_r}^{IIe}\rho)N_l(k_{c_r}^{IIe}b)-\\
&\quad J_l(k_{c_r}^{IIe}b)N_l(k_{c_r}^{IIe}\rho)]\rho d\rho\cdot 4\int_\theta^{\pi/2}\sin s\phi\cos l(\phi-\theta)d\phi+\\
&\quad P_{s,p}^{(Ie)}P_{m,r}^{(IIe)}\int_a^b J_s'(k_{c_{s,p}}^{Ie}\rho)[J_l'(k_{c_r}^{IIe}\rho)N_l(k_{c_r}^{IIe}b)-\\
&\quad J_l(k_{c_r}^{IIe}b)N_l'(k_{c_r}^{IIe}\rho)]\rho d\rho\cdot 4\int_\theta^{\pi/2}\cos s\phi\sin l(\phi-\theta)d\phi
\end{aligned} \tag{4.23}$$

where $l=\frac{m\pi}{\phi_o}$: $\phi_o=(\pi/2-\theta)$ double ridged circular waveguide as region II.

$$V_{eh}(x,y)=(\sum_{n=1,3}^{N1}Term_5+\sum_{m=0}^{N2}Term_6)\frac{k_o}{\sqrt{k_z^{IIh}(y)k_z^{Ie}(x)}} \tag{4.24}$$

$$
\begin{aligned}
Term_5 &= P^{Ie}_{s,p} P^{IIh}_{n,r} \pi \\
&\quad \cdot \int_0^a [n J'_s(k^{Ie}_{c_{s,p}} \rho) J_n(k^{IIh}_{c_r} \rho) + s J_s(k^{Ie}_{c_r} \rho) J'_n(k^{IIh}_{c_{s,p}} \rho)] d\rho \quad \text{if n=s} \\
&= 0 \quad \text{if n} \neq \text{s} \qquad (4.25)
\end{aligned}
$$

$$
\begin{aligned}
Term_6 &= P^{Ie}_{s,p} P^{IIh}_{m,r} \int_a^b -l J'_s(k^{Ie}_{c_{s,p}} \rho)[J_l(k^{IIh}_{c_r} \rho) N'_l(k^{IIh}_{c_r} b) - \\
&\quad J'_l(k^{IIh}_{c_r} b) N_l(k^{IIh}_{c_r} \rho)] d\rho \cdot 4 \int_\theta^{\pi/2} \cos s\phi \sin l(\phi - \theta) d\phi + \\
&\quad P^{(Ie)}_{s,p} P^{(IIh)}_{m,r} \int_a^b s J_s(k^{Ie}_{c_{s,p}} \rho)[J'_l(k^{IIh}_{c_r} \rho) N'_l(k^{IIh}_{c_r} b) - \\
&\quad J'_l(k^{IIh}_{c_r} b) N'_l(k^{IIh}_{c_r} \rho)] d\rho \cdot 4 \int_\theta^{\pi/2} \sin s\phi \cos l(\phi - \theta) d\phi \qquad (4.26)
\end{aligned}
$$

where $l = \frac{m\pi}{2\phi_o}$: $\phi_o = (\pi/2 - \theta)$ double ridged circular waveguide as region II.

While some of the integrals can be evaluated analytically, some others are evaluated numerically. However, all the coupling integrals are frequency independent and hence the numerical integration is not repeatedly evaluated at every frequency point. Hence, this procedure is rigorous and yet computationally efficient.

Applying the continuity of the tangential components of the H-fields results in coupling matrices that are the transposed of the coupling matrices in equations (4.16) and (4.17). Equations (4.16) and (4.17) together with the matrix equations resulting from the continuity of the H-fields can be rearranged suitably using Appendix B and inverted to yield the generalized scattering matrix of the discontinuity between the empty circular waveguide and a ridged circular waveguide. Any subsequent discontinuity can be cascaded using the generalized scattering matrix technique described in Appendix C.

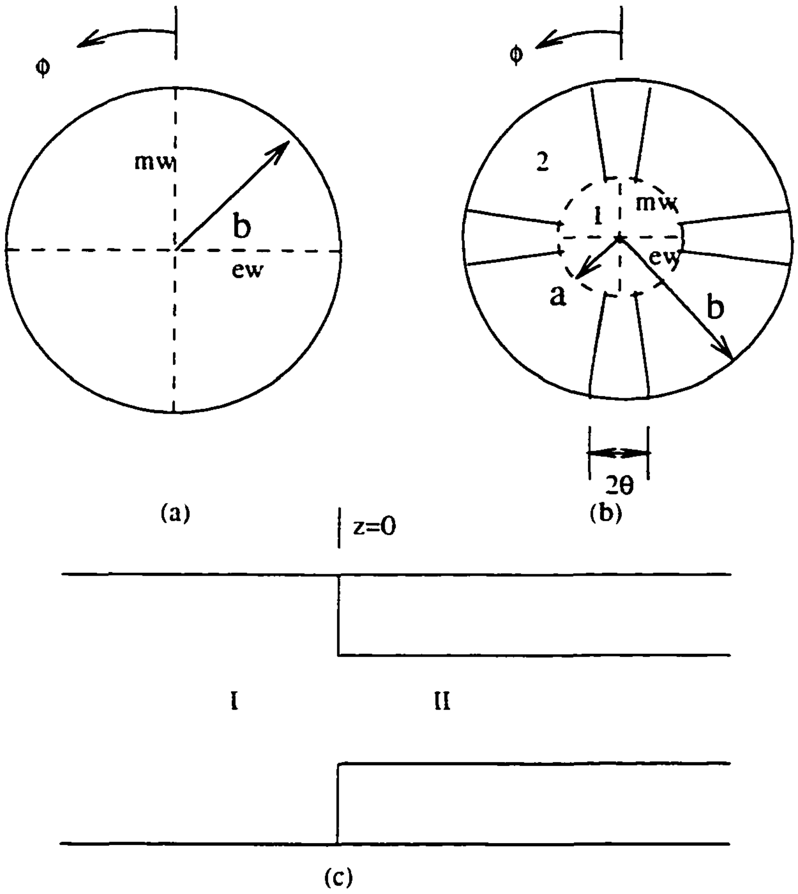

Figure 4.2: Discontinuity regions (a) circular waveguide (region *I*) (b) quadruple ridged circular waveguide (region *II*) (c) side-view

4.3 Circular to quadruple ridged circular waveguide discontinuity

The regions of the discontinuity from a circular to a quadruple ridged waveguide are shown in Figure 4.2. Since the extra pair of ridges as compared to the double ridged circular waveguide appear along the electric wall symmetry. the discontinuity from circular to quadruple ridged circular waveguide discontinuity is almost the same as the circular to double ridged circular waveguide discontinuity.

But there are minor changes in the potential functions and hence in the coupling integrals too. For the quadruple ridged cross-section, l in $\psi^{(2h)}$ and $\psi^{(2e)}$ of equations (4.12) (4.14) is given as $l = \frac{m\pi}{\frac{\pi}{2}-2\theta}$ for a ridge thickness of 2θ. This is also the value of l in the equations of the coupling integrals, namely (4.20), (4.23) and (4.26). The coupling integrals also change with regard to the limits of the ϕ dependent integral in the equations for V_{ee}, V_{eh} and V_{hh}. The limits θ to $\pi/2-\theta$ is used in place of θ to $\pi/2$ for this discontinuity in equations (4.20), (4.23) and (4.26).

4.4 Convergence analysis

A convergence analysis for a discontinuity from empty circular waveguide to double ridged circular waveguide shows that less than 40 TE and TM modes are required. This is shown in the Figure 4.3.

Since the highest order modes of the ridged circular waveguide included in the discontinuity analysis have cutoff frequencies which are very close to the corresponding one in the empty circular waveguide, the number of modes used in the discontinuity analysis is the same in both regions of the discontinuity.

A discontinuity between an empty circular waveguide and ridged circular waveguide has not been analyzed in literature before. So a finitely long double ridged circular wave guide placed between an input and output empty circular waveguide was first evaluated using the rigorous procedure described above. The discontinuity was fabricated with a very thin ridge (thickness= 125μm in a circular waveguide of diameter 8mm) that has rectangular cross-section. In the computation, this ridge was approximated as a conically shaped one with a constant angular thickness of $\theta = 1$ degree. This value of θ is the angle subtended on the edge of circular waveguide to meet the rectangular thickness of the ridge and has been rounded to the closest integer. The dimensions of the circular waveguide and the ridge depth are given in Figure 4.4. A comparison was made with measurements and good agreement was

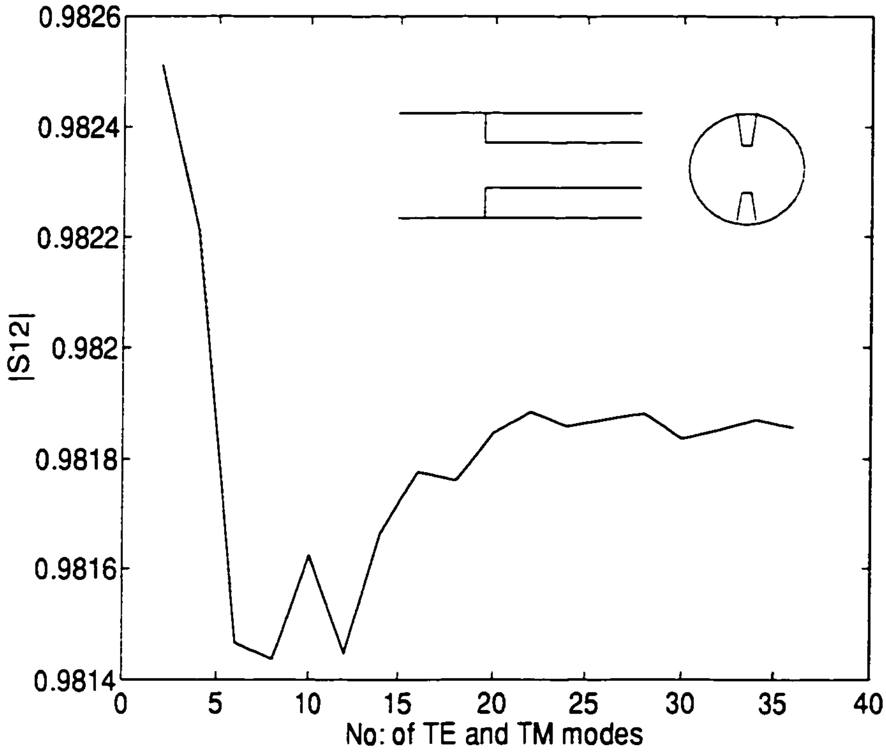

Figure 4.3: Magnitude of S_{12} of a discontinuity from a circular waveguide to a double ridged circular waveguide. b=2mm. a=1.5mm. f=55GHz. θ = 5degree

found as shown in Figure 4.4. The small disagreement may be attributed to the approximation of the shape of the ridges.

4.5 Components in ridged circular waveguides

4.5.1 Transformer Design

lowered characteristic impedance. The ridged circular waveguide has a lower characteristic impedance compared to that of an empty circular waveguide. This enables the excitation of the fundamental polarization in an empty circular waveguide from a coaxially fed double ridged circular waveguide. This same feature allows excita-

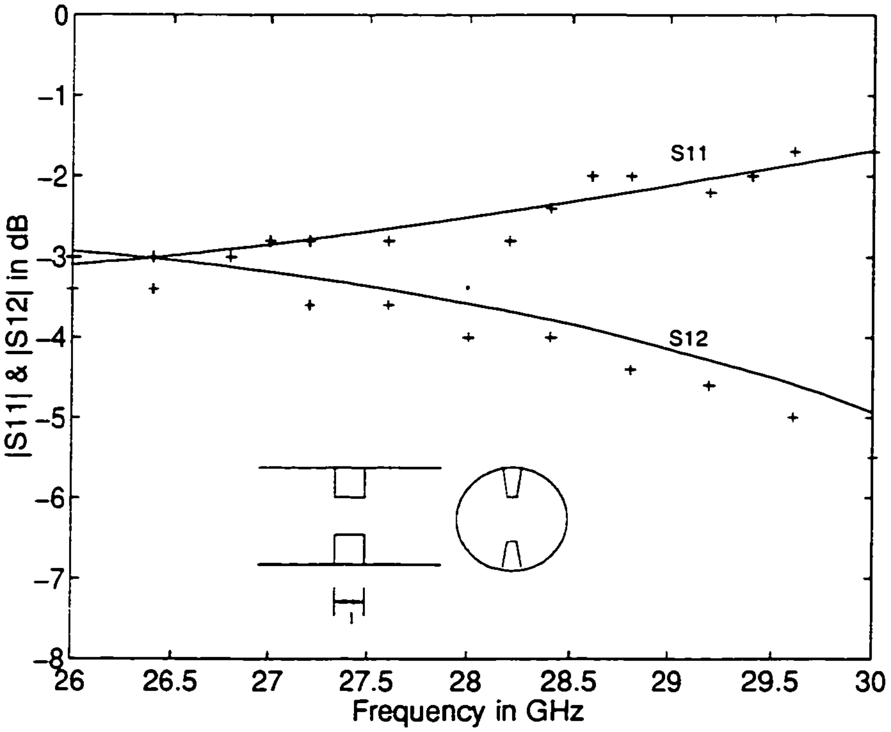

Figure 4.4: S-parameters in dB of a discontinuity from circular waveguide to a double ridged circular waveguide of finite length, b=4mm, a=2mm, ridge thickness =125μm ($\theta = 1$ degree), l=1.1mm, + measured, - calculated

tion of fundamental orthogonal polarizations to a circular waveguide from a coaxially fed quadruple ridged circular waveguide. Hence a rigorous design of transformers from empty circular waveguide into a ridged circular waveguide is of great practical importance.

Based on the characteristic impedance evaluated in the previous chapter, a Chebyshev transformer shown in Figure 4.5 is designed for a return loss specification. The ridge depths in various sections of the Chebychev transformer are determined from the characteristic impedance of the respective section. The lengths of the sections initially assumed are quarter wavelength long at the chosen center frequency. In order to evaluate the response of the transformer including the effect of the higher

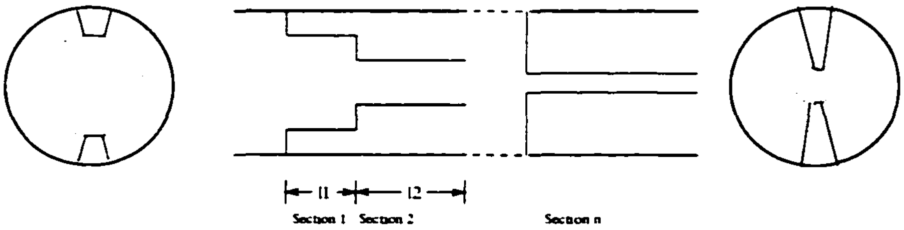

Figure 4.5: A Chebychev Transformer in double ridged circular waveguide

order modes, first the generalized scattering matrix of a discontinuity from an empty circular waveguide to each ridged circular waveguide section is evaluated. Cascading the generalized scattering matrices of the individual sections (see Appendix C) leads to the overall generalized S-matrix of the the transformer. While cascading S-matrix of one section of the transformer to the subsequent section, the lengths of the intermediate sections of circular waveguide are allowed to approach zero.

The length of the ridged sections were altered using an optimization routine to provide an improved performance of the transformer. The optimization routine was based on modified Fletchers algorithm for minimization of an objective function as described in [64]. The objective function is the error function of the desired response to the actual response of the transformer. The response during the optimization is evaluated using about 20 TE and TM modes. At the end of the optimization, the final response is evaluated using 40 TE and TM modes.

Using this procedure a double ridged (Figure 4.5) and quadruple ridged circular waveguide transformers have been designed and optimized. Their return loss characteristics are shown in Figures 4.6 and 4.7.

It should be noted that in these transformers, the limitation on the bandwidth is due to the higher order modes. The capacitive action of the ridge not only lowers the cutoff frequency of the fundamental mode but also lowers that of the first few higher order modes greatly. Since the cutoff frequency of $TE_{3,1}$ mode is also lowered

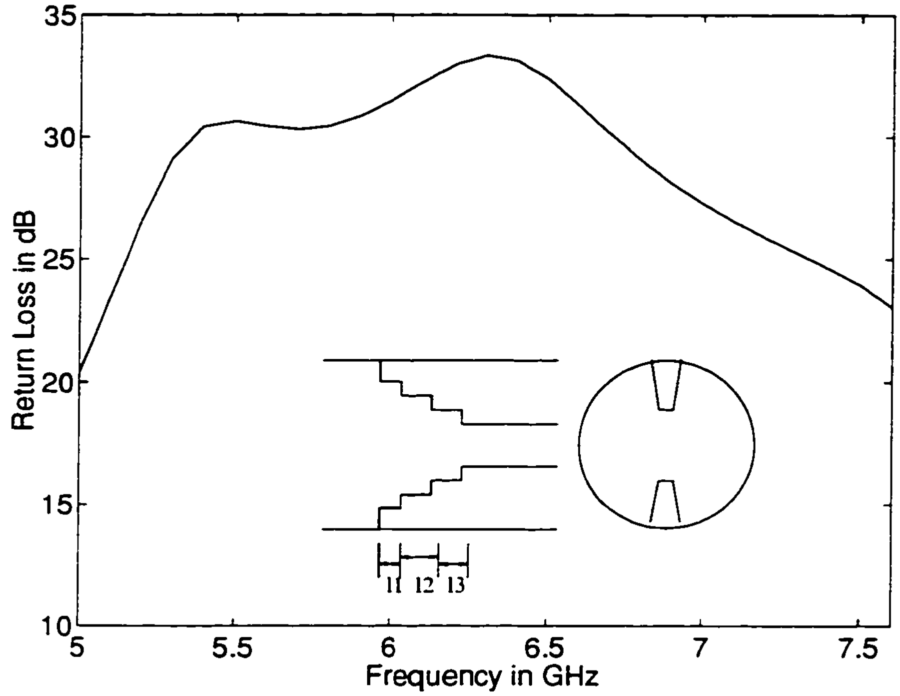

Figure 4.6: Response of an optimum 3-section double ridged circular waveguide transformer. dimensions in cm. section 1: b=2. a=1.7. l1=1.633. section 2: b=2. a=1.13. l2=1.351. section 3: b=2. a=0.7. l3=1.191. section 4: b=2 a=0.5

considerably. and this mode is the first higher order mode that gets excited at the discontinuities between each sections. the return loss of the transformer goes down beyond the propagation of this mode.

The bandwidth of such a type of transformer can be improved to some extent by reducing the outer circular diameter of the ridged circular waveguide in the subsequent sections of the transformer. The structure of such a transformer is shown in Figure 4.8. The return loss characteristics of such an optimized quadruple ridged circular waveguide transformer is shown in Figure 4.9.

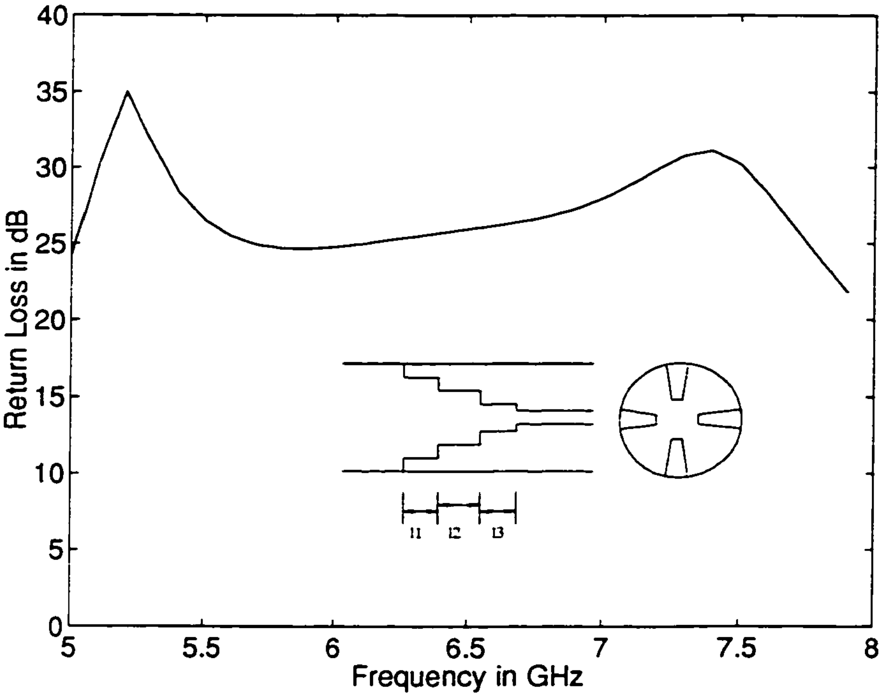

Figure 4.7: Response of an optimum 3-section quadruple ridged circular waveguide transformer. dimensions in cm. section 1: b=2. a=1.62. l1=1.519. section 2: b=2. a=1.09. l2=1.404. section 3: b=2. a=0.68. l3=1.363. section 4: b=2 a=0.5

4.5.2 Bandpass Filter

The significant lowering of the fundamental mode cutoff frequency in ridged waveguides can be used to fabricate filters in below cutoff sections of a waveguide. Such filters have many attractive features like wide stopband characteristic. small component size and high skirt selectivity. Hence. they are well suited for applications in antenna feed system. Because of these features they are also preferred over metal insert filters and other conventional filters which are bigger in size and are heavier. These two features are important for satellite applications.

The resonators inside these filters were initially constructed using round posts inside a below cutoff waveguide [65]. Rigorous design of such evanescent mode bandpass

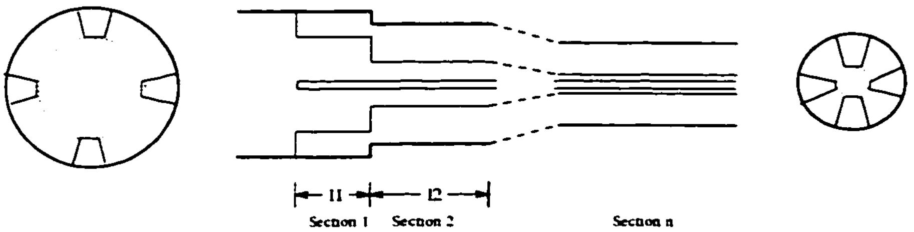

Figure 4.8: A quadruple ridged circular waveguide transformer with tapered outer circular waveguide housing

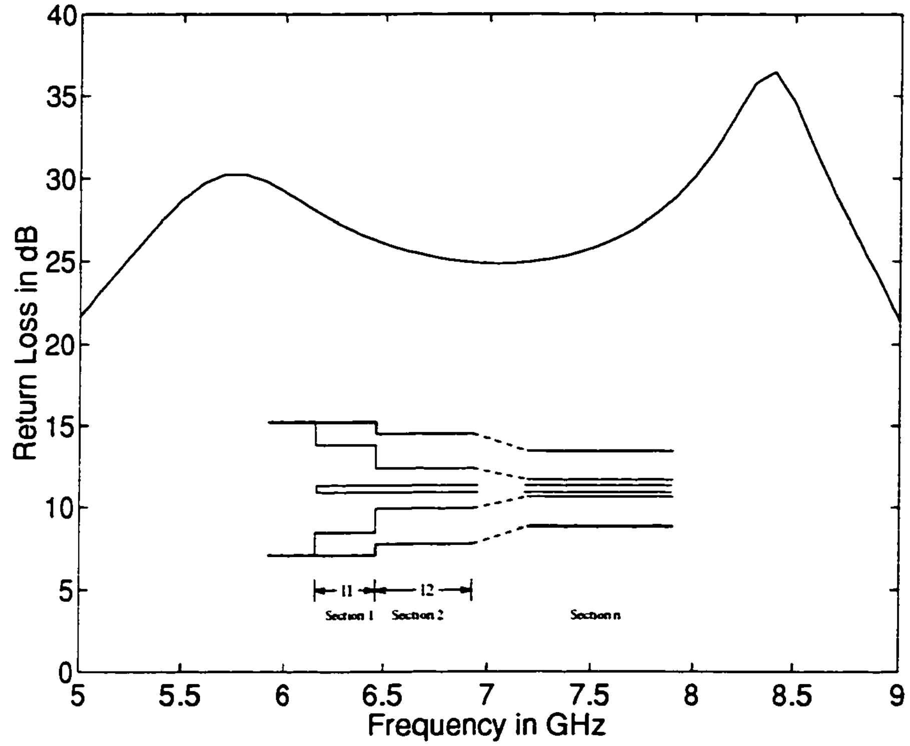

Figure 4.9: Response of an optimum 3-section quadruple ridged circular waveguide transformer, dimensions in cm, section 1: b=2, a=1.7, l1=1.162, section 2: b=1.95, a=1.45, l2=1.474, section 3: b=1.9, a=1.25, l3=1.59, section 4: b=1.85 a=1.2

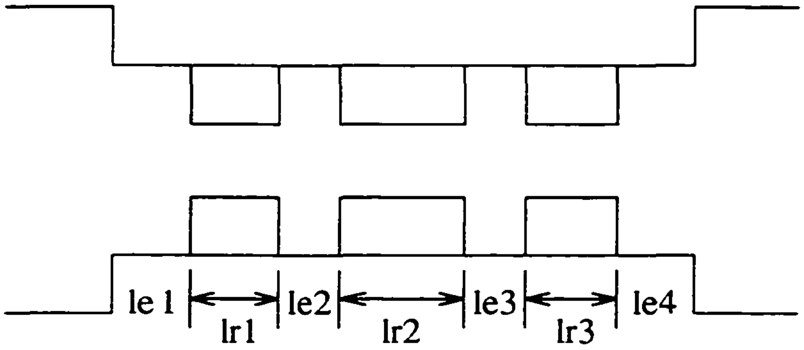

Figure 4.10: Three section evanescent mode circular waveguide filter

filters using ridged rectangular waveguides were presented in [66,67]. The advantage of this type of filter over metal insert type filter was also shown in these references. In order to further improve upon the characteristics of evanescent mode filters, the ridges were replaced by T-septa in [68].

Although rectangular waveguides have been traditionally used to build evanescent filters, the circular waveguide filters are also of practical importance. Moreover, the circular waveguide has lower attenuation for a given cutoff wavelength over a rectangular waveguide. Keeping this in mind, a metal insert circular waveguide was designed in [43], analogous to the metal insert in rectangular waveguides. For the rigorous design, the metal insert was modeled as a bow-tie shaped discontinuity. Such an approximation did not however affect the performance of the filter. Following this approach, an evanescent mode circular waveguide filter shown in Figure 4.10 has been rigorously designed.

An evanescent mode filter in circular waveguide involves rigorous characterization of a symmetrical discontinuity between two circular waveguides and also the discontinuity from an empty circular waveguide to ridged circular waveguide as shown in Figure 4.11. The mode matching technique is once again used to characterize a step discontinuity between two circular waveguides.

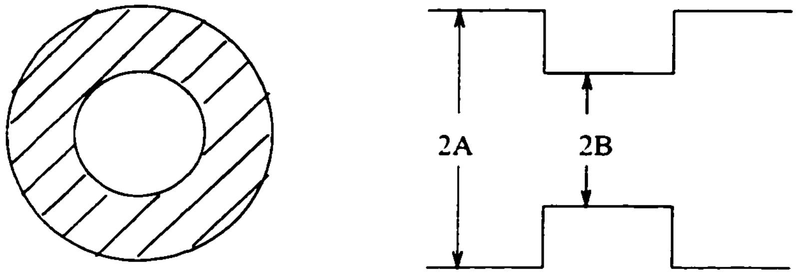

Figure 4.11: Circular waveguide symmetric step discontinuity

If the $TE_{1,1}$ mode is the fundamental mode of excitation, then for this type of discontinuity, the higher order modes that get excited are only $TE_{1,m}$ and $TM_{1,n}$ where $m = n = 1, 2, \cdots$.

The potential functions in region I of this discontinuity can be written as follows:

$$\psi^{(Ih)}(\rho, \phi) = \sum_{m=1}^{M^h} P^{Ih}_{1,m} J_1(k^{Ih}_{c_{1,m}} \rho) \sin \phi \tag{4.27}$$

$$\psi^{(Ie)}(\rho, \phi) = \sum_{m=1}^{M^e} P^{Ie}_{1,m} J_1(k^{Ie}_{c_{1,m}} \rho) \cos \phi \tag{4.28}$$

The potential functions in region II can be written in a similar form. The tangential components of the electric field is matched at the discontinuity. This results in coupling matrices as explained in section 3.2. Along with the transpose of the coupling matrices arising from the matching of the tangential magnetic fields, the generalized scattering matrix of a step discontinuity in circular waveguide is obtained. The S-parameters so obtained for an iris of finite thickness has been compared with available measurements in [69] and are tabulated in Table 4.1. The convergence of the S-parameters for the dimensions in the table occurs with 40 TE and TM modes in the input waveguide and 20 TE and TM modes in the iris.

In the evanescent mode filter where the subsequent discontinuities are evanescent sections of circular waveguide to double ridged circular waveguide, there can be higher

Thickness	Reflection Coefficient s_{11}			
(inch)	Calculated		Measured [69]	
	Magnitude	Phase (o)	Magnitude	Phase (o)
0.005	0.837	150.5	0.855	150.5
0.008	0.881	151.1	0.866	151.7
0.050	0.938	156.5	0.927	155.3
0.100	0.968	159.3	0.956	158.1
0.200	0.990	161.6	0.981	160.6
0.500	0.999	162.6	0.993	161.1
1.000	1.000	162.6	0.995	161.5
	Transmission Coefficient s_{12}			
0.005	0.488	60.5	0.465	56.8
0.008	0.474	61.1	0.451	59.3
0.050	0.345	66.4	0.330	62.6
0.100	0.250	69.3	0.240	65.1
0.200	0.138	71.6	0.134	67.1
0.500	0.025	72.6	0.026	69.0
1.000	0.002	72.6	0.002	70.1

Table 4.1: Calculated and measured S parameters (radius of input/output section=A=0.50175 in. radius of the iris=B=0.25 in; f=9.0 GHz)

order modes other than $TE_{1,m}$ and $TM_{1,m}$ excited. These modes have a magnetic and electric wall along the lines of symmetry, as shown in Figure 4.1. Since the evanescent sections of waveguide in the filter are close to both the input/output sections and the ridged resonator sections, these higher order modes can affect the response of the filter when the S-matrices of all discontinuities are cascaded. Hence the generalized scattering matrix of each step discontinuity between the input circular waveguide and the evanescent section is calculated including these higher order modes. The electric and magnetic potential functions of region I are now written as in equations (4.5) and (4.6). A similar set of potential functions can be written for region II. Matching of the field components and subsequent inversion leads to the generalized scattering matrix. However, the S-parameters of the $TE_{1,m}$ modes do not get affected by these higher order modes when the discontinuity is evaluated individually. The coupling between the included modes and the $TE_{1,m}$ and $TM_{1,n}$ are all zero.

By cascading the generalized scattering matrix of the stepped circular waveguide discontinuity in the filter with the subsequent empty circular waveguide to ridged circular waveguide discontinuities using the equations in Appendix C, the evanescent mode filters response is obtained.

A single resonator evanescent mode filter is first analyzed using the approach discussed above. Figure 4.12 shows the response of a single resonator filter.

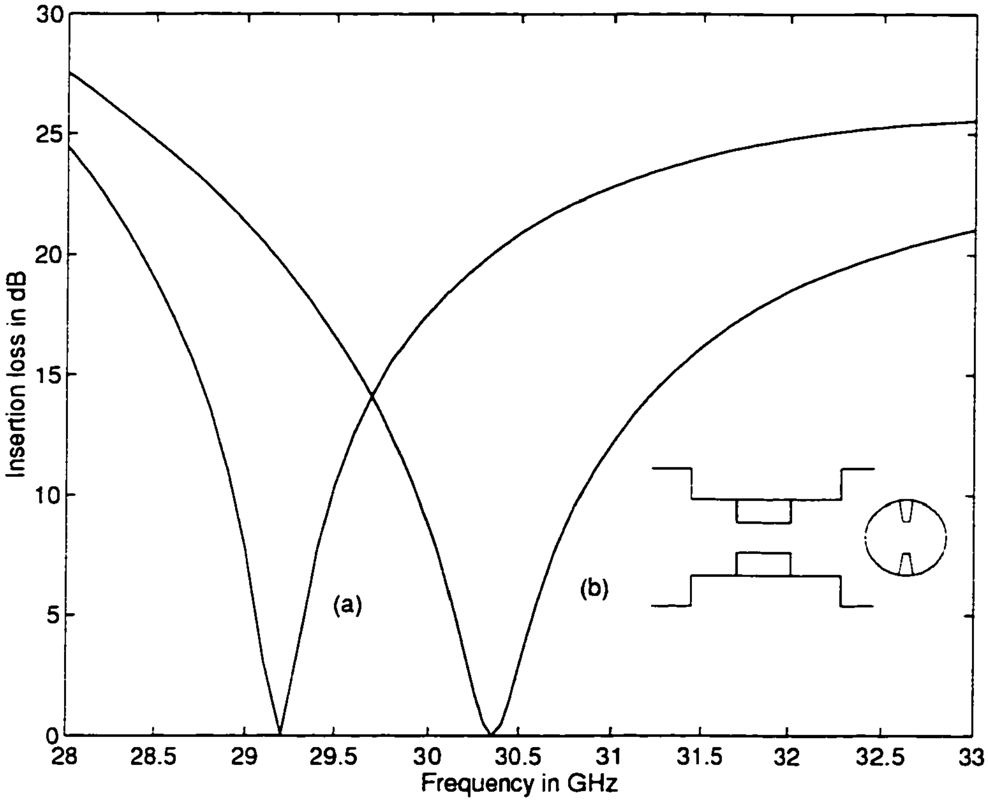

Figure 4.12: Characteristic of a single resonator evanescent mode filter. Radius of input and output waveguide=4mm, radius of evanescent waveguide=2mm, depth of ridge=1.6mm, thickness of ridge θ = 5deg, length of evanescent sections=2mm, (a):length of resonator=3mm (b):length of resonator=2mm

A three resonator evanescent mode filter was first designed. It was optimized using the modified Fletcher algorithm as described in [64]. For this purpose, a suitable objective function was chosen in order to optimize the lengths of resonator and evanescent sections of the filter. It should be noted that the ridge penetration was kept constant in all the resonator sections and not used as a parameter for optimization due to the following reason. If the ridge penetration was altered, the eigenvalues have to be evaluated for every iteration of the optimization. The eigenvalue analysis is however time consuming due to the search at fine steps of frequency points for the minimum of the smallest singular value. The number of TE and TM modes used during the optimization were 30. In the final analysis of the filter 40 modes were included. The response of this filter is shown in Figure 4.13.

Based on the above design the filter was fabricated and measured. The .003 inch uniformly thick brass metal used in the practical realization was approximated as $\theta = 1$deg. A first comparison between measured and calculated response showed a significant offset. However, after remeasuring the actual physical dimensions of the waveguide and the metal insert as well as adjusting the angular thickness of the ridges from $\theta = 1$deg to $\theta = 5.5$deg, so that the tip of the conically shaped ridges show the same thickness as that of the rectangular ridges used in the physical realization of the filter, a relatively good agreement between theory and practise was found. This is illustrated in Figure 4.14. It should be noted, however, that due to the different effective widths of the insert metallization, the ridge length as well as the distance between them is not optimized any longer. Therefore, the electrical performance of the filter has deteriorated considerably. The high insertion loss of 3dB in the passband of the filter is mainly due to the impedance mismatch at the input to the filter and some due to conduction loss in the material. The wideband response of the filter is shown in Figure 4.15.

A five resonator evanescent mode filter has been designed, optimized and fabricated in aluminium circular waveguide. The .003 inch uniformly thick copper sheet

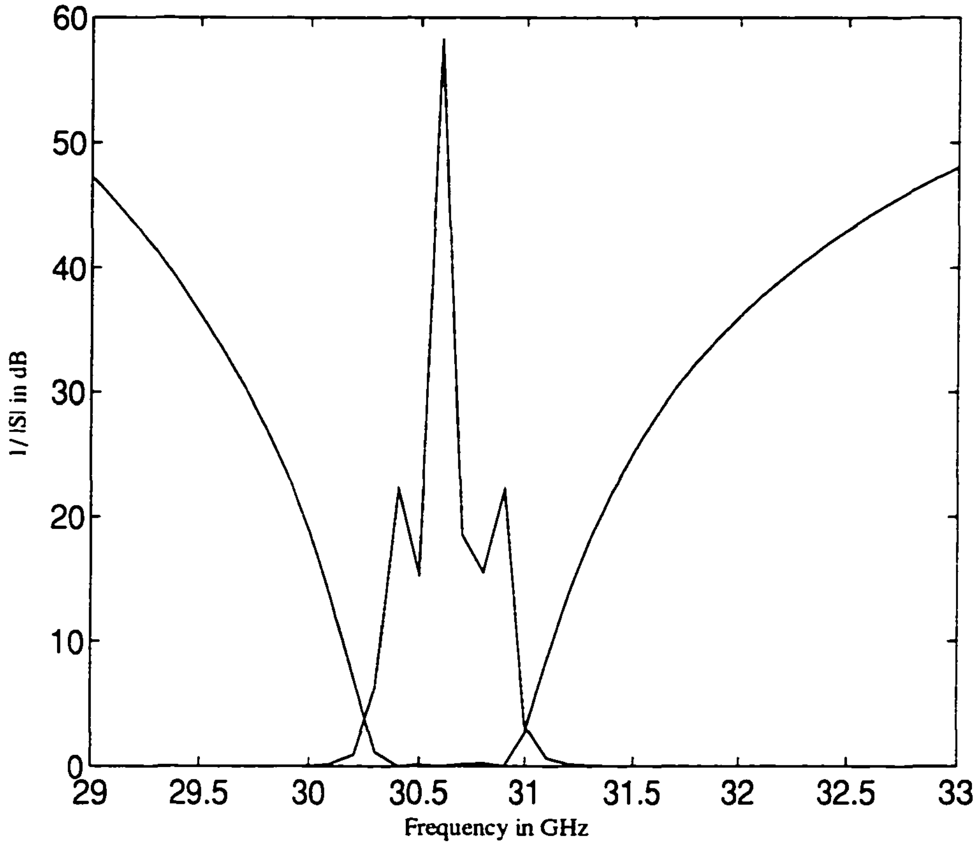

Figure 4.13: Computed response of a 3-resonator evanescent mode circular waveguide filter, dimensions in mm, radius of input/output section=4, radius of evanescent section=b=2, a=0.4, θ = 1deg, le1=le4=1.166, lr1=lr3=1.595, le2=le3=4.396, lr2=1.78

used in the practical realization was approximated as θ = 5.5deg. The passband response of the calculated and realized filter is shown in Figure 4.16. Good agreement with measurements was found. The high insertion loss of 2.5dB of the filter was still observed. A similar effect was observed at much lower frequencies of 8.8 GHz in [68] evanescent mode filter designed using T-septa as resonator sections. The wideband response of the filter (Figure 4.17) behaves similar to an evanescent mode ridge waveguide filter in a rectangular waveguide [67].

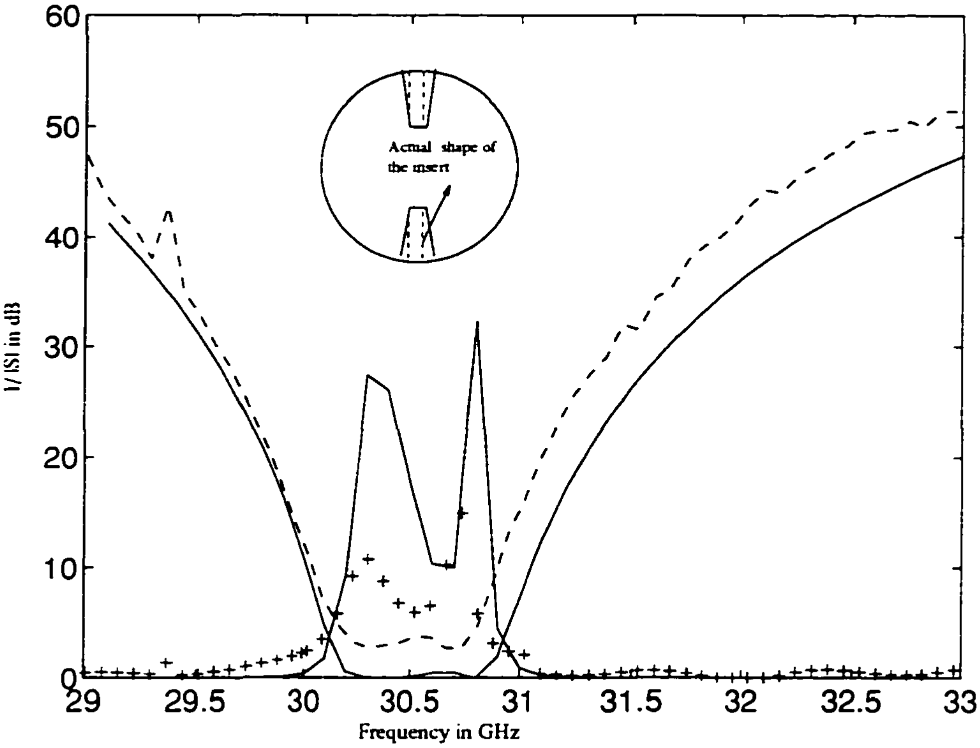

Figure 4.14: Passband response of a 3-resonator evanescent mode circular waveguide filter. dimensions in mm. radius of input/output section=4. radius of evanescent section=b=1.97. a=0.4. θ = 5.5deg. le1=le4=1.2. lr1=lr3=1.58. le2=le3=4.4. lr2=1.78. dashed lines('- -')-measured insertion loss. '+' measured return loss. solid lines-computed response

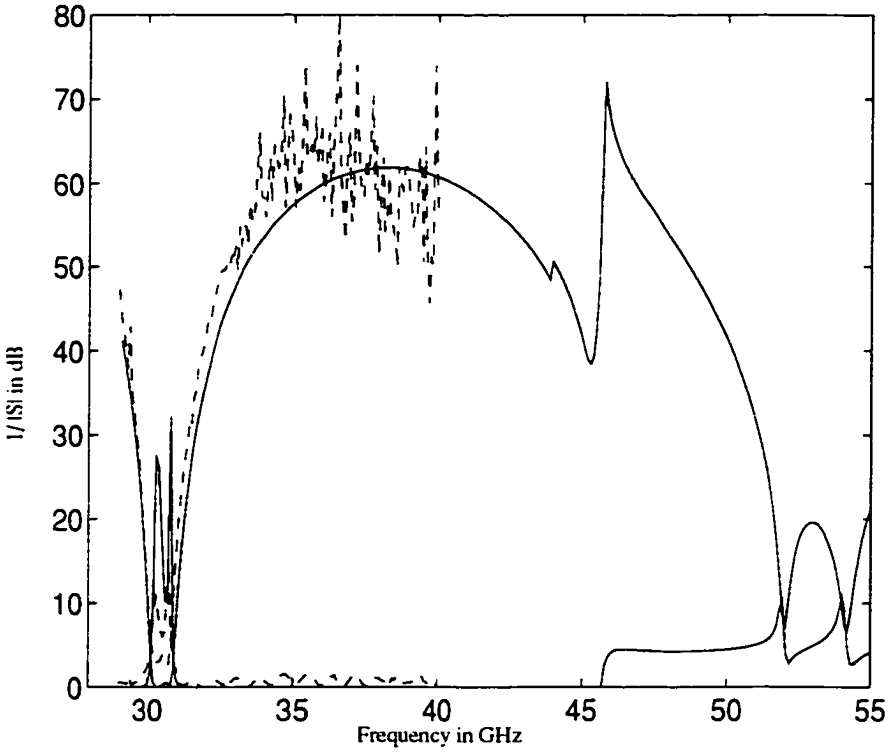

Figure 4.15: Wideband response of the 3-resonator evanescent mode circular waveguide filter in Figure 4.14. dashed lines('- -')-measured response. solid lines-computed response

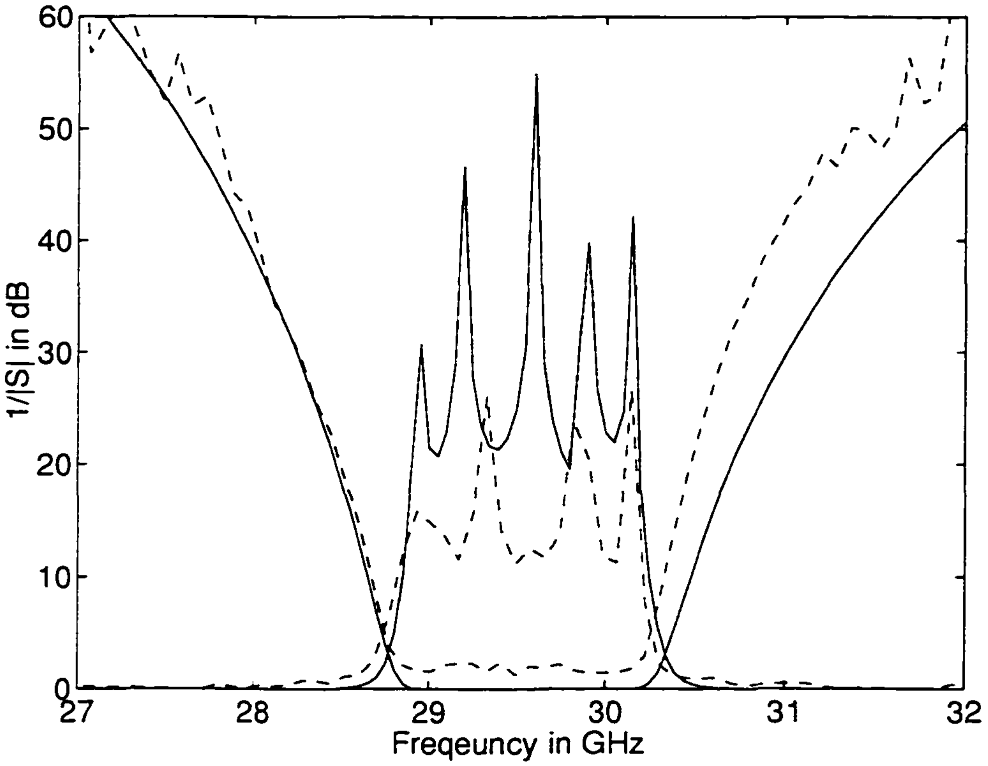

Figure 4.16: Passband response of an optimum 5-resonator evanescent mode circular waveguide filter. dimensions in mm. radius of input/output section=4. radius of evanescent section=b=2. a=0.4. θ = 5.5deg. le1=.36. lr1=1.07. le2=3.09. lr2=1.74. le3=3.36. lr3=1.74. solid lines-computed response. dashed lines ('- -')-measured response

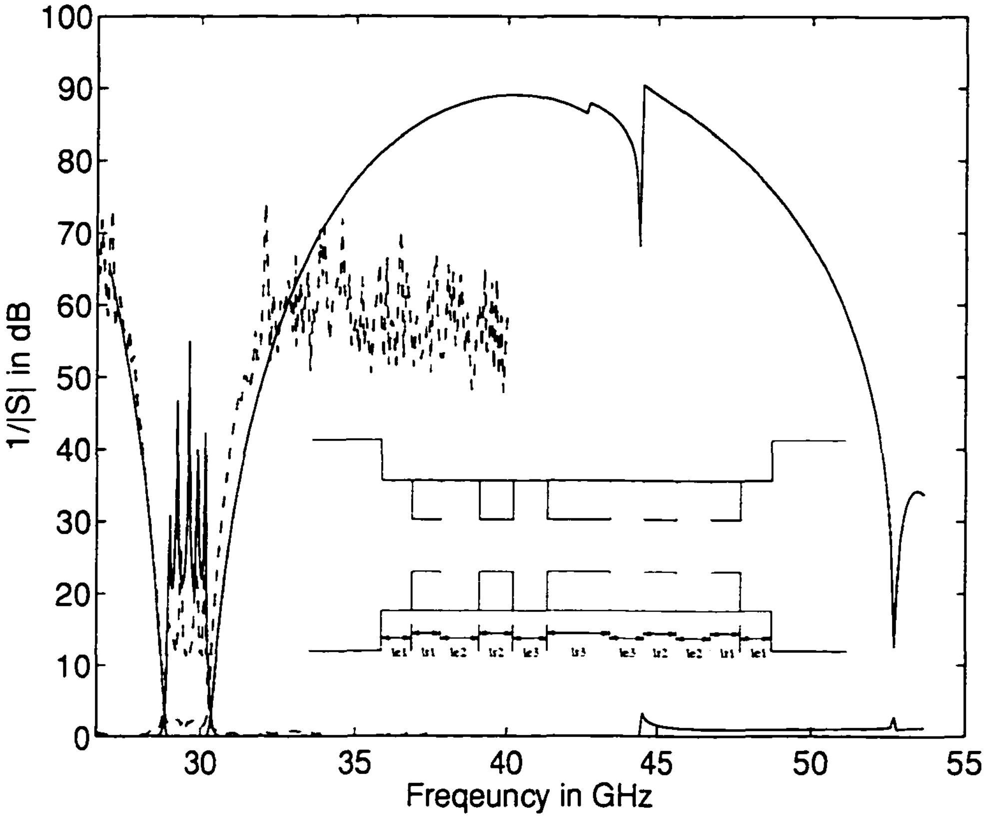

Figure 4.17: Wideband response of the 5-resonator evanescent mode circular waveguide filter, dimensions in mm, radius of input/output section=4, radius of evanescent section=b=2, a=0.4, θ = 5.5deg, le1=.36, lr1=1.07, le2=3.09, lr2=1.74, le3=3.36, lr3=1.74, solid lines-computed response, dashed lines('- -')-measured response

Chapter 5

Analysis of Orthogonal Mode Coupling Elements

Circular and square waveguides support degenerate fundamental modes (and also higher order modes) with orthogonal polarizations. In an unperturbed waveguide the two polarizations do not couple. However, in the presence of any asymmetric discontinuity, coupling between the two orthogonally polarized modes take place. This coupling is essential in the functioning of components such as dual mode filters and polarizers.

A dual mode filter can offer elliptic filter characteristics. Elliptic filters have the advantage of improved stopband characteristics due to the presence of transmission zeros at finite frequencies in contrast to Chebychev or Butterworth response (transmission zeros at infinity). Hence, the number of resonators required to obtain a specified stopband rejection is lower than for Chebychev or Butterworth filters. Also, elliptic filters have equiripple passband characteristics. The transmission zeros at finite frequencies is introduced by coupling nonsuccessive resonant circuits. In microwave filters this coupling can be realized using a multimode cavity. A multimode cavity provides dual, triple or higher mode degeneracies. Two resonant circuits in a single circular or square waveguide cavity are possible due to degenerate orthogonal polarizations. Cross coupling between two adjacent dual mode cavities (but nonsuccessive resonant circuits) produces one real or imaginary pair of poles of the characteristic function. This results in an elliptic-function type filter characteristic. Thus when the cavities in a dual mode filters are inline, the number of pole pairs is half the number of physical cavities present in the filter. In a canonical configuration of dual mode filters, cross coupling between the first and the last resonant circuits is possible [70]. For such a configuration the same physical dual mode resonant cavity becomes the first and last resonator of the filter. Thus an elliptic function characteristic of higher order compared to an inline configuration is realized. Elliptic filters of higher orders can also be realised using multiple mode degeneracies. In order to realize a dual mode mode filter a coupling between the two orthogonal polarization is necessary. In practise this is achieved with a screw placed at 45 degree inclination to the horizontal and vertical polarization inside a cavity. A configuration of the coupling screw in a dual mode filter has been shown in Figure 1.3 of Chapter 1. By varying the depth of penetration of the screw the degree of coupling can be altered. Horizontal and vertical tuning screws (see Figure 1.3) have been used to account for fabrication tolerances or inaccuracies of design. When a rigorous analysis and design procedure is used these tuning screws can be eliminated [45] as accurate prediction of the performance is possible. This chapter deals with the analysis of a discontinuity from an empty circular waveguide to a coupling screw using MMM. In order to avoid a mixed coordinate system the coupling screw has been modeled as ridges of uniform angular thickness in the numerical analysis. It is also possible to fabricate such ridges positioned at an arbitrary angle to the excitation. This type of reshaping the screw to suit the numerical technique has been applied in the literature as well, e.g., the coupling screw has been replaced with a corner cut in a square waveguide cavity [71] in order to compute the coupling rigorously using MMM.

Satellite links often use circularly polarized waves to provide link to mobile users. A circularly polarized wave is represented by the superposition of two orthogonal linearly polarized waves that possess identical magnitude and a phase difference of ±

90 degrees. Hence, frequency reuse is possible with right hand circularly polarized and left hand circularly polarized waves. To generate or discriminate a circularly polarized wave from a linearly polarized wave, polarizers are used. There are several ways to realize polarizers both in square and circular waveguides. One possible configuration is shown in Figure 1.4 of Chapter 1. In this polarizer, a linearly polarized signal at the input is converted to semi signals of orthogonal polarization with a 90 degree differential phase shift between them at the output. Analysis of the basic coupling section of such a polarizer with double ridges of uniform thickness placed at 45 degree inclination to the horizontal and vertical polarization is also presented in this chapter. Since there are two ridges to perform the coupling, more coupling can be achieved in a double ridged asymmetric discontinuity compared to a single ridged asymmetric discontinuity. This structure can also be used in dual mode filters to achieve the coupling between the two orthogonal polarizations.

There is yet another method for the generation and discrimination of circular polarization. This method is based on generating semi signals of linear orthogonal polarization at the first stage using a 3-dB power splitting transition [72]. These semi signals are then fed to a differential phase shifter which produces the ±90 degree phase shift between the orthogonal polarization to generate circular polarization. The differential phase shifter can be designed from a ridged circular waveguide. A quadruple ridged waveguide has been used for this purpose in [73]. The penetration depth and thickness of the horizontal ridges are different from the vertical ridges so as to achieve differing propagation constants for the two modes of orthogonal polarizations. This results in a phase difference between the two polarizations that grows as the waves travel down the ridged waveguide structure. A transformer from an empty circular waveguide to such a quadruple ridged waveguide offering both a good returnloss and a differential phase shift of ±90 degree forms a polarizer unit. A double ridged transformer can also be used in place of a quadruple ridged waveguide design because the propagation constants of horizontal and vertical polarizations are

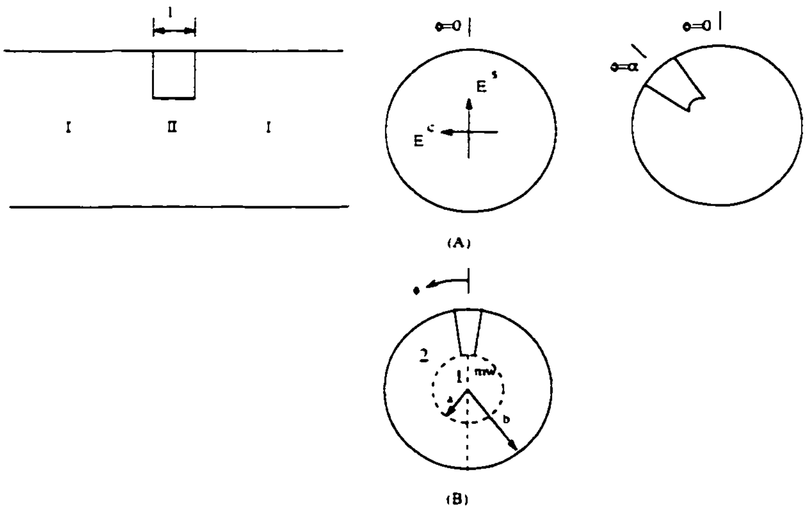

Figure 5.1: (A)Discontinuity regions I & II of the ridged circular waveguide section of finite length (B) Subregions 1 & 2 of section II

different in this structure as well. A differential phase shifter in a double ridged circular waveguide has been designed and optimized at the end of this chapter.

5.1 Circular to single ridged waveguide discontinuity

The cross-section of a discontinuity from an empty circular waveguide to a single ridged circular waveguide with the ridge positioned at an arbitrary angle α is shown in Figure 5.1. At such a discontinuity, which is asymmetric with respect to either the vertical or horizontal polarization, both polarizations of the fundamental and higher order $TE_{n,m}$ and $TM_{n,m}$ modes get excited. The electric and magnetic vector potentials expressed as a sum of incident and reflected waves of unknown amplitudes for the two regions of discontinuity are written as in equations 4.1 and 4.2. The incident and reflected wave amplitudes at such a discontinuity for TE modes of both the polarizations are shown in Figure 5.2. It should be noted that the F^{Ih} of equation 4.1

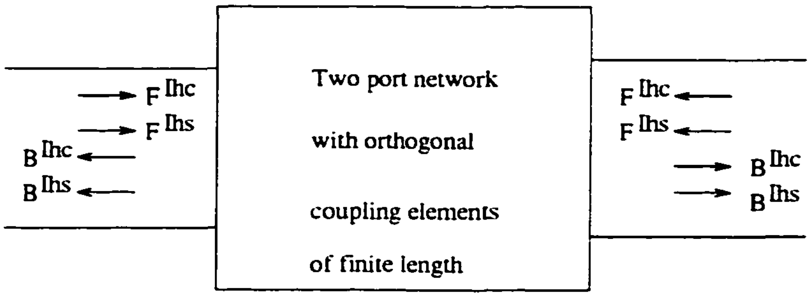

Figure 5.2: Incident and reflected wave amplitudes of a orthogonal polarization coupling network

for this discontinuity has two components namely F^{Ihs} and F^{Ihc} and similarly B^{Ih} has the components B^{Ihs} and B^{Ihc}. Similarly F^{Ie} and B^{Ie} of equation 4.2 have two components. The superscripts 'c' and 's' denote the cosine and sine polarized electric field component E_ρ due to these potentials. This representation of the orthogonal polarization based on the electric field component is shown in Figure 5.1. The potential functions in region I including the two polarizations are expressed as follows:

$$\psi^{(Ih)}(\rho,\phi) = \sum_{m=1}^{M^{hc}} \sum_{n=1}^{N^{hc}} P^{Ihc}_{n,m} J_n(k^{Ihc}_{c_{n,m}}\rho) \sin n\phi + \sum_{m=1}^{M^{hs}} \sum_{n=0}^{N^{hs}} P^{Ihs}_{n,m} J_n(k^{Ihs}_{c_{n,m}}\rho) \cos n\phi \quad (5.1)$$

$$\psi^{(Ie)}(\rho,\phi) = \sum_{m=1}^{M^{ec}} \sum_{n=0}^{N^{ec}} P^{Iec}_{n,m} J_n(k^{Iec}_{c_{n,m}}\rho) \cos n\phi + \sum_{m=1}^{M^{es}} \sum_{n=1}^{N^{es}} P^{Ies}_{n,m} J_n(k^{Ies}_{c_{n,m}}\rho) \sin n\phi \quad (5.2)$$

The power normalization constants for a circular waveguide of radius b are given in equations (4.7) and (4.8) for the cosine and sine polarization.

For the single ridged circular waveguide region once again the potential functions include the modes for both polarizations. The eigenvalues of the orthogonal TE and TM modes of the single ridged waveguide are evaluated from electric and magnetic wall symmetries at $\phi = 0$ as described in Chapter 3. As the ridge is positioned at an angle α, the potential functions corresponding to the orthogonal polarizations must incorporate the boundary condition due to this angular displacement. This implies that the potential functions are written using the electric and magnetic wall symmetry lines at $\phi = \alpha$. However, the eigenvalues evaluated with the ridge positioned at $\alpha = 0$ can still be used in these equations because the eigenvalues do not change with the rotation of the ridge. The superscripts 'c' and 's' are again used in these potentials to denote the two orthogonal polarizations with magnetic wall (mw) and electric wall (ew) symmetries at $\phi = \alpha$, respectively. Although this nomenclature is not meaningful in the single ridged waveguide, it allows easy identification of the polarizations and has hence been used. The potential function of region II are written as follows:

$$\begin{aligned}\psi^{(IIh)}(\rho,\phi) &= \sum_{r=1}^{Rs}(\psi^{(1hs)}(\rho,\phi) + \psi^{(2hs)}(\rho,\phi)) + \\ &\quad \sum_{r=1}^{Rc}(\psi^{(1hc)}(\rho,\phi) + \psi^{(2hc)}(\rho,\phi)) \qquad (5.3)\end{aligned}$$

where the functions on right hand side of the above equation are,

$$\psi^{(1hc)}(\rho,\phi) = \sum_{n=1}^{N1c} A_n^c J_n(k_{c_r}^{IIhc}\rho)\sin n(\phi-\alpha) \qquad (5.4)$$

$$\psi^{(1hs)}(\rho,\phi) = \sum_{n=0}^{N1s} A_n^s J_n(k_{c_r}^{IIhs}\rho)\cos n(\phi-\alpha) \qquad (5.5)$$

$$\begin{aligned}\psi^{(2hc)}(\rho,\phi) &= \sum_{m=1,3}^{N2c} C_m^c[Y_l'(k_{c_r}^{IIhc}b)J_l(k_{c_r}^{IIhc}\rho) - J_l'(k_{c_r}^{IIhc}b)Y_l(k_{c_r}^{IIhc}\rho)] \\ &\quad \cdot\cos l(\phi-\theta-\alpha) \qquad l = \frac{m\pi}{2(\pi-\theta)} \text{ for mw at } \phi=\alpha \qquad (5.6)\end{aligned}$$

$$\begin{aligned}\psi^{(2hs)}(\rho,\phi) &= \sum_{m=0}^{N2s} C_m^s[Y_l'(k_{c_r}^{IIhs}b)J_l(k_{c_r}^{IIhs}\rho) - J_l'(k_{c_r}^{IIhs}b)Y_l(k_{c_r}^{IIhs}\rho)] \\ &\quad \cdot\cos l(\phi-\theta-\alpha) \qquad l = \frac{m\pi}{\pi-\theta} \text{ for ew at } \phi=\alpha \qquad (5.7)\end{aligned}$$

$$\begin{aligned}\psi^{(IIe)}(\rho,\phi) &= \sum_{r=1}^{Rs}(\psi^{(1es)}(\rho,\phi)+\psi^{(2es)}(\rho,\phi))+\\ &\quad \sum_{r=1}^{Rc}(\psi^{(1ec)}(\rho,\phi)+\psi^{(2ec)}(\rho,\phi)) \end{aligned} \qquad (5.8)$$

$$\psi^{(1es)}(\rho,\phi) = \sum_{n=1}^{N1s} B_n^s J_n(k_{c_r}^{IIes}\rho)\sin n(\phi-\alpha) \qquad (5.9)$$

$$\psi^{(1ec)}(\rho,\phi) = \sum_{n=0}^{N1c} B_n^c J_n(k_{c_r}^{IIec}\rho)\cos n(\phi-\alpha) \qquad (5.10)$$

$$\begin{aligned}\psi^{(2ec)}(\rho,\phi) &= \sum_{m=1,3}^{N2c} D_m^c[N_l(k_{c_r}^{IIec}b)J_l(k_{c_r}^{IIec}\rho)-J_l(k_{c_r}^{IIec}b)N_l(k_{c_r}^{IIec}\rho)]\\ &\quad \cdot\sin l(\phi-\theta-\alpha) \qquad l=\tfrac{m\pi}{2(\pi-\theta)} \text{ for mw at } \phi=\alpha \end{aligned} \qquad (5.11)$$

$$\begin{aligned}\psi^{(2es)}(\rho,\phi) &= \sum_{m=1}^{N2s} D_m^s[N_l(k_{c_r}^{IIes}b)J_l(k_{c_r}^{IIes}\rho)-J_l(k_{c_r}^{IIes}b)N_l(k_{c_r}^{IIes}\rho)]\\ &\quad \cdot\sin l(\phi-\theta-\alpha) \qquad l=\tfrac{m\pi}{\pi-\theta} \text{ for ew at } \phi=\alpha \end{aligned} \qquad (5.12)$$

The modal coefficients and the power normalization constants are once again evaluated for $\alpha = 0$ using the same procedure described in Chapter 4. From these potential functions, the electric and magnetic fields are evaluated in region I and region II and matched at the discontinuity.

Using the orthogonality property of modes, the matching condition is converted to a set of linear equations relating the unknown amplitudes of the incident and reflected waves as given by equations (4.16) and (4.17). The matrices V_{hh}, V_{ee} and V_{eh} of equations (4.16) and (4.17) for this case of asymmetric discontinuity relate the coupling between the orthogonal polarizations as well. Hence these matrices can be expressed in terms of submatrices as shown below:

$$V_{hh} = \begin{pmatrix} L^{cc}_{hh} & L^{cs}_{hh} \\ L^{sc}_{hh} & L^{ss}_{hh} \end{pmatrix} \tag{5.13}$$

$$V_{ee} = \begin{pmatrix} L^{cc}_{ee} & L^{cs}_{ee} \\ L^{sc}_{ee} & L^{ss}_{ee} \end{pmatrix} \tag{5.14}$$

$$V_{eh} = \begin{pmatrix} L^{cc}_{eh} & L^{cs}_{eh} \\ L^{sc}_{eh} & L^{ss}_{eh} \end{pmatrix} \tag{5.15}$$

The superscripts 'ss', 'sc', 'cc', 'cs' indicate the coupling from sine to sine, sine to cosine, cosine to cosine and cosine to sine polarizations of regions I and II, respectively. In other words the submatrices of the above equations relate the two components of the incident and reflected modes shown in Figure 5.2. The size of the coupling matrices depends on the number of modes of both the polarization included in the analysis. The number of the modes used in the ridged and empty circular waveguide for sine polarization are not the same as that for the cosine polarization because only one of the polarizations includes the axisymmetric modes. This can be observed from the equations of the electric and magnetic potential functions.

The elements of V_{hh} are evaluated from the following equations:

$$L^{cc}_{hh}(x,y) = \left(\sum_{n=1}^{N1c} Term_1 + \sum_{m=1,3}^{N2c} Term_2\right)\sqrt{\frac{k_z^{Ihc}(x)}{k_z^{IIhc}(y)}} \tag{5.16}$$

where $Term_1$ and $Term_2$ are given below. The x corresponds to the mode that is excited in cross-section I while y corresponds to that excited in II. Also, k_z represent the propagation constants of the sine or cosine polarization of TE and TM

modes in regions I and II of the corresponding modes. In the following equations of coupling integrals and those given in Appendix F the modal amplitude coefficients of the potential functions in the subregion 2 have been absorbed into the power normalization coefficients of region II.

$$\begin{aligned} Term_1 &= P^{Ihc}_{q,p} P^{IIhc}_{n,r} \\ &\cdot \Big(\int_0^a \frac{nq}{\rho} J_q(k^{Ihc}_{c_{q,p}}\rho) J_n(k^{IIhc}_{c_r}\rho) d\rho \int_\alpha^{2\pi+\alpha} \cos q\phi \cos n(\phi-\alpha) d\phi \\ &+ J'_q(k^{Ihc}_{c_{q,p}}\rho) J'_n(k^{IIhc}_{c_r}\rho)\rho d\rho \int_\alpha^{2\pi+\alpha} \sin q\phi \sin n(\phi-\alpha) d\phi \Big) \qquad (5.17) \end{aligned}$$

$$\begin{aligned} Term_2 &= P^{Ihc}_{q,p} P^{IIhc}_{m,r} \int_a^b -\frac{lq}{\rho^2} J_q(k^{Ihc}_{c_{q,p}}\rho)[J_l(k^{IIhc}_{c_r}\rho) N'_l(k^{IIhc}_{c_r}b) \\ &- J'_l(k^{IIhc}_{c_r}b) N_l(k^{IIhc}_{c_r}\rho)]\rho d\rho \int_{\alpha+\theta}^{2\pi+\alpha-\theta} \cos q\phi \sin l(\phi-\alpha-\theta) d\phi \\ &+ P^{(Ihc)}_{q,p} P^{(IIhc)}_{m,r} \int_a^b J'_q(k^{Ihc}_{c_{q,p}}\rho)[J'_l(k^{IIhc}_{c_r}\rho) N'_l(k^{IIhc}_{c_r}b) \\ &- J'_l(k^{IIhc}_{c_r}b) N'_l(k^{IIhc}_{c_r}\rho)]\rho d\rho \int_{\alpha+\theta}^{2\pi+\alpha-\theta} \sin q\phi \cos l(\phi-\alpha-\theta) d\phi \quad (5.18) \end{aligned}$$

where $l = \frac{m\pi}{2(\pi-\theta)}$

$$L^{ss}_{hh}(x,y) = (\sum_{n=0}^{N1s} Term_3 + \sum_{m=0}^{N2s} Term_4)\sqrt{\frac{k_z^{Ihs}(x)}{k_z^{IIhs}(y)}} \qquad (5.19)$$

$$
\begin{aligned}
Term_3 &= P_{q,p}^{(Ihs)} P_{n,r}^{(IIhs)} \\
&\cdot \left(\int_0^a \frac{nq}{\rho} J_q(k_{c_{q,p}}^{Ihs}\rho) J_n(k_{c_r}^{IIhs}\rho) d\rho \int_\alpha^{2\pi+\alpha} \sin qo \sin n(o-\alpha) do \right. \\
&\left. + J_q'(k_{c_{q,p}}^{Ihs}\rho) J_n'(k_{c_r}^{IIhs}\rho)\rho d\rho \int_\alpha^{2\pi+\alpha} \cos qo \cos n(o-\alpha) do \right) \qquad (5.20)
\end{aligned}
$$

$$
\begin{aligned}
Term_4 &= P_{q,p}^{Ihs} P_{m,r}^{IIhs} \int_a^b \frac{lq}{\rho^2} J_q(k_{c_{q,p}}^{Ihs}\rho)[J_l(k_{c_r}^{IIhs}\rho) N_l'(k_{c_r}^{IIhs} b) \\
&- J_l'(k_{c_r}^{IIhs} b) N_l(k_{c_r}^{IIhs}\rho)]\rho d\rho \int_{\alpha+\theta}^{2\pi+\alpha-\theta} \sin qo \sin l(o-\alpha-\theta) do \\
&+ P_{q,p}^{(Ihs)} P_{m,r}^{(IIhs)} \int_a^b J_q'(k_{c_{q,p}}^{Ihs}\rho)[J_l'(k_{c_r}^{IIhs}\rho) N_l'(k_{c_r}^{IIhs} b) \\
&- J_l'(k_{c_r}^{IIhs} b) N_l'(k_{c_r}^{IIhs}\rho)]\rho d\rho \int_{\alpha+\theta}^{2\pi+\alpha-\theta} \cos qo \cos l(o-\alpha-\theta) do \quad (5.21)
\end{aligned}
$$

where $l = \frac{m\pi}{(\pi-\theta)}$

$$
L_{hh}^{cs}(x,y) = \left(\sum_{n=0}^{N1s} Term_5 + \sum_{m=0}^{N2s} Term_6\right)\sqrt{\frac{k_z^{Ihc}(x)}{k_z^{IIhs}(y)}} \qquad (5.22)
$$

$$
\begin{aligned}
Term_5 &= P_{q,p}^{(Ihc)} P_{n,r}^{(IIhs)} \\
&\cdot \left(\int_0^a \frac{nq}{\rho} J_q(k_{c_{q,p}}^{Ihc}\rho) J_n(k_{c_r}^{IIhs}\rho) d\rho \int_\alpha^{2\pi+\alpha} -\cos qo \sin n(o-\alpha) do \right. \\
&\left. + J_q'(k_{c_{q,p}}^{Ihc}\rho) J_n'(k_{c_r}^{IIhs}\rho)\rho d\rho \int_\alpha^{2\pi+\alpha} \sin qo \cos n(o-\alpha) do \right) \qquad (5.23)
\end{aligned}
$$

$$\begin{aligned} Term_6 \;=\;& P_{q,p}^{Ihc} P_{m,r}^{IIhs} \int_a^b -\frac{lq}{\rho^2} J_q(k_{c_{q,p}}^{Ihc}\rho)[J_l(k_{c_r}^{IIhs}\rho) N_l'(k_{c_r}^{IIhs}b) \\ & -J_l'(k_{c_r}^{IIhs}b) N_l(k_{c_r}^{IIhs}\rho)]\rho d\rho \int_{\alpha+\theta}^{2\pi+\alpha-\theta} \cos qo \sin l(o-\alpha-\theta) do \\ & +P_{q,p}^{(Ihs)} P_{m,r}^{(IIhs)} \int_a^b J_q'(k_{c_{q,p}}^{Ihc}\rho)[J_l'(k_{c_r}^{IIhs}\rho) N_l'(k_{c_r}^{IIhs}b) \\ & -J_l'(k_{c_r}^{IIhs}b) N_l'(k_{c_r}^{IIhs}\rho)]\rho d\rho \int_{\alpha+\theta}^{2\pi+\alpha-\theta} \sin qo \cos l(o-\alpha-\theta) do \quad (5.24) \end{aligned}$$

where $l = \frac{m\pi}{(\pi-\theta)}$

$$L_{hh}^{sc}(x,y) = (\sum_{n=1}^{N1c} Term_7 + \sum_{m=1,3}^{N2c} Term_8)\sqrt{\frac{k_z^{Ihs}(x)}{k_z^{IIhc}(y)}} \qquad (5.25)$$

$$\begin{aligned} Term_7 \;=\;& P_{q,p}^{(Ihs)} P_{n,r}^{(IIhc)} \\ & \cdot\left(\int_0^a \frac{nq}{\rho} J_q(k_{c_{q,p}}^{Ihs}\rho) J_n(k_{c_r}^{IIhc}\rho) d\rho \int_\alpha^{2\pi+\alpha} -\sin qo \cos n(o-\alpha) do \right. \\ & \left. + J_q'(k_{c_{q,p}}^{Ihs}\rho) J_n'(k_{c_r}^{IIhc}\rho)\rho d\rho \int_\alpha^{2\pi+\alpha} \cos qo \sin n(o-\alpha) do\right) \qquad (5.26) \end{aligned}$$

$$\begin{aligned} Term_8 \;=\;& P_{q,p}^{Ihs} P_{m,r}^{IIhc} \int_a^b \frac{lq}{\rho^2} J_q(k_{c_{q,p}}^{Ihs}\rho)[J_l(k_{c_r}^{IIhc}\rho) N_l'(k_{c_r}^{IIhc}b) \\ & -J_l'(k_{c_r}^{IIhc}b) N_l(k_{c_r}^{IIhc}\rho)]\rho d\rho \int_{\alpha+\theta}^{2\pi+\alpha-\theta} \sin qo \sin l(o-\alpha-\theta) do \\ & +P_{q,p}^{(Ihs)} P_{m,r}^{(IIhc)} \int_a^b J_q'(k_{c_{q,p}}^{Ihs}\rho)[J_l'(k_{c_r}^{IIhc}\rho) N_l'(k_{c_r}^{IIhc}b) \\ & -J_l'(k_{c_r}^{IIhc}b) N_l'(k_{c_r}^{IIhc}\rho)]\rho d\rho \int_{\alpha+\theta}^{2\pi+\alpha-\theta} \cos qo \cos l(o-\alpha-\theta) do \quad (5.27) \end{aligned}$$

where $l = \frac{m\pi}{2(\pi-\theta)}$

The other coupling integrals of the submatrices of equation (5.14) and (5.15) are given in Appendix F. The continuity of the tangential components of the H-field results in the transpose of the coupling matrices of equations (5.13), (5.14) and (5.15) to relate the unknown field coefficients. By using all these coupling matrices as described in Appendix B the generalized S-matrix of the orthogonal polarizations at a discontinuity from an empty circular waveguide to a single ridged circular waveguide is obtained. Cascading the generalized S-matrices (as given in Appendix C) of the step from an empty circular waveguide to a single ridged waveguide and back, the overall S-matrix of a single ridged waveguide of finite length is obtained.

Since the analysis of such a discontinuity involves both the polarizations, the S-matrix of the fundamental orthogonal polarization extracted from the generalized scattering matrix is a 4×4 matrix. As mentioned earlier, the sine polarization is the one with the E_ρ field component varying sinusoidally with ϕ and the cosine polarization is orthogonal to this. In the following discussions and figures, the subscripts 'sc' and 'cs' of the S-parameters denote the coupling from sine to cosine and cosine to sine polarizations, respectively. The subscripts 's' and 'c' denote the coupling from sine to sine and cosine to cosine polarizations, respectively. For a discontinuity with a finitely long single ridge, S_{12sc} and S_{12cs} are equal and so are the S_{11sc} and S_{11cs}, which is due to the symmetry property of the S-matrix.

The computed S-parameters for a single ridged circular waveguide of finite length is tested for convergence. It can be observed from Figure 5.3 that convergence (S_{12sc} is shown) occurs when 70 modes of both the polarizations of $TE_{n,m}$ and $TM_{n,m}$ modes are included. In this analysis the ridge is placed at $\alpha = 45$ degree. Figures 5.4 and 5.5 show the variation of the S-parameters of such a discontinuity with frequency. For $\alpha = 45$ degree the discontinuity looks alike for both sine and cosine polarization. Hence the S_{11c} and S_{11s} are equal and similarly S_{12c} and S_{12s} are also equal. The

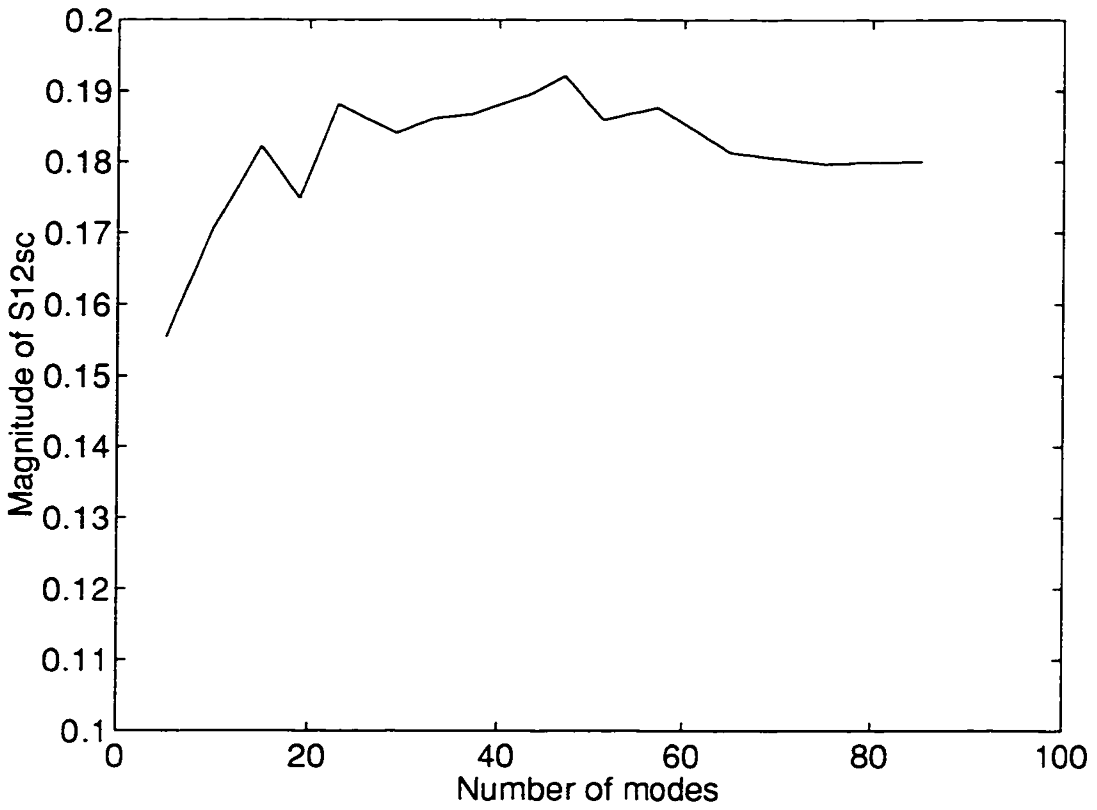

Figure 5.3: Convergence of the magnitude of S_{12sc} at a discontinuity from a circular waveguide to a single ridged circular waveguide versus the number of TE and TM modes of both polarizations. b=1.0cm. a=0.4cm. $\alpha = 45$deg. $\theta = 5$deg. l=1.0mm. f=10GHz

theoretically computed values are very close to each other as shown in Figure 5.4. However, these S-parameters are not equal for the other values of α.

When the ridge is positioned such that $\alpha = 0$, then the orthogonal polarizations do not couple. This can also be concluded from equations (5.22) and (5.25). In this case, the submatrices L^{cs}_{hh}, L^{sc}_{hh}, L^{cs}_{ee}, L^{sc}_{ee}, L^{cs}_{eh} and L^{sc}_{eh} become identically zero. Placing the ridge along $\alpha = 0$ and $\alpha = \pi/2$ is identical, because at these ridge positions the orthogonal polarizations are decoupled. However, if in the algorithm α is set to $\pi/2$, mathematically some of the elements of submatrices L^{cc}_{hh}, L^{ss}_{hh} L^{cc}_{ee}, L^{ss}_{ee}, L^{cc}_{eh} and L^{ss}_{eh}

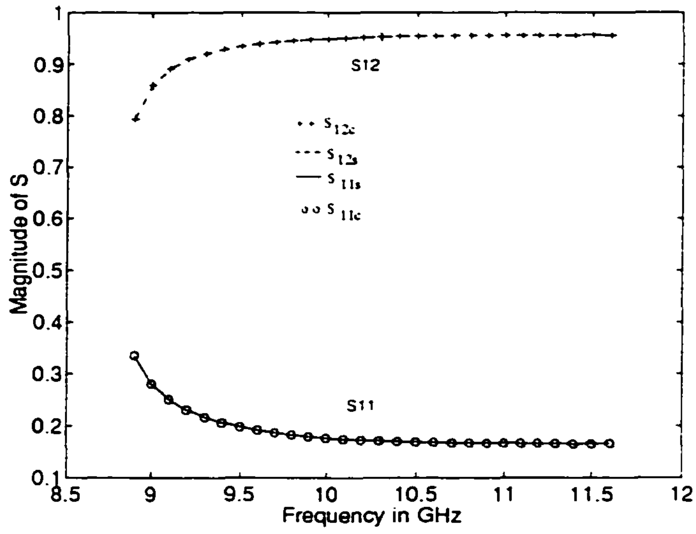

Figure 5.4: Magnitude of S-parameters of a discontinuity from circular waveguide to single ridged circular waveguide of finite length. b=1.0cm. a=0.4cm. α = 45deg. θ = 5deg. l=1.0mm.

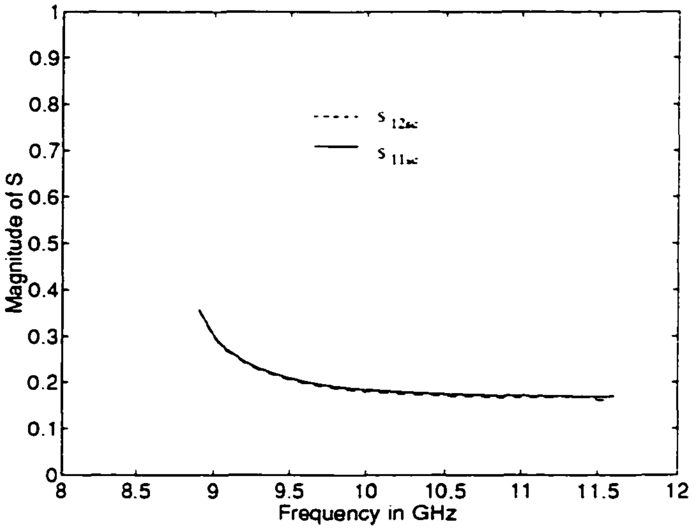

Figure 5.5: Magnitude of S-parameters of a discontinuity from circular waveguide to single ridged circular waveguide of finite length. b=1.0cm. a=0.4cm. α = 45deg. θ = 5deg. l=1.0mm

become zero which should not be the case. Incorrect solutions are thus obtained when using $\alpha = \pi/2$ owing to the symmetric discontinuity being treated mathematically as asymmetric. Hence this setting should be avoided in the algorithm.

The parameter S_{12sc} for various α is shown in Figure 5.6. It can be concluded that for $\alpha = 45$ degree, maximum coupling between the orthogonal polarizations is obtained. This has been verified in Figure 5.6. Also, it can be observed that because of rotational symmetry of the discontinuity, S_{12sc} at $\alpha = 30$ degree is equal to that at $\alpha = 60$ degree. Similarly S_{12sc} at $\alpha = 15$ degree is equal to that at $\alpha = 75$ degree. Once again, due to rotational symmetry, for $\alpha = 30$ degree and $\alpha = 60$ degree, the other S-parameters like S_{11s} and S_{12s} are interchanged with S_{11c} and S_{12c}, respectively, as shown in Figures 5.7 and 5.8.

When the depth of penetration of the ridge increases, the parameter S_{12sc} should increase because the coupling between the orthogonal polarizations is increased. This is shown in Figure 5.9.

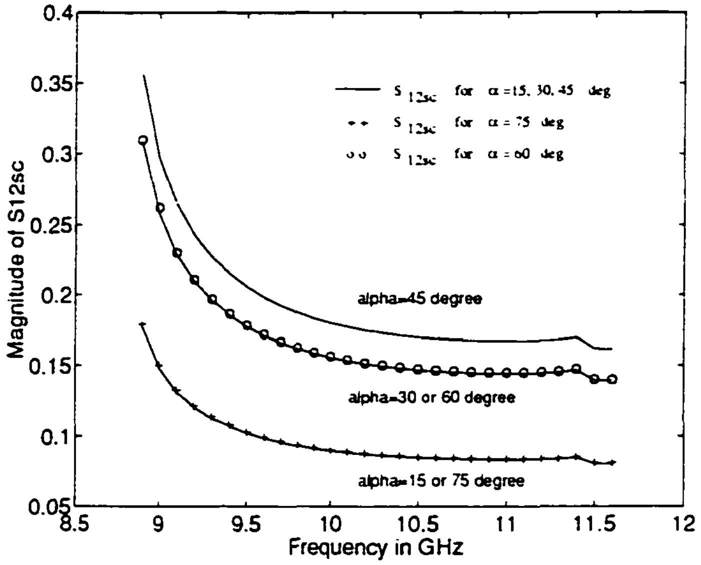

Figure 5.6: Magnitude of S-parameters of a discontinuity from circular waveguide to single ridged circular waveguide of finite length. b=1.0cm. a=0.4cm. θ = 5deg. l=1.0mm.

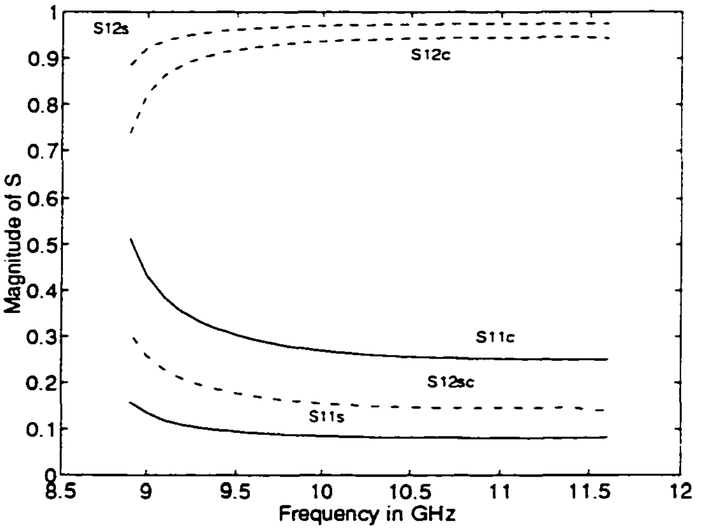

Figure 5.7: Magnitude of S-parameters of a discontinuity from circular waveguide to single ridged circular waveguide of finite length. b=1.0cm. a=0.4cm. α = 30deg. θ = 5deg. l=1.0mm.

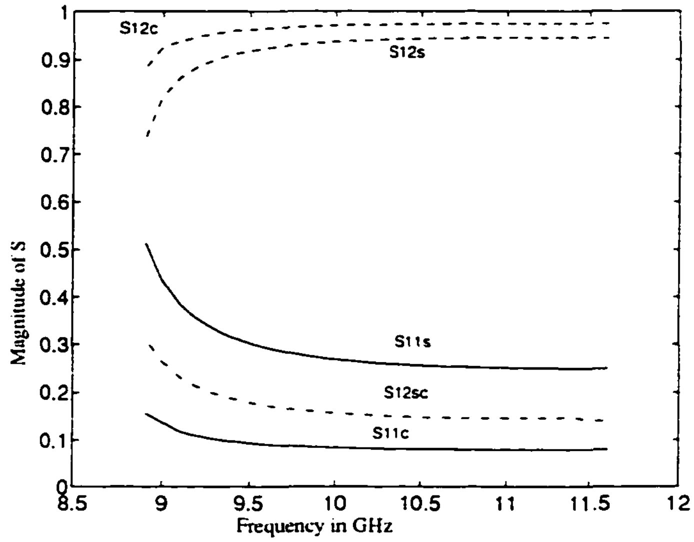

Figure 5.8: Magnitude of S-parameters of a discontinuity from circular waveguide to single ridged circular waveguide of finite length, b=1.0cm, a=0.4cm, $\alpha = 60$deg, $\theta = 5$deg, l=1.0mm.

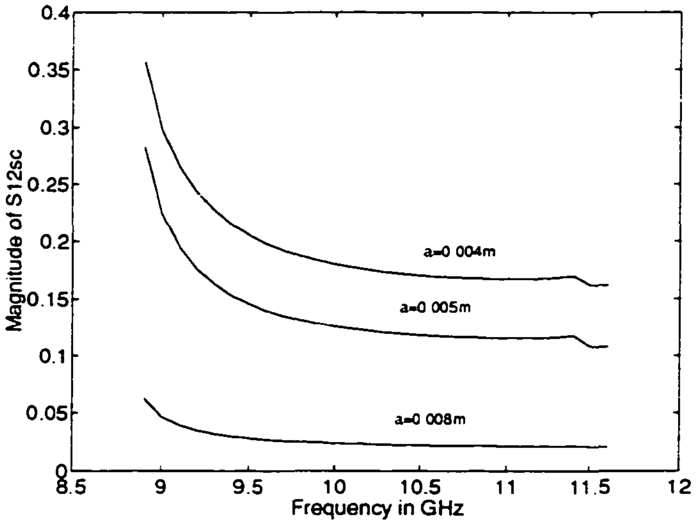

Figure 5.9: Magnitude of S_{12sc} of a discontinuity from circular waveguide to single ridged circular waveguide of finite length, b=1.0cm, $\alpha = 45$deg, $\theta = 5$deg, l=1.0mm, for various values of 'a'

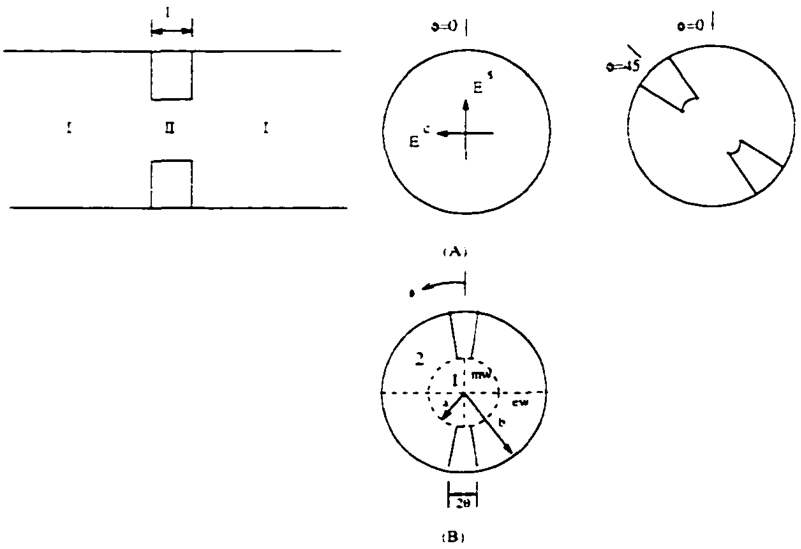

Figure 5.10: (A) Discontinuity regions I & II of the double ridged circular waveguide section of finite length (B) Subregions 1 & 2 of section II

5.2 Asymmetric double ridged waveguide discontinuity

As mentioned earlier, a polarizer is a component that changes a linear polarization into a circular polarization. There are a number of design variants of a polarizer in square and circular waveguide technology [72]. The discontinuity discussed in this section can be used as a basic unit of a polarizer In fact the polarizer of Figure 1.4 can also be modified to a tapered ridged waveguide similar to the design in a square waveguide as discussed in [74], and the same basic unit discussed here can be used to design a polarizer by cascading the scattering matrices of individual discontinuities.

Figure 5.10(A) shows a double ridged waveguide placed asymmetric to the $TE_{1,1}$ excitation in a circular waveguide. For the region I, the potential functions are identical to those in equations (5.1) and (5.2). The eigenvalues of the double ridged waveguide as evaluated in Chapter 3 can be used to write the potential functions in the region II of the discontinuity. However, the potential functions are required to satisfy the boundary conditions due to the rotation of the ridge by α. The orthogonal polarizations of all the modes of region II are identified with superscripts 'c' and 's' and are expressed as a sum of the potential functions of the subregions 1 and 2 as in equation (5.3) and (5.8).

The boundary conditions of subregion 1 of the double ridged waveguide is identical to that of a single ridged waveguide and hence for this subregion the potential functions are similar to that in a single ridged waveguide. But, unlike in the single ridged waveguide, in a double ridged waveguide there are four possible symmetries that yield these orthogonal polarization (Figure 5.10(B)). These symmetries are discussed below with relevance to those in a single ridged waveguide. The potential function $\psi^{(1hc)}$ is given by equation (5.4) where $n = 1, 3 \cdots$ represent the symmetry 'mw' at $\phi = \alpha$ and 'ew' at $\phi = \alpha + \pi/2$, while $n = 2, 4 \cdots$ represent the symmetry 'mw' at $\phi = \alpha$ and 'mw' at $\phi = \alpha + \pi/2$. Similarly the potential function $\psi^{(1hs)}$ is given by equation (5.5) where $n = 1, 3 \cdots$ represent the symmetry 'ew' at $\phi = \alpha$ and 'mw' at $\phi = \alpha + \pi/2$, while $n = 0, 2 \cdots$ represent the symmetry 'ew' at $\phi = \alpha$ and 'ew' at $\phi = \alpha + \pi/2$. Also, the potential function $\psi^{(1ec)}$ is given by equation (5.10) where $n = 0, 2 \cdots$ represent the symmetry 'mw' at $\phi = \alpha$ and 'ew' at $\phi = \alpha + \pi/2$, while $n = 1, 3 \cdots$ represent the symmetry 'mw' at $\phi = \alpha$ and 'mw' at $\phi = \alpha + \pi/2$. And the potential function $\psi^{(1es)}$ is given by equation (5.9) where $n = 2, 4 \cdots$ represent the symmetry 'ew' at $\phi = \alpha$ and 'ew' at $\phi = \alpha + \pi/2$, while $n = 1, 3 \cdots$ represent the symmetry 'ew' at $\phi = \alpha$ and 'mw' at $\phi = \alpha + \pi/2$.

For the subregion 2 the potential functions are as follows:

$$\psi^{(2hc)}(\rho,\phi) = \sum_{m=0}^{N2c} C_m^c [N_l'(k_{cr}^{IIhc}b)J_l(k_{cr}^{IIhc}\rho) - J_l'(k_{cr}^{IIhc}b)N_l(k_{cr}^{IIhc}\rho)] \cdot \cos l(\phi - \theta - \alpha) \tag{5.28}$$

where $l = \frac{m\pi}{(\pi-2\theta)}$. Also here even values of m correspond to the modes with 'mw' at $\phi = \alpha$ and 'ew' at $\phi = \alpha + \pi/2$ and odd values of m correspond to the modes with 'mw' at $\phi = \alpha$ and 'mw' at $\phi = \alpha + \pi/2$

$$\psi^{(2hs)}(\rho,\phi) = \sum_{m=0}^{N2s} C_m^s [N_l'(k_{cr}^{IIhs}b)J_l(k_{cr}^{IIhs}\rho) - J_l'(k_{cr}^{IIhs}b)N_l(k_{cr}^{IIhs}\rho)] \cdot \cos l(\phi - \theta - \alpha) \tag{5.29}$$

where $l = \frac{m\pi}{(\pi-2\theta)}$. Even values of m correspond to the modes with 'ew' at $\phi = \alpha$ and 'ew' at $\phi = \alpha + \pi/2$ and odd values of m correspond to the modes with 'ew' at $\phi = \alpha$ and 'mw' at $\phi = \alpha + \pi/2$.

$$\psi^{(2ec)}(\rho,\phi) = \sum_{m=1}^{N2c} D_m^c [N_l(k_{cr}^{IIec}b)J_l(k_{cr}^{IIec}\rho) - J_l(k_{cr}^{IIec}b)N_l(k_{cr}^{IIec}\rho)] \cdot \sin l(\phi - \theta - \alpha) \tag{5.30}$$

where $l = \frac{m\pi}{(\pi-2\theta)}$. Even values of m correspond to the modes with 'mw' at $\phi = \alpha$ and 'ew' at $\phi = \alpha + \pi/2$ and odd values of m for the modes with 'mw' at $\phi = \alpha$ and 'mw' at $\phi = \alpha + \pi/2$.

$$\psi^{(2es)}(\rho,\phi) = \sum_{m=1}^{N2s} D_m^s [N_l(k_{cr}^{IIes}b)J_l(k_{cr}^{IIes}\rho) - J_l(k_{cr}^{IIes}b)N_l(k_{cr}^{IIes}\rho)] \cdot \sin l(\phi - \theta - \alpha) \tag{5.31}$$

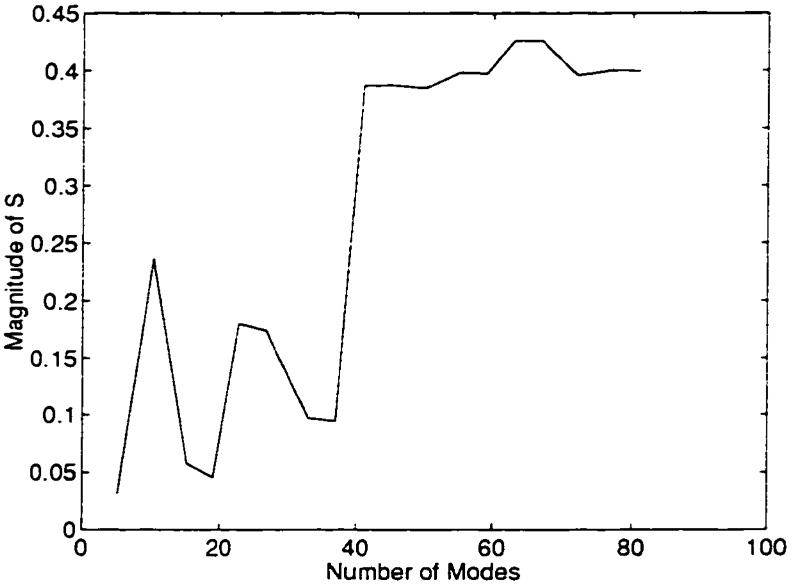

Figure 5.11: Magnitude of S_{12sc} of a discontinuity from circular waveguide to double ridged circular waveguide of finite length, b=1cm, a=0.5cm, α = 45deg, θ = 20deg, l=1.0mm, f=10GHz

where $l = \frac{m\pi}{(\pi-2\theta)}$. Even values of m correspond to modes with 'ew' at $\phi = \alpha$ and 'ew' at $\phi = \alpha + \pi/2$ and odd values of m correspond to modes with 'ew' at $\phi = \alpha$ and 'mw' at $\phi = \alpha + \pi/2$.

From the matching condition of the tangential components of E and H fields at the discontinuity, the coupling matrices are obtained. The coupling matrices V_{hh}, V_{ee} and V_{eh} are expressed in terms of submatrices as in equations (5.13), (5.14) and (5.15). The integrals of the coupling matrices closely resemble those of the single ridged case. Hence, the coupling integrals of the submatrices of V_{hh} alone are given in detail in Appendix G as an example. Similarly, the coupling matrices V_{ee} and V_{eh} are derived and the discontinuity from a circular waveguide to a double ridged waveguide with the ridges positioned at any arbitrary angle can be computed.

The discontinuity from a circular waveguide to a finite length double ridged cir-

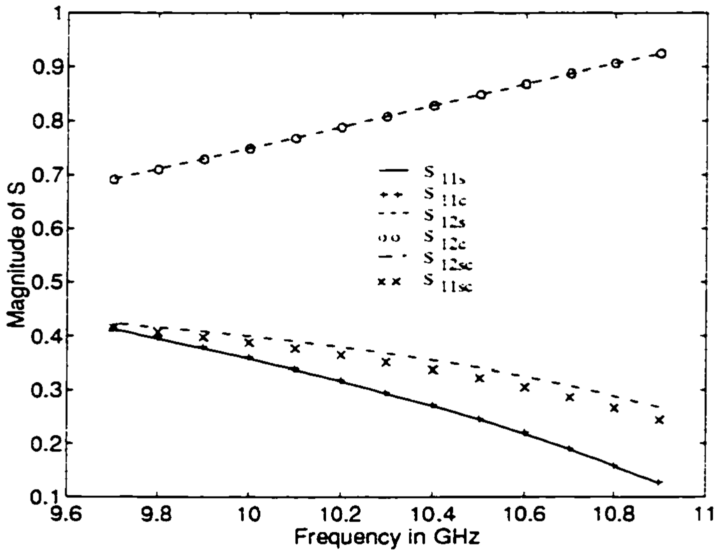

Figure 5.12: Magnitude of S-parameters of a discontinuity from circular waveguide to double ridged circular waveguide of finite length. b=1cm. a=0.5cm. α = 45deg. θ = 10deg. l=1.0mm

cular waveguide with the ridge positioned at $\alpha = 45$ degree has been computed by cascading the generalized S-matrices as explained in Appendix C. The convergence of the S_{12sc} versus the number of modes considering both the polarizations are incident is shown in Figure 5.11. About 60 modes are found sufficient for this analysis. Figure 5.12 shows the variation of S-parameters with frequency for such a discontinuity. Similar to the circular to single ridged waveguide discontinuity. with the ridge positioned at 45 degree to the vertical and horizontal polarizations. the S_{11c} and S_{11s} are equal in this discontinuity as well. Also. S_{12c} is equal to S_{12s}. S_{12sc} is equal to S_{12cs}. and S_{11cs} is equal to S_{11sc}.

The discontinuity from empty circular waveguide to a double ridged waveguide of finite length with the ridge positioned at $\alpha = 0$ has also been computed using the above algorithm. For $\alpha = 0$. the submatrices L^{cs}_{hh}. L^{sc}_{hh}. L^{cs}_{ee}. L^{sc}_{ee}. L^{cs}_{eh} and L^{sc}_{eh} become identically zero. similar to the single ridged discontinuity. In other words there is

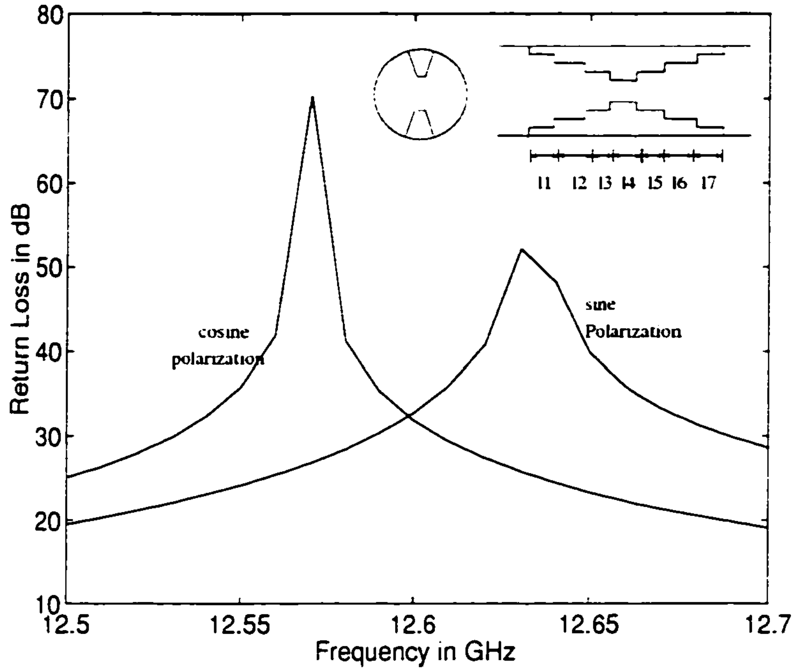

Figure 5.13: Return Loss of orthogonal polarizations of the differential phase shifter unit of a polarizer Dimension in cm. section 1 and section 7: a=0.9. b=1.0. l1=1.338. section 2 and section 6: a=0.7 b=1.0. l2=1.025. section 3 and section 5: a=0.56. b=1.0. l3=1.118. section 4: a=0.5. b=1.0. l4=3.680

no coupling between the orthogonal polarization as the discontinuity reduces to the symmetric discontinuity discussed in Chapter 4. For such a symmetric discontinuity. $TE_{n,m}$ and $TM_{n,m}$ modes with n even have not been included in the analysis. The resulting S-parameters of the fundamental mode (cosine polarized) are the same as the theoretical values of Figure 4.4. The S-parameters of the fundamental orthogonal (sine polarized) mode was verified to satisfy the unitary relationship. The analysis of this discontinuity including both the polarizations has been used to design a differential phase shifter utilized for a polarizer.

A three section Chebychev transformer for the cosine polarized mode was first designed using the fundamental mode theory. The response of the initial design was

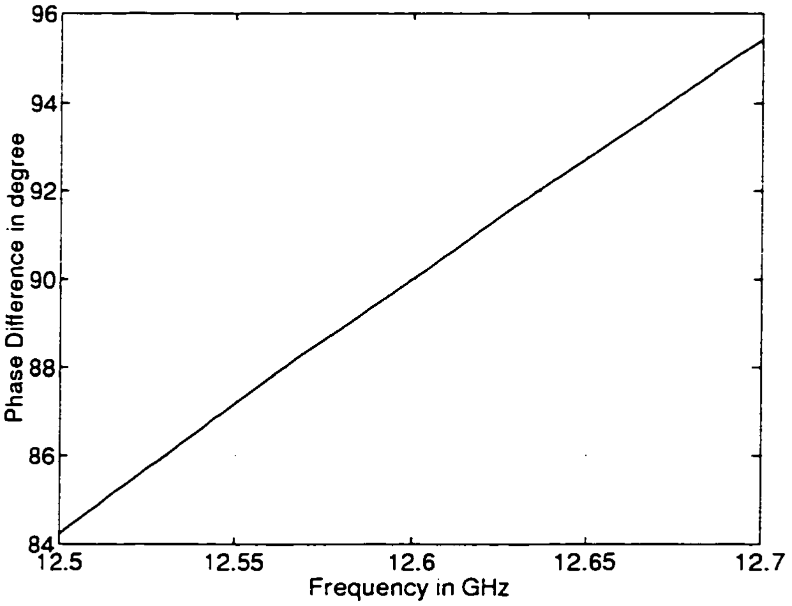

Figure 5.14: Phase difference between the orthogonal polarizations of the differential phase shifter unit of the above polarizer

optimized for a good return loss performance of both the polarizations and for a 90 degree phase shift between them at midband, by altering the length of each ridged section. The number of modes used in the optimization was 20 TE and TM modes of each polarization. The final analysis was performed including 40 TE and TM modes of each polarization. The return loss and phase response of this type of polarizer unit is shown in Figures 5.13 and 5.14 The bandwidth of such a polarizer is not as high as the corrugated waveguide polarizer that in square waveguide technology [75]. However, it should be noted that the capacitive iris of [75] in square waveguides can be realized only as a corrugated or ridged structure in circular waveguides.

Chapter 6

Conclusions

6.1 Conclusions

The major objective of this research has been to expand the mode matching method as an accurate numerical design tool for the design of filters and matching networks in circular waveguide technology. Rigorous analysis and design of these components is essential for modern microwave and satellite communication systems. Selected components have been designed utilizing the MMM developed in this thesis.

Chapter 1 gives a survey on the available numerical methods and their advantages and disadvantages. From the methods available to rigorously solve electromagnetic field problems. the MMM has been found to be best suited for the design of waveguide components.

Chapter 2 has reviewed the MMM as applied to rectangular waveguides and rectangular coaxial lines. A double step discontinuity in a rectangular waveguide was solved using the MMM. Also. the eigenvalues of ridged rectangular waveguide and rectangular coaxial line for various symmetries were determined using the MMM. For a rectangular coaxial line. the characteristic impedance was evaluated as well. From a knowledge of the propagation characteristics of fundamental and higher order modes. a step discontinuity in a rectangular coaxial line has been analyzed. A comparison with literature shows a very good agreement for the eigenvalues and S-parameters of discontinuities analyzed in this chapter. Essentially, this chapter has laid the foundation for an understanding of the fundamentals of this numerical technique. The basic principles of the MMM has been applied to design components in cylindrical coordinate system in the following chapters

The first step in the design of components is a study of the propagation characteristics. Ridged circular waveguides find an important role in the design of filters, polarizers, orthomode transducers etc. In Chapter 3, the eigenvalue analysis of various types of ridged circular waveguides has been discussed. A comparison of the eigenvalues with the literature for single, double and triple ridged waveguides showed very good agreement. The characteristic impedance of double and quadruple ridged circular waveguides was also evaluated in this chapter.

A rigorous analysis of a discontinuity from an empty circular waveguide to a double ridged circular waveguide including the interaction of fundamental and higher order modes was performed in Chapter 4. A metal ridge of uniform angular thickness in the theoretical analysis was fabricated as a thin ridge of rectangular cross-section. The theoretical analysis was compared with measurements and it was found that this approximation did not introduce a large error. Having characterized discontinuities in ridged circular waveguides, the analysis was applied to the design of certain useful components. Based on the characteristic impedance evaluated in Chapter 3, double and quadruple ridged waveguide transformers have been designed. The initial design was analyzed including the interaction of fundamental and higher oder modes and optimized to achieve improved performance. Two types of quadruple ridged waveguide transformer have been designed and a good return loss performance was found. A fifth order evanescent mode filter was also built and measured. The insertion loss was mainly due to the mismatch at the input of the filter and some owing to the poor conductivity of the material.

A single or a double ridge placed at an arbitrary angle to the excitation in an empty circular waveguide couples the orthogonal fundamental polarizations. A rigorous analysis of such a discontinuity has been presented in Chapter 5. This analysis is very useful in the design of polarizers and dual mode filters. A variety of calculations have been performed demonstrating the validity of the algorithms presented in this chapter. A double ridged transformer to realize a polarizer has also been presented in this chapter. A 90 degree differential phase shift between the orthogonally polarized inputs has been achieved by using a double ridged circular waveguide transformer where the ridges are positioned parallel to one excitation and perpendicular to the other.

The results presented in this thesis demonstrate a significant step forward in the rigorous design of components in circular waveguides using the MMM in conjunction with the generalized scattering matrix method.

6.2 Further Work

For the design of orthomode transducers in circular waveguides, it is necessary to characterize a coaxial feed to ridged circular waveguide. The analysis of a coaxial feed to a ridged circular waveguide along with the quadruple ridged transformers designed in Chapter 3 forms a complete orthomode transducer. For such an analysis, the inner conductor of the coaxial line can once again be approximated as conically shaped.

In conjunction with the analysis of a discontinuity from rectangular waveguide to circular waveguide presented in [76,77] and the analysis of orthomode coupling elements discussed in Chapter 5, a dual mode filter can be analyzed and designed rigorously.

A circular waveguide polarizer shown in Figure 1.4 can be designed by cascading several discontinuities of double ridged circular waveguides presented in Chapter 5.

The analysis of a discontinuity from empty circular waveguide to a single ridged circular waveguide can be used to design a septum polarizer in circular waveguides shown in Figure 6.1. An approximation of the thin metal septum as ridges of finite angular thickness is necessary for an analysis of this type of polarizer.

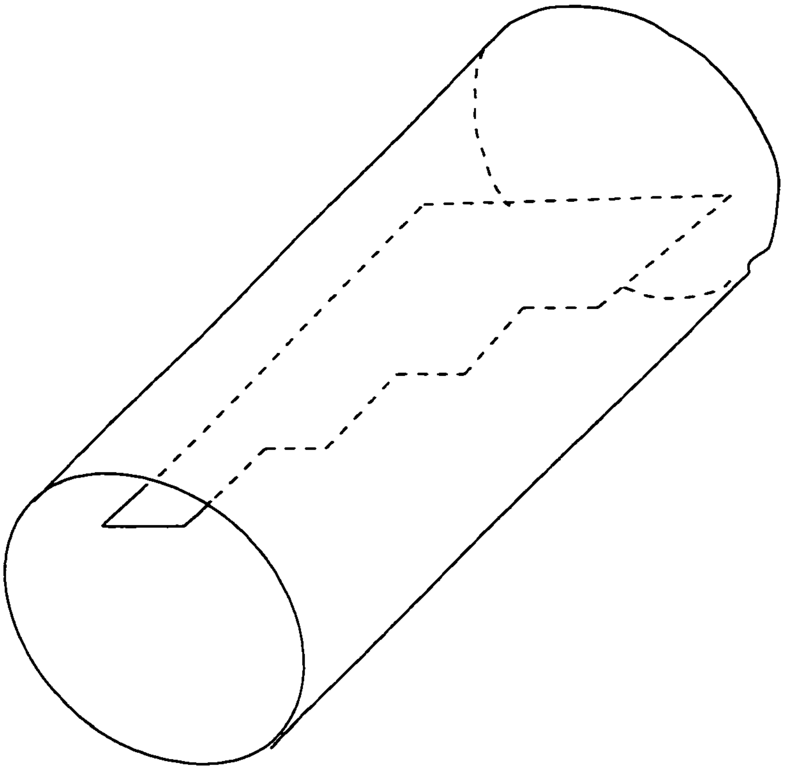

Figure 6.1: A septum polarizer

Irises of sectoral shape as shown in Figure 6.2(b,c) can be used to couple the orthogonal polarizations into circular waveguides in place of the offset rectangular iris (Figure 6.2(a)) presented in [45]. Such a shape (Figure 6.2(b,c)) avoids the mixed coordinate system required to compute the structure of Figure 6.2(a) and, besides, it is possible to fabricate them as easily. A wide range of similar waveguide component designs related to filters, multiplexers, transformers polarizers and orthomode transducers is possible as an extension to the approaches discussed in this work.

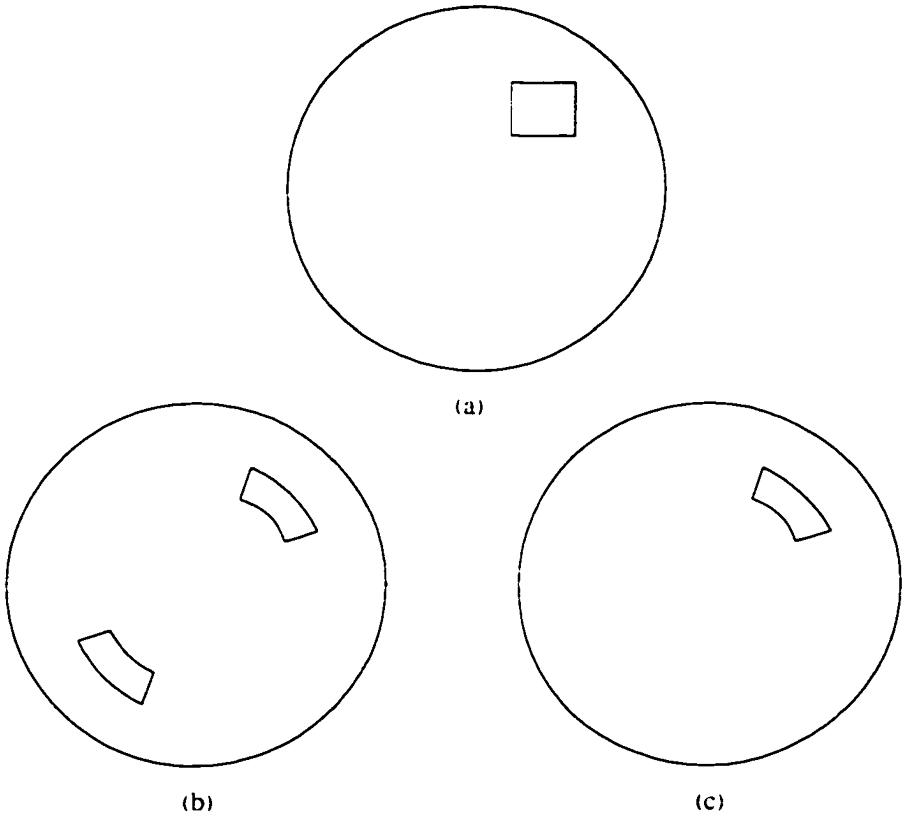

Figure 6.2: Irises for dual mode filters (a) Rectangular iris (b) and (c) Sectoral irises

Bibliography

[1] A. Wexler. "Solution of waveguide discontinuities by modal analysis." *IEEE Trans. Microwave Theory & Techniques.* Vol. 10. no. 9. pp. 508–517. Sept. 1967.

[2] R. C. Booton. in *Computational methods for electromagnetics and microwaves.* John Wiley & Sons. 1992.

[3] K. S. Yee. "Numerical solution of initital boundary value problems involving Maxwell's equations in isotropic media." *IEEE Trans. Antennas and Propagation.* Vol. 14. pp. 302–307. May 1966.

[4] W. J. R. Hoefer. "The transmission-line matrix method-theory and application." *IEEE Trans. Microwave Theory & Techniques.* Vol. 33. no. 10. pp. 883–893. Oct. 1985.

[5] H. Jin and R. Vahldieck. "The frequency-domain transmission line matrix method-a new concept." *IEEE Trans. Microwave Theory & Techniques.* Vol. 40. no. 12. pp. 2207–2218. Dec. 1992.

[6] R. F. Harrington. in *Field computation by moment methods.* NJ: IEEE Press. 1993.

[7] C. Eswarappa. G. I. Costache and W. J. R. Hoefer. "Finlines in rectangular and circular waveguide housings including substrate mounting and bending effects - finite element analysis." *IEEE Trans. Microwave Theory & Techniques.* Vol. 37. pp. 299–306. Feb. 1989.

[8] P. Daly. "Polar geometry waveguides by finite element methods." *IEEE Trans. Microwave Theory & Techniques*. Vol. 22. no. 3. pp. 202–209. Mar. 1974.

[9] B. M. Dillon and A. A. P. Gibson. "Triply-ridged circular waveguides." *Journal of Electromagnetic waves and Applications*. Vol. 9. no. 1/2. pp. 145–156. 1995.

[10] V. N. Kanellopoulous and J. P. Webb. "A complete E-plane analysis of waveguide junctions using the finite element method." *IEEE. Trans. Microwave Theory & Techniques*. Vol. 38. pp. 290–295. Mar. 1990.

[11] J. P. Webb and S. Parihar. "Finite-element analysis of H-plane rectangular waveguide problems." *IEE Proc.*. Vol. 130. pt. H. no. 2. pp. 91-94. Apr. 1986.

[12] K. Ise. K. Inoue and M. Koshiba. "Three dimensional finite-element solution of dielectric scattering obstacles in a rectangular waveguide." *IEEE Microwave Theory & Techniques*. Vol. 38. no. 9. pp. 1352-1359. Sept. 1990.

[13] K. Ishibashi and E. Sawado. "Three-dimensional analysis of electromagnetic fields in rectangular waveguides by the boundary integral equation method." *IEEE Microwave Theory & Techniques*. Vol. 38. no. 9. pp. 1300–1308. Sept. 1990.

[14] M. Koshiba and M. Suzuki. "Application of the boundary-element method to waveguide discontinuities." *IEEE Microwave Theory & Techniques*. Vol. 34. no. 2. pp. 301–307. Feb. 1986.

[15] T. Itoh and R. Mittra. "Spectral-domain approach for calculating the dispersion characteristics of microstrip lines." *IEEE Trans. Microwave Theory & Techniques*. Vol. 21. pp. 496–499. July 1973.

[16] R. Pregla and W. Pascher. "The Method of Lines." in *Chapter 6 in Numerical Techniques for Microwaves and MIllimeter-wave Passive structures*. T. Itoh., Ed. John Wiley & Sons. pp. 381–446. 1989.

[17] K. Wu and R. Vahldieck. "The method of lines applied to planar transmission lines in circular and elliptical waveguides." *IEEE Trans. Microwave Theory & Techniques*. Vol. 37. no. 12. pp. 1958–1963. Dec. 1989.

[18] M. Thorburn. A. Biswas and V. K. Tripathi. "Application of the method of lines to cylindrical inhomogeneous propagation structures." *Electronic Letters*. Vol. 26. pp. 170–171. Feb. 1990.

[19] R. Mittra and J. Pace. "A new technique for solving a class of boundary value probles." Antenna Laboratory. University of Illinois. Urbana. Rep. 72. 1963.

[20] N. Marcuvitz. in *Waveguide Handbook*. Peter Peregrinus Ltd. on behalf of IEE. 1986.

[21] G. Matthaei. L. Young and E. M. T. Jones. in *Microwave Filters. Impedance Matching Networs. and Coupling Structures.*. Dedham. MA.: Artech House. 1980.

[22] P. H. Masterman and P. J. B. Clarricoats. "Computer field-matching solution of waveguide discontinuities." *Proc. IEE*. Vol. 118. no. 1. pp. 51–63. Jan. 1971.

[23] H. Patzelt and F. Arndt. "Double-plane steps in rectangular waveguides and their applications for transformers. irises and filters." *IEEE Trans. Microwave Theory & Techniques*. Vol. 30. no. 5. pp. 771–776. May 1982.

[24] R. Safavi-Naini and R. H. MacPhie. "Scattering at rectangular-to-rectangular waveguide junctions." *IEEE Trans. Microwave Theory & Techniques*. Vol. 33. no. 11. pp. 2060–2063. Nov. 1982.

[25] R. Vahldieck. J. Bornemann. F. Arndt and D. Grauerholz. "Optimized waveguide E-plane metal insert filters for millimeter-wave applications." *IEEE Trans. Microwave Theory & Techniques*. Vol. 31. no. 1. pp. 65–69. Jan. 1983.

[26] F. Arndt. U. Tucholke and T. Wriedt. "Computer-optimized multisection transformers between rectangular waveguide of adjacent frequency bands".." *IEEE Trans. Microwave Theory & Techniques*. Vol.32. pp. 1479–1484. Nov. 1984.

[27] T. Ege and P. McAndrew. "Analysis of stepped septum polarizers." *Electronic Lett.*, Vol. 21, pp. 1166–1168, Nov 1985.

[28] U. Tucholke, F. Arndt and T. Wriedt. "Field theory design of square waveguide iris polarizers." *IEEE Trans. Microwave Theory & Techniques*, Vol. 34, no. 1, pp. 156–160, Jan. 1986.

[29] R. R. Mansour and R. H. Macphie. "An improved transmission matrix formulation of cascaded discontinuties and its application to E-plane circuits." *IEEE Trans. Microwave Theory & Techniques*, Vol. 34, no. 12, pp. 1490–1498, Dec. 1986.

[30] R. R. Mansour and R. H. MacPhie. "Scattering at an N-furcated parallel-plate waveguide junction." *IEEE Microwave Theory & Techniques*, Vol. 30, no. 11, pp. 2060–2063, Nov. 1982.

[31] J. Dittloff and F. Arndt. "Rigorous Field Theory Design of millimeter-wave E-plane integrated circuit multiplexers." *IEEE Trans. Microwave Theory & Techniques*, Vol. 37, no. 2, pp. 340–350, Feb. 1989.

[32] T. Sieverding and F. Arndt. "Field Theoretic CAD of open or aperture matched T-junction coupled rectangular waveguide structures." *IEEE Trans. Microwave Theory & Techniques*, Vol. 40, no. 2, pp. 353–362, Feb. 1982.

[33] R. Vahldieck. "Quasi-planar filters for millimeter-wave applications." *IEEE Trans. Microwave Theory & Techniques*, Vol. 37, no. 2, pp. 324–334, Feb. 1989.

[34] J. Bornemann, R. Vahldieck, F. Arndt and D. Grauerholz. "Optimized low-insertion-loss millimetre-wave fin-line and metal insert filters." *The Radio and Electronic Engineer*, Vol. 52, no. 11/12, pp. 513–521, Nov./Dec. 1982.

[35] A. S. Omar and K. F. Schuenemann. "The effect of complex modes at finline discontinuities." *IEEE Trans. Microwave Theory & Techniques*, Vol. 34, no. 12, pp. 1508–1514, Dec. 1986.

[36] T. S. Chu, T. Itoh and Y. C. Shih, "Comparative study of mode-matching formulations for microstrip discontinuity problems," *IEEE Trans. Microwave Theory & Techniques*, Vol. 33, no. 10, pp. 1018–1023, Oct. 1985.

[37] I. Wolff, "The waveguide model for the analysis of microstrip discontinuities," in *Chap. 7 in Numerical Techniques for Microwaves and Millimeter-wave Passive structures*, T. Itoh, Ed. John Wiley & Sons , pp. 447–495, 1989.

[38] J. Bornemann, "Rigorous field theory analysis of quasiplanar waveguides," *IEEE Proceedings*, Vol. 132, Pt. H., no. 1, pp. 1–6, Feb. 1985.

[39] R. Vahldieck, "Accurate hybrid-mode analysis of various finline configurations including multilayered dielectrics, finite metallization thickness, and substrate holding grooves," *IEEE Trans. Microwave Theory & Techniques*, Vol. 32, no. 11, pp. 1454–1460, Nov. 1984.

[40] G. Kowalski and R. Pregla, "Dispersion characteristics of shielded microstripts with finite thickness," *Arch. Elek. Ubertragung*, Vol. 25, pp. 93–196, April 1971.

[41] M. Thumm, A. Jacobs and M. S. Ayza, "Design of short high-power TE_{11}-HE_{11} mode converters in highly overmoded corrugated waveguides," *IEEE Microwave Theory & Techniques*, Vol. 39, no. 2, pp. 301–309, Feb. 1991.

[42] T. ul Haq, K. J. Webb and N. C. Gallagher, "TE_{11} to TM_{11} compact mode converter for circular waveguide," presented at IEEE MTT Symposium, pp. 1613-1615, May 1995.

[43] B. V. dela Filolie and R. Vahldieck, "Coaxial and circular waveguide bandpass filters using printed metal inserts," presented at IEEE MTT Symposium, pp. 905-908, 1992.

[44] M. Mongiardo and R. Sorrentino, "Efficient and versatile analysis of microwave structures by combined mode matching and finite difference methods," *IEEE Microwave and Guided Wave Letters*, Vol. 3, no. 8, pp. 241–243, Aug. 1993.

[45] R. Beyer and F. Arndt. "Efficient modal analysis of waveguide filters including the orthogonal coupling by an MM/FE method." *IEEE Microwave and Guided Wave Letters*. Vol. 5. no. 1. pp. 1–3. Jan. 1995.

[46] F. Alessandri. M. Monguiardo and R. Sorrentino. "Computer-aided design of beam forming networks for modern satellite antennas." *IEEE Trans. Microwave Theory & Techniques*. Vol. 40. no. 6. pp. 1117–1127. Jun. 1992.

[47] Y. C. Shih. "The Mode-Matching Method." in *Chapter 9 in Numerical Techniques for Microwaves and MIllimeter-wave Passive structures*. T. Itoh. Ed. John Wiley & Sons. pp. 592–621. 1989.

[48] R. E. Collin. in *Foundations for Microwave Engineering*. McGraw-Hill. Inc.. 1992.

[49] J. Bornemann and F. Arndt. "Modal-S-Matrix design of optimum stepped ridged and finned waveguide transformers." *IEEE Trans. Microwave Theory & Techniques*. Vol. 31. no. 1. pp. 561–567. June 1987.

[50] J. Bornemann and R. Vahldieck. "Characterization of a class of waveguide discontinuities using a modified TE_{mn}^{x} mode Approach." *IEEE Trans. Microwave Theory & Techniques*. Vol. 38. no. No. 12. pp. 1816–1822. Dec. 1990.

[51] V. A. Labay and J. Bornemann. "Matrix singular value decomposition for pole-free solutions of homogeneous matrix equations as applied to numerical modeling methods." *IEEE Microwave and Guided Wave Letters*. Vol. 2. no. 2. pp. 49–51. Feb. 1992.

[52] Y. Utsumi. "Variational analysis of ridged waveguide modes." *IEEE Trans. Microwave Theory & Techniques*. . pp. 111-120. Feb. 1985.

[53] F. Alessandri. P. Capece and R. Sorrentino. "Theory and experiment on rectangular coaxial line discontinuities and junctions." presented at IEEE MTT Symposium. pp. 259-262. 1990.

[54] S. K. Das and B. K. Sinha. "Numerical solution of higher order mode cut-off frequencies in symmetric TEM cells using Finite Element Method." *IEEE Trans. EMC*. Vol. 32. pp. 264–268. Nov. 1990.

[55] J. Zhang and J. Fu. "Higher-order mode cut-off frequencies in TEM cells calculated with TLM method." *IEEE Trans. EMC*. Vol. 30. pp. 563–567. Nov. 1988.

[56] I. Sreenivasiah and D. C. Chang. "A variational expression for the Scattering Matrix of double step discontinuity in a coaxial line and application to a TEM cell." *IEEE Trans. Microwave Theory & Techniques*. Vol. 31. pp. 380–384. May 1983.

[57] B. V. de la Filolie. "Field theory analysis of rectangular and circular waveguide discontinuities for filters multiplexers and matching networks." University of Victoria. Ph.D Thesis. 1992.

[58] R. F. Harrington. in *Time-Harmonic Electromagnetic Fields*. McGraw-Hill Book Co.. 1961.

[59] R. Behe and P. Brachat. "Compact duplexer-polarizer with semicircular waveguide." *IEEE Trans. Antennas & Propagation*. Vol. 39. pp. 1222–1224. Aug. 1991.

[60] D. A. AlMukhtar and J. E. Sitch. "Transmission-line matrix method with irregularly graded space." *IEE Proc.*. Vol 128. Pt. H. no. 6. pp. 299–305. Dec. 1981.

[61] S. J. Skinner and G. L. James. "Wide-band orthomode transducer." *IEEE Trans. Microwave Theory & Techniques*. Vol. 39. pp. 294–300. Feb. 1991.

[62] M. H. Chen. N. Tsandoulas and F. G. Willwerth. "Modal Characteristics of quadruple-ridged circular and square waveguides." *IEEE Trans. on Microwave Theory & Techniques*. Vol. 22. pp. 801–804. Aug. 1974.

[63] W. Sun and C. A. Balanis. "Analysis and design of quadruple-ridged waveguides." *IEEE Trans. Microwave Theory & Techniques*. Vol. 42. pp. 2201–2207. Dec 1994.

[64] A. Antoniou. in *Digital Filters. Design and Applications*. Second Edition. McGraw-Hill. 1993.

[65] G. F. Craven and C. K. Mok. "The design of evanescent mode filters for a prescribed insertion loss characteristi." *IEEE Trans. Microwave Theory & Techniques*. Vol. 19. no. No. 3. pp. 295–308. Mar 1971.

[66] Q. Zhang and T. Itoh. "Computer-aided design of evanescent-mode waveguide filter with nontouching E-plane fins." *IEEE Trans. Microwave Theory & Techniques*. Vol. 36. no. 2. pp. 259–262. Feb. 1988.

[67] J. Bornemann and F. Arndt. "Transverse resonance. standing wave. and resonator formulations of the ridge waveguide eigenvalue problem and its application to the design of E-plane finned waveguide filters." *IEEE Trans. Microwave Theory & Techniques*. Vol. 38. no. 8. pp. 404–412. Aug. 1990.

[68] V. A. Labay and J. Bornemann. "CAD of T-Septum waveguide evanescent-mode filters." *IEEE Microwave Theory & Tech.*. Vol. 41. no. 4. pp. 731-733. Apr. 1993.

[69] R. W. Scharstein and A. T. Adams. "Thick circular iris in a TE_{11} mode circular waveguide." *IEEE Transactions of Microwave Theory & Techniques.*. Vol. 36. no. 11. pp. 1529–1531. Nov. 1988.

[70] A. E. Williams and A. E. Atia. "Dual-Mode canonical waveguide filters." *IEEE Transactions on Microwave Theory & Techniques*. Vol. 25. no. No. 12. pp. 1021–1026. Dec. 1977.

[71] X. P. Liang. K. A. Zaki and A. E. Atia. "Dual mode coupling by square corner cut in resonators and filters." *IEEE. Trans. Microwave Theory & Techniques*. Vol. 41. pp. 2294–2302. Dec. 1992.

[72] J. Uher. J. Bornemann and U. Rosenberg. in *Waveguide Components for antenna feed systems: Theory and CAD.* Artech House Inc.. 1993.

[73] K. Mahadevan and S. Ghosh. "Accurate determination of the S-matrix of a circular waveguide polarizer module." presented at ANTEM Symposium. pp. 277-280. 1994.

[74] R. Levy. "The relationship between dual mode cavity cross-coupling and waveguide polarizers." *IEEE Microwave Theory & Techniques*. Vol. 43. no. 11. pp. 2614–2620. Nov. 1995.

[75] F. Arndt. W. Tucholke and T. Wriedt. "Design of wideband compact square waveguide polarizer." *Electronic Letters*. Vol. 21. pp. 74-75. June 1985.

[76] R. H. MacPhie and K-L. Wu. "Scattering at the junction of a rectangular waveguide and a larger circular waveguide." *IEEE Transactions on Microwave Theory & Techniques*. Vol. 43. no. 9. pp. 2041-2045. Sept. 1995.

[77] U. Papziner and F. Arndt. "Field theoretical computer-aided design of rectangular and circular iris coupled rectangular or circular waveguides cavity filters." *IEEE Microwave Theory & Techniques*. Vol. 41. no. 3. pp. 462–471. Mar. 1993.

[78] S. Ramo. J. R. Whinnery and T. V. Duzer. in *Fields and Waves in Communication Electronics*. John Wiley and Sons Inc.. 1965.

[79] M. Abramowitz and I. Stegun. in *Handbook of mathematical functions*. New York: Dover.

[80] I. S. Gradshteyn and I. M. Ryzhik. in *Table of Integrals. Series. and Products*. San Diego: Academic Press. 1980.

Appendix A

Field Components in Rectangular Waveguides

- Field Components of Transverse Magnetic Modes

$$E_x = \frac{1}{j\omega\epsilon}\frac{\partial^2\psi^e}{\partial x\partial y} \qquad H_x = \frac{\partial\psi^e}{\partial y} \tag{A.1}$$

$$E_y = \frac{1}{j\omega\epsilon}\frac{\partial^2\psi^e}{\partial y\partial z} \qquad H_y = -\frac{\partial\psi^e}{\partial x} \tag{A.2}$$

$$E_z = \frac{1}{j\omega\epsilon}\left(\frac{\partial^2}{\partial z^2} + k^2\right)\psi^e \qquad H_z = 0 \tag{A.3}$$

- Field Components of Transverse Electric Modes

$$E_x = -\frac{\partial\psi^h}{\partial y} \qquad H_x = \frac{1}{j\omega\mu}\frac{\partial^2\psi^h}{\partial x\partial z} \tag{A.4}$$

$$E_y = \frac{\partial\psi^h}{\partial x} \qquad H_y = \frac{1}{j\omega\mu}\frac{\partial^2\psi^h}{\partial y\partial z} \tag{A.5}$$

$$E_z = 0 \qquad H_z = \frac{1}{j\omega\mu}\left(\frac{\partial^2}{\partial z^2} + k^2\right)\psi^h \tag{A.6}$$

Appendix B

Alternative Matrix Inversion

An alternative technique for evaluation of generalized scattering matrix in a two port network with the coupling submatrices is presented here. The matrices V_{hh}, V_{ee} and V_{eh} are the coupling matrices from which the generalized S-matrix is obtained.

$$M = \begin{pmatrix} V_{hh} & 0 \\ V_{eh} & V_{ee} \end{pmatrix} \tag{B.1}$$

The submatrices of the generalized S-matrix are obtained as follows.

$$S_{11} = -W(I - MM^t) \tag{B.2}$$

$$S_{12} = 2WM \tag{B.3}$$

$$S_{21} = M^T[I + W(I - MM^T)] \tag{B.4}$$

$$S_{22} = I - 2M^T WM \tag{B.5}$$

where $W = (I + MM^T)^{-1}$

Appendix C

Generalized Scattering Matrix Technique

The generalized scattering matrix technique is used to combine the interaction of fundamental and higher order modes at cascaded discontinuities. The following equations are used to cascade the generalized S-matrices of two discontinuities shown in Figure C.1.

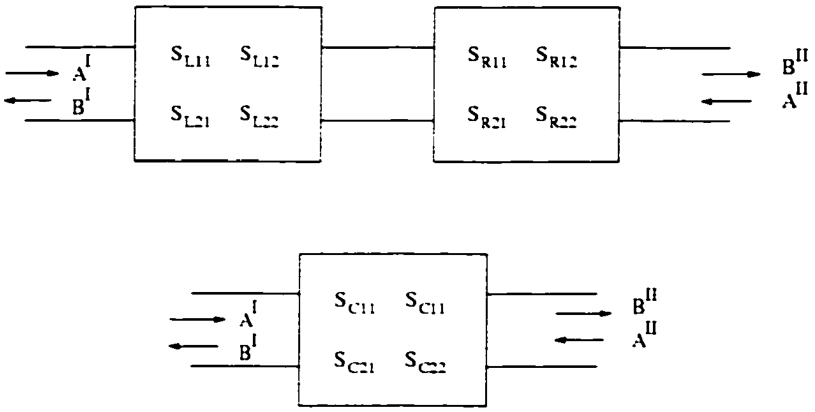

Figure C.1: Cascading two-port scattering matrices

$$S_{C11} = S_{L11} + S_{L12} S_{R11} W S_{L21} \tag{C.1}$$

$$S_{C12} = S_{L12}(I + S_{R11}W'S_{L22})S_{R12} \quad (C.2)$$

$$S_{C21} = S_{R21}W'S_{L21} \quad (C.3)$$

$$S_{C22} = S_{R22} + S_{R21}W'S_{L22}W'S_{R12} \quad (C.4)$$

where $W' = [I - S_{L22}S_{R11}]^{-1}$ and S_L and S_R are generalized scattering matrices as shown in Figure C.1.

For the discontinuity of finite length as shown in Figure C.2 the generalised S matrix is obtained as

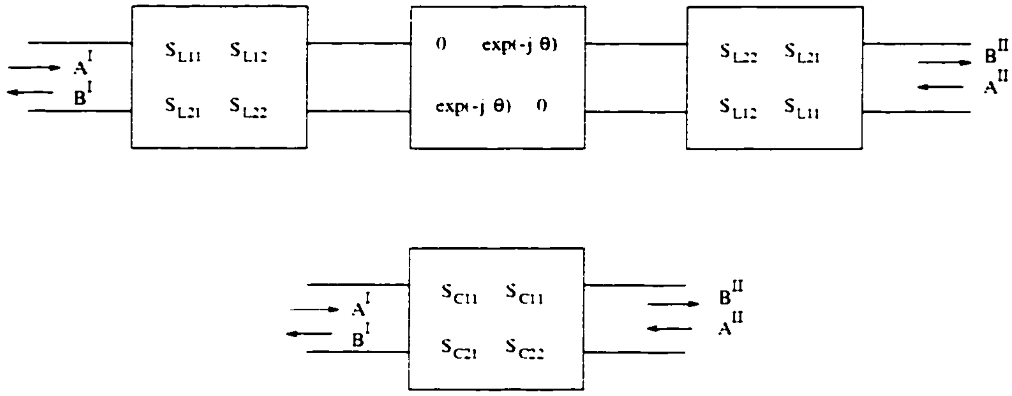

Figure C.2: Scattering matrix of a discontinuity of finite length

$$S_{C11} = S_{L11} + S_{L12}D[I - S_{L22}DS_{L22}D]^{-1}S_{L22}DS_{L21} \quad (C.5)$$

$$S_{C22} = S_{C11} \quad (C.6)$$

$$S_{C12} = S_{L12}D[I - S_{L22}DS_{L22}D]^{-1}S_{L21} \quad (C.7)$$

$$S_{C12} = S_{C21} \quad (C.8)$$

where D is the diagonal matrix containing the phase or attenuation (θ) relations of the propagating and evanescent modes between the discontinuity of finite length l.

$$D = Diag(e^{-jk_z l}) \tag{C.9}$$

where, at any frequency f, the propagation constants in the region of the finitely long guide is obtained from the cutoff frequency f_c of all the modes as:

$$jk_z = \begin{cases} jk\sqrt{1-\left(\frac{f_c}{f}\right)^2} & \text{when } f > f_c \\ k\sqrt{1-\left(\frac{f}{f_c}\right)^2} & \text{when } f < f_c \end{cases} \tag{C.10}$$

The generalised S matrix of a two port junction followed by the region of electrical length θ as shown in Figure C.3 is obtained as

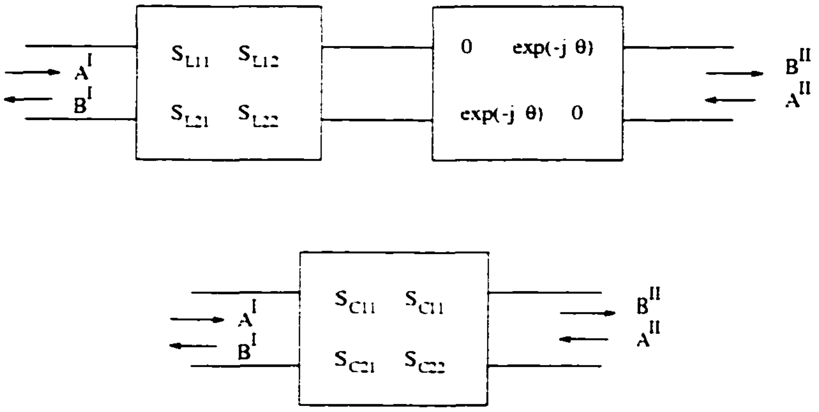

Figure C.3: Scattering matrix of a discontinuity followed by a guide of electrical length θ

$$S_{C11} = S_{L11} \tag{C.11}$$

$$S_{C12} = S_{L12}D \tag{C.12}$$

$$S_{C21} = DS_{L21} \tag{C.13}$$

$$S_{C22} = DS_{L22}D \tag{C.14}$$

where D is the same as in equation (C.9).

Appendix D

Field Components in Circular Waveguides

- Field Components of Transverse Magnetic Modes

$$H_\rho = \frac{1}{\rho}\frac{\partial \psi^e}{\partial \phi} \qquad E_\rho = \frac{1}{j\omega\epsilon}\frac{\partial^2 \psi^e}{\partial \rho \partial z} \tag{D.1}$$

$$H_\phi = -\frac{\partial \psi^e}{\partial \rho} \qquad E_\phi = \frac{1}{j\omega\epsilon\rho}\frac{\partial \psi^e}{\partial \phi \partial z} \tag{D.2}$$

$$H_z = 0 \qquad E_z = \frac{1}{j\omega\epsilon}\left(\frac{\partial^2}{\partial z^2} + k^2\right)\psi^e \tag{D.3}$$

- Field Components of Transverse Electric Modes

$$E_\rho = \frac{1}{\rho}\frac{\partial \psi^h}{\partial \phi} \qquad H_\rho = \frac{1}{j\omega\mu}\frac{\partial^2 \psi^h}{\partial \rho \partial z} \tag{D.4}$$

$$E_\phi = -\frac{\partial \psi^h}{\partial \rho} \qquad H_\phi = \frac{1}{j\omega\mu\rho}\frac{\partial \psi^h}{\partial \phi \partial z} \tag{D.5}$$

$$E_z = 0 \qquad H_z = \frac{1}{j\omega\mu}\left(\frac{\partial^2}{\partial z^2} + k^2\right)\psi^h \tag{D.6}$$

Appendix E

Useful Bessel Function Relations

Bessel equation:

The Bessel functions are solutions of the differential equation:

$$\frac{d^2P}{d\rho^2} + \frac{1}{\rho}\frac{dP}{d\rho} + \left(1 - \frac{n^2}{\rho^2}\right) = 0 \tag{E.1}$$

The solutions to the above differential equation are convergent power series. These solutions are called the Bessel functions of the first kind J_n and the Bessel functions of the second kind N_n, where n is the order. The value of n can be an integer, real or a complex number. But, the value of n encountered in this work are either an integer or a real number. Some of the useful differentials and integrals of these functions for real or integral n is listed below. The function $B_n(\rho) = AJ_n(\rho) + BN_n(\rho)$. The $B_n(\rho)$ could also be a sum of Hankel functions of the first and second kind which are written as:

$$\begin{aligned} H_n^{(1)}(\alpha\rho) &= J_n(\alpha\rho) + jN_n(\alpha\rho) && \text{(E.2)} \\ H_n^{(2)}(\alpha\rho) &= J_n(\alpha\rho) - jN_n(\alpha\rho) && \text{(E.3)} \end{aligned}$$

The negative and positive order of the Hankel functions are related by:

$$H_{-n}^{(1)}(\alpha\rho) = \epsilon^{j\pi n} H_n^{(1)}(\alpha\rho) \tag{E.4}$$

$$H^{(2)}_{-n}(\alpha\rho) = \epsilon^{-j\pi n} H^{(2)}_{n}(\alpha\rho) \tag{E.5}$$

The relation between the negative and positive orders in the Bessel functions of the first and second kind can be derived from the equations (E.4) and (E.5). The differentials and integrals given below can be found in [78.79.80]

Differentials in Bessel functions:

$$B_0'(\rho) = -B_1(\rho) \tag{E.6}$$

$$B_{(-n)}'(\rho) = (-1)^n B_n(\rho) \tag{E.7}$$

$$n B_n(\rho) = \frac{\rho}{2}(B_{n-1}(\rho) + B_{n+1}(\rho)) \tag{E.8}$$

$$\frac{dB_n(\alpha\rho)}{d\rho} = \frac{\alpha}{2}[B_{n-1}(\alpha\rho) + B_{n+1}(\alpha\rho)] \tag{E.9}$$

$$\frac{dB_0(\alpha\rho)}{d\rho} = -\alpha B_1(\alpha\rho) \tag{E.10}$$

$$\rho\frac{dB_n(\alpha\rho)}{d\rho} = \alpha\rho B_{n-1}(\alpha\rho) - n B_n(\alpha\rho) \tag{E.11}$$

$$\rho\frac{dB_n(\alpha\rho)}{d\rho} = n B_n(\alpha\rho) + \alpha\rho B_{n+1}(\alpha\rho) \tag{E.12}$$

$$\frac{d}{d\rho}(\rho^n B_n(\rho)) = x^n B_{n-1}(\rho) \tag{E.13}$$

$$\frac{d}{d\rho}(\rho^{-n} B_n(\rho)) = -x^{-n} B_{n+1}(\rho) \tag{E.14}$$

Integrals in Bessel functions:

$$\int \rho^2 B_0(\rho) d\rho = \rho^2 B_1(\rho) + \rho B_0(\rho) - \int B_0(\rho) d\rho \tag{E.15}$$

$$\int B_1(\rho) d\rho = -B_1(\rho) \tag{E.16}$$

$$\int \rho B_1(\rho)d\rho = -\rho B_0(\rho) + \int B_0(\rho)d\rho \tag{E.17}$$

$$\int \rho^n B_{n-1}(\rho)d\rho = \rho^n B_n(\rho) \tag{E.18}$$

$$\begin{aligned}\int \rho B_n(\alpha\rho)B_n(\beta\rho)d\rho &= \frac{\rho}{\beta^2-\alpha^2}(\alpha B_n(\beta\rho)B_n'(\alpha\rho) - \beta B_n(\alpha\rho)B_n'(\beta\rho)) && \text{(E.19)}\\ &= \frac{\rho}{\alpha^2-\beta^2}(\beta B_n(\alpha\rho)B_{n-1}(\beta\rho) - \alpha B_{n-1}(\alpha\rho)B_n(\beta\rho)) && \text{(E.20)}\\ &= \frac{\rho}{\beta^2-\alpha^2}(\beta B_n(\alpha\rho)B_{n+1}(\beta\rho)) - \alpha B_{n+1}(\alpha\rho)B_n(\beta\rho)) && \text{(E.21)}\end{aligned}$$

$$\begin{aligned}\int \rho B_n^2(\alpha\rho)d\rho &= \frac{\rho^2}{2}(B_n'(\alpha\rho))^2 + \frac{\rho^2}{2}(1 - \frac{n^2}{\alpha^2\rho^2})B_n^2(\alpha\rho) && \text{(E.22)}\\ &= \frac{\rho^2}{2}\left(B_n^2(\alpha\rho) + B_{n-1}(\alpha\rho)B_{n+1}(\alpha\rho)\right) && \text{(E.23)}\end{aligned}$$

Recurrence Relation:

Using this relation it is possible to obtain the values for Bessel functions of any order when the values of the functions for any two orders, differing from the first by integers are known.

$$\frac{2n}{\rho}B_n\rho = B_{n+1}(\rho) + B_{n-1}(\rho) \tag{E.24}$$

Appendix F

Coupling Integrals of Circular to Single Ridged Circular Waveguide Discontinuity

The coupling integrals of matrices of equation (5.14) and (5.15) are given below:

$$L_{\epsilon\epsilon}^{cc}(x,y) = (\sum_{n=0}^{N1c} Term_9 + \sum_{m=1,3}^{N2c} Term_{10})\sqrt{\frac{k_z^{IIec}(x)}{k_z^{Iec}(y)}} \tag{F.1}$$

$$\begin{aligned} Term_9 \;=\; & P_{q,p}^{(Iec)} P_{n,r}^{(IIec)} \\ & \cdot \left(\int_0^a \frac{nq}{\rho} J_q(k_{c_{q,p}}^{Iec}\rho) J_n(k_{c_r}^{IIec}\rho) d\rho \int_\alpha^{2\pi+\alpha} \sin q\phi \sin n(\phi - \alpha) d\phi \right. \\ & \left. + J_q'(k_{c_{q,p}}^{Iec}\rho) J_n'(k_{c_r}^{IIec}\rho)\rho d\rho \int_\alpha^{2\pi+\alpha} \cos q\phi \cos n(\phi - \alpha) d\phi \right) \end{aligned} \tag{F.2}$$

$$\begin{aligned} Term_{10} \;=\; & P_{q,p}^{Iec} P_{m,r}^{IIec} \int_a^b -\frac{lq}{\rho^2} J_q(k_{c_{q,p}}^{Iec}\rho)[J_l(k_{c_r}^{IIec}\rho) N_l(k_{c_r}^{IIec}b) \\ & - J_l(k_{c_r}^{IIec}b) N_l(k_{c_r}^{IIec}\rho)]\rho d\rho \int_{\alpha+\theta}^{2\pi+\alpha-\theta} \sin q\phi \cos l(\phi - \alpha - \theta) d\phi \end{aligned}$$

$$+P_{q,p}^{(Iec)}P_{m,r}^{(IIec)}\int_a^b J_q'(k_{c_{q,p}}^{Iec}\rho)[J_l'(k_{c_r}^{IIec}\rho)N_l(k_{c_r}^{IIec}b)$$

$$-J_l'(k_{c_r}^{IIec}b)N_l(k_{c_r}^{IIec}\rho)]\rho d\rho\int_{\alpha+\theta}^{2\pi+\alpha-\theta}\cos q\phi\sin l(\phi-\alpha-\theta)d\phi \quad \text{(F.3)}$$

where $l=\frac{m\pi}{2(\pi-\theta)}$

$$L_{ee}^{ss}(x,y)=(\sum_{n=1}^{N1s}Term_{11}+\sum_{m=1}^{N2s}Term_{12})\sqrt{\frac{k_z^{IIes}(x)}{k_z^{Ies}(y)}} \quad \text{(F.4)}$$

$$\begin{aligned}Term_{11} &= P_{q,p}^{(Ies)}P_{n,r}^{(IIes)}\\ &\cdot\Bigg(\int_0^a\frac{nq}{\rho}J_q(k_{c_{q,p}}^{Ies}\rho)J_n(k_{c_r}^{IIes}\rho)d\rho\int_\alpha^{2\pi+\alpha}\cos q\phi\cos n(\phi-\alpha)d\phi\\ &+J_q'(k_{c_{q,p}}^{Ies}\rho)J_n'(k_{c_r}^{IIes}\rho)\rho d\rho\int_\alpha^{2\pi+\alpha}\sin q\phi\sin n(\phi-\alpha)d\phi\Bigg) \quad \text{(F.5)}\end{aligned}$$

$$\begin{aligned}Term_{12} &= P_{q,p}^{Ies}P_{m,r}^{IIes}\int_a^b\frac{lq}{\rho^2}J_q(k_{c_{q,p}}^{Ies}\rho)[J_l(k_{c_r}^{IIes}\rho)N_l(k_{c_r}^{IIes}b)\\ &-J_l(k_{c_r}^{IIes}b)N_l(k_{c_r}^{IIes}\rho)]\rho d\rho\int_{\alpha+\theta}^{2\pi+\alpha-\theta}\cos q\phi\cos l(\phi-\alpha-\theta)d\phi\\ &+P_{q,p}^{(Ies)}P_{m,r}^{(IIes)}\int_a^b J_q'(k_{c_{q,p}}^{Ies}\rho)[J_l'(k_{c_r}^{IIes}\rho)N_l(k_{c_r}^{IIes}b)\\ &-J_l'(k_{c_r}^{IIes}b)N_l(k_{c_r}^{IIes}\rho)]\rho d\rho\int_{\alpha+\theta}^{2\pi+\alpha-\theta}\sin q\phi\sin l(\phi-\alpha-\theta)d\phi \quad \text{(F.6)}\end{aligned}$$

where $l=\frac{m\pi}{(\pi-\theta)}$

$$L_{ee}^{cs}(x,y)=(\sum_{n=1}^{N1s}Term_{13}+\sum_{m=1}^{N2s}Term_{14})\sqrt{\frac{k_z^{IIes}(x)}{k_z^{Iec}(y)}} \quad \text{(F.7)}$$

$$\begin{aligned} Term_{13} \;=\;& P_{q,p}^{(Iec)} P_{n,r}^{(IIes)} \\ & \cdot \left(\int_0^a \frac{nq}{\rho} J_q(k_{z_{q,p}}^{Iec}\rho) J_n(k_{z_r}^{IIes}\rho) d\rho \int_\alpha^{2\pi+\alpha} -\sin q\phi \cos n(\phi-\alpha) d\phi \right. \\ & \left. + J_q'(k_{z_{q,p}}^{Iec}\rho) J_n'(k_{z_r}^{IIes}\rho)\rho d\rho \int_\alpha^{2\pi+\alpha} \cos q\phi \sin n(\phi-\alpha) d\phi \right) \qquad \text{(F.8)} \end{aligned}$$

$$\begin{aligned} Term_{14} \;=\;& P_{q,p}^{Iec} P_{m,r}^{IIes} \int_a^b \frac{lq}{\rho^2} J_q(k_{z_{q,p}}^{Iec}\rho)[J_l(k_{z_r}^{IIes}\rho) N_l(k_{z_r}^{IIes}b) \\ & - J_l(k_{z_r}^{IIes}b) N_l(k_{z_r}^{IIes}\rho)]\rho d\rho \int_{\alpha+\theta}^{2\pi+\alpha-\theta} -\sin q\phi \cos l(\phi-\alpha-\theta) d\phi \\ & + P_{q,p}^{(Iec)} P_{m,r}^{(IIes)} \int_a^b J_q'(k_{z_{q,p}}^{Iec}\rho)[J_l'(k_{z_r}^{IIes}\rho) N_l(k_{z_r}^{IIes}b) \\ & - J_l'(k_{z_r}^{IIes}b) N_l(k_{z_r}^{IIes}\rho)]\rho d\rho \int_{\alpha+\theta}^{2\pi+\alpha-\theta} \cos q\phi \sin l(\phi-\alpha-\theta) d\phi \qquad \text{(F.9)} \end{aligned}$$

where $l = \frac{m\pi}{(\pi-\theta)}$

$$L_{ee}^{sc}(x,y) = \left(\sum_{n=0}^{N1c} Term_{15} + \sum_{m=1,3}^{N2c} Term_{16}\right) \sqrt{\frac{k_z^{IIec}(x)}{k_z^{Ies}(y)}} \qquad \text{(F.10)}$$

$$\begin{aligned} Term_{15} \;=\;& P_{q,p}^{(Ies)} P_{n,r}^{(IIec)} \\ & \cdot \left(\int_0^a \frac{nq}{\rho} J_q(k_{z_{q,p}}^{Ies}\rho) J_n(k_{z_r}^{IIes}\rho) d\rho \int_\alpha^{2\pi+\alpha} -\cos q\phi \sin n(\phi-\alpha) d\phi \right. \\ & \left. + J_q'(k_{z_{q,p}}^{Ies}\rho) J_n'(k_{z_r}^{IIec}\rho)\rho d\rho \int_\alpha^{2\pi+\alpha} \sin q\phi \cos n(\phi-\alpha) d\phi \right) \qquad \text{(F.11)} \end{aligned}$$

$$\begin{aligned} Term_{16} \;=\; & P_{q,p}^{Ies} P_{m,r}^{IIec} \int_a^b \frac{lq}{\rho^2} J_q(k_{c_{q,p}}^{Ies}\rho)[J_l(k_{c_r}^{IIec}\rho) N_l(k_{c_r}^{IIec}b) \\ & - J_l(k_{c_r}^{IIec}b) N_l(k_{c_r}^{IIec}\rho)]\rho d\rho \int_{\alpha+\theta}^{2\pi+\alpha-\theta} \cos q\phi \cos l(\phi-\alpha-\theta) d\phi \\ & + P_{q,p}^{(Ies)} P_{m,r}^{(IIec)} \int_a^b J_q'(k_{c_{q,p}}^{Ies}\rho)[J_l'(k_{c_r}^{IIec}\rho) N_l(k_{c_r}^{IIec}b) \\ & - J_l'(k_{c_r}^{IIec}b) N_l(k_{c_r}^{IIec}\rho)]\rho d\rho \int_{\alpha+\theta}^{2\pi+\alpha-\theta} \sin q\phi \sin l(\phi-\alpha-\theta) d\phi \quad (\mathrm{F.12}) \end{aligned}$$

where $l = \frac{m\pi}{2(\pi-\theta)}$

$$L_{eh}^{ss}(x,y) = (\sum_{n=0}^{N1s} Term_{17} + \sum_{m=0}^{N2s} Term_{18}) \frac{k_o}{\sqrt{k_z^{Ies}(x) k_z^{IIhs}(y)}} \qquad (\mathrm{F.13})$$

$$\begin{aligned} Term_{17} \;=\; & P_{q,p}^{(Ies)} P_{n,r}^{(IIhs)} \\ & \cdot \Big(\int_0^a n J_q'(k_{c_{q,p}}^{Ies}\rho) J_n(k_{c_r}^{IIhs}\rho) d\rho \int_\alpha^{2\pi+\alpha} -\sin q\phi \sin n(\phi-\alpha) d\phi \\ & + q J_q(k_{c_{q,p}}^{Ies}\rho) J_n'(k_{c_r}^{IIhs}\rho) d\rho \int_\alpha^{2\pi+\alpha} -\cos q\phi \cos n(\phi-\alpha) d\phi \Big) \quad (\mathrm{F.14}) \end{aligned}$$

$$\begin{aligned} Term_{18} \;=\; & P_{q,p}^{Ies} P_{m,r}^{IIhs} \int_a^b -l J_q'(k_{c_{q,p}}^{Ies}\rho)[J_l(k_{c_r}^{IIhs}\rho) N_l'(k_{c_r}^{IIhs}b) \\ & - J_l'(k_{c_r}^{IIhs}b) N_l(k_{c_r}^{IIhs}\rho)] d\rho \int_{\alpha+\theta}^{2\pi+\alpha-\theta} \sin q\phi \sin l(\phi-\alpha-\theta) d\phi \\ & - P_{q,p}^{(Ies)} P_{m,r}^{(IIhs)} \int_a^b q J_q(k_{c_{q,p}}^{Ies}\rho)[J_l'(k_{c_r}^{IIhs}\rho) N_l'(k_{c_r}^{IIhs}b) \\ & - J_l'(k_{c_r}^{IIhs}b) N_l'(k_{c_r}^{IIhs}\rho)] d\rho \int_{\alpha+\theta}^{2\pi+\alpha-\theta} \cos q\phi \cos l(\phi-\alpha-\theta) d\phi \quad (\mathrm{F.15}) \end{aligned}$$

where $l = \frac{m\pi}{(\pi-\theta)}$

$$L_{eh}^{cc}(x,y) = \left(\sum_{n=1}^{N1c} Term_{19} + \sum_{m=1,3}^{N2c} Term_{20}\right)\frac{k_o}{\sqrt{k_z^{Iec}(x)k_z^{IIhc}(y)}} \qquad \text{(F.16)}$$

$$\begin{aligned} Term_{19} &= P_{q,p}^{(Iec)}P_{n,r}^{(IIhc)} \\ &\cdot\left(\int_0^a nJ_q'(k_{c_{q,p}}^{Iec}\rho)J_n(k_{c_r}^{IIhc}\rho)d\rho\int_\alpha^{2\pi+\alpha}\cos qo\cos n(o-\alpha)do\right. \\ &\left.+\,qJ_q(k_{c_{q,p}}^{Iec}\rho)J_n'(k_{c_r}^{IIhc}\rho)d\rho\int_\alpha^{2\pi+\alpha}\sin qo\sin n(o-\alpha)do\right) \qquad \text{(F.17)} \end{aligned}$$

$$\begin{aligned} Term_{20} &= P_{q,p}^{Iec}P_{m,r}^{IIhc}\int_a^b lJ_q'(k_{c_{q,p}}^{Iec}\rho)[J_l(k_{c_r}^{IIhc}\rho)N_l'(k_{c_r}^{IIhc}b) \\ &-J_l'(k_{c_r}^{IIhc}b)N_l(k_{c_r}^{IIhc}\rho)]d\rho\int_{\alpha+\theta}^{2\pi+\alpha-\theta}\cos qo\sin l(o-\alpha-\theta)do \\ &+P_{q,p}^{(Iec)}P_{m,r}^{(IIhc)}\int_a^b qJ_q(k_{c_{q,p}}^{Iec}\rho)[J_l'(k_{c_r}^{IIhc}\rho)N_l'(k_{c_r}^{IIhc}b) \\ &-J_l'(k_{c_r}^{IIhc}b)N_l'(k_{c_r}^{IIhc}\rho)]d\rho\int_{\alpha+\theta}^{2\pi+\alpha-\theta}\sin qo\cos l(o-\alpha-\theta)do \qquad \text{(F.18)} \end{aligned}$$

where $l = \frac{m\pi}{2(\pi-\theta)}$

$$L_{eh}^{sc}(x,y) = \left(\sum_{n=1}^{N1c} Term_{21} + \sum_{m=1,3}^{N2c} Term_{22}\right)\frac{k_o}{\sqrt{k_z^{Ies}(x)k_z^{IIhc}(y)}} \qquad \text{(F.19)}$$

$$\begin{aligned} Term_{21} &= P_{q,p}^{(Ies)}P_{n,r}^{(IIhc)} \\ &\cdot\left(\int_0^a nJ_q'(k_{c_{q,p}}^{Ies}\rho)J_n(k_{c_r}^{IIhc}\rho)d\rho\int_\alpha^{2\pi+\alpha}\sin qo\sin n(o-\alpha)do\right. \\ &\left.+\,qJ_q(k_{c_{q,p}}^{Ies}\rho)J_n'(k_{c_r}^{IIhc}\rho)d\rho\int_\alpha^{2\pi+\alpha}\cos qo\cos n(o-\alpha)do\right) \qquad \text{(F.20)} \end{aligned}$$

$$\begin{aligned}
Term_{22} &= P^{Ies}_{q,p}P^{IIhc}_{m,r}\int_a^b lJ'_q(k^{Ies}_{z_{q,p}}\rho)[J_l(k^{IIhc}_{z_r}\rho)N'_l(k^{IIhc}_{z_r}b) \\
&\quad +J'_l(k^{IIhc}_{z_r}b)N_l(k^{IIhc}_{z_r}\rho)]d\rho\int_{\alpha+\theta}^{2\pi+\alpha-\theta}\sin q\phi\sin l(\phi-\alpha-\theta)d\phi \\
&\quad +P^{(Ies)}_{q,p}P^{(IIhc)}_{m,r}\int_a^b qJ_q(k^{Ies}_{z_{q,p}}\rho)[J'_l(k^{IIhc}_{z_r}\rho)N'_l(k^{IIhc}_{z_r}b) \\
&\quad J'_l(k^{IIhc}_{z_r}b)N'_l(k^{IIhc}_{z_r}\rho)]d\rho\int_{\alpha+\theta}^{2\pi+\alpha-\theta}cosq\phi\cos l(\phi-\alpha-\theta)d\phi \qquad (F.21)
\end{aligned}$$

where $l=\frac{m\pi}{2(\pi-\theta)}$

$$L^{es}_{eh}(x,y)=(\sum_{n=0}^{N1s}Term_{23}+\sum_{m=0}^{N2s}Term_{24})\frac{k_o}{\sqrt{k^{Iec}_z(x)k^{IIhs}_z(y)}} \qquad (F.22)$$

$$\begin{aligned}
Term_{23} &= P^{(Iec)}_{q,p}P^{(IIhs)}_{n,r} \\
&\quad \cdot\Big(\int_0^a nJ'_q(k^{Iec}_{z_{q,p}}\rho)J_n(k^{IIhs}_{z_r}\rho)d\rho\int_\alpha^{2\pi+\alpha}\sin q\phi\sin n(\phi-\alpha)d\phi \\
&\quad +qJ_q(k^{Iec}_{z_{q,p}}\rho)J'_n(k^{IIhs}_{z_r}\rho)d\rho\int_\alpha^{2\pi+\alpha}\cos q\phi\cos n(\phi-\alpha)d\phi\Big) \qquad (F.23)
\end{aligned}$$

$$\begin{aligned}
Term_{24} &= P^{Iec}_{q,p}P^{IIhs}_{m,r}\int_a^b lJ'_q(k^{Iec}_{z_{q,p}}\rho)[J_l(k^{IIhs}_{z_r}\rho)N'_l(k^{IIhs}_{z_r}b) \\
&\quad J'_l(k^{IIhs}_{z_r}b)N_l(k^{IIhs}_{z_r}\rho)]d\rho\int_{\alpha+\theta}^{2\pi+\alpha-\theta}\cos q\phi\sin l(\phi-\alpha-\theta)d\phi \\
&\quad +P^{(Iec)}_{q,p}P^{(IIhs)}_{m,r}\int_a^b qJ_q(k^{Iec}_{z_{q,p}}\rho)[J'_l(k^{IIhs}_{z_r}\rho)N'_l(k^{IIhs}_{z_r}b) \\
&\quad -J'_l(k^{IIhs}_{z_r}b)N'_l(k^{IIhs}_{z_r}\rho)]d\rho\int_{\alpha+\theta}^{2\pi+\alpha-\theta}\sin q\phi\cos l(\phi-\alpha-\theta)d\phi \qquad (F.24)
\end{aligned}$$

where $l=\frac{m\pi}{(\pi-\theta)}$

Appendix G

Coupling Integrals of Circular to Double Ridged Circular Waveguide

The nomenclatures used in the following equations have been discussed in Chapter 5 already. The coupling integrals of the matrix elements of V_{hh} for a discontinuity from a circular to a double ridged circular waveguide are as follows:

$$L_{hh}^{cc}(x,y) = (\sum_{n=1}^{N1c} Term_1 + \sum_{m=0}^{N2c} Term_2)\sqrt{\frac{k_z^{Ihc}(x)}{k_z^{IIhc}(y)}} \tag{G.1}$$

$$\begin{aligned} Term_1 \quad = \quad & P_{q,p}^{Ihc} P_{n,r}^{IIhc} \\ & \cdot \left(\int_0^a \frac{nq}{\rho} J_q(k_{c_{q,p}}^{Ihc}\rho) J_n(k_{c_r}^{IIhc}\rho) d\rho \int_\alpha^{2\pi+\alpha} \cos q\phi \cos n(\phi-\alpha) d\phi \right. \\ & \left. + J_q'(k_{c_{q,p}}^{Ihc}\rho) J_n'(k_{c_r}^{IIhc}\rho)\rho d\rho \int_\alpha^{2\pi+\alpha} \sin q\phi \sin n(\phi-\alpha) d\phi \right) \end{aligned} \tag{G.2}$$

$$Term_2 \quad = \quad P_{q,p}^{Ihc} P_{m,r}^{IIhc} \int_a^b -\frac{lq}{\rho^2} J_q(k_{c_{q,p}}^{Ihc}\rho)[J_l(k_{c_r}^{IIhc}\rho) N_l'(k_{c_r}^{IIhc}b)$$

$$-J_l'(k_{c_r}^{IIhc}b)N_l(k_{c_r}^{IIhc}\rho)]\rho d\rho \cdot 2\int_{\alpha+\theta}^{\pi+\alpha-\theta}\cos q\phi \sin l(\phi-\alpha-\theta)d\phi$$

$$+P_{q,p}^{(Ihc)}P_{m,r}^{(IIhc)}\int_a^b J_q'(k_{c_{q,p}}^{Ihc}\rho)[J_l'(k_{c_r}^{IIhc}\rho)N_l'(k_{c_r}^{IIhc}b)$$

$$-J_l'(k_{c_r}^{IIhc}b)N_l'(k_{c_r}^{IIhc}\rho)]\rho d\rho \cdot 2\int_{\alpha+\theta}^{\pi+\alpha-\theta}\sin q\phi \cos l(\phi-\alpha-\theta)d\phi \tag{G.3}$$

where $l = \frac{m\pi}{(\pi-2\theta)}$

$$L_{hh}^{ss}(x,y) = (\sum_{n=0}^{N1s} Term_3 + \sum_{m=0}^{N2s} Term_4)\sqrt{\frac{k_z^{Ihs}(x)}{k_z^{IIhs}(y)}} \tag{G.4}$$

$$\begin{aligned} Term_3 \;=\;& P_{q,p}^{(Ihs)}P_{n,r}^{(IIhs)} \\ & \cdot\left(\int_0^a \frac{nq}{\rho}J_q(k_{c_{q,p}}^{Ihs}\rho)J_n(k_{c_r}^{IIhs}\rho)d\rho\int_\alpha^{2\pi+\alpha}\sin q\phi \sin n(\phi-\alpha)d\phi\right. \\ & \left.+\;J_q'(k_{c_{q,p}}^{Ihs}\rho)J_n'(k_{c_r}^{IIhs}\rho)\rho d\rho\int_\alpha^{2\pi+\alpha}\cos q\phi\cos n(\phi-\alpha)d\phi\right) \end{aligned} \tag{G.5}$$

$$\begin{aligned} Term_4 \;=\;& P_{q,p}^{Ihs}P_{m,r}^{IIhs}\int_a^b \frac{lq}{\rho^2}J_q(k_{c_{q,p}}^{Ihs}\rho)[J_l(k_{c_r}^{IIhs}\rho)N_l'(k_{c_r}^{IIhs}b) \\ & -J_l'(k_{c_r}^{IIhs}b)N_l(k_{c_r}^{IIhs}\rho)]\rho d\rho\cdot 2\int_{\alpha+\theta}^{\pi+\alpha-\theta}\sin q\phi\sin l(\phi-\alpha-\theta)d\phi \\ & +P_{q,p}^{(Ihs)}P_{m,r}^{(IIhs)}\int_a^b J_q'(k_{c_{q,p}}^{Ihs}\rho)[J_l'(k_{c_r}^{IIhs}\rho)N_l'(k_{c_r}^{IIhs}b) \\ & -J_l'(k_{c_r}^{IIhs}b)N_l'(k_{c_r}^{IIhs}\rho)]\rho d\rho\cdot 2\int_{\alpha+\theta}^{\pi+\alpha-\theta}\cos q\phi\cos l(\phi-\theta)d\phi \end{aligned} \tag{G.6}$$

where $l = \frac{m\pi}{(\pi-2\theta)}$

$$L_{hh}^{cs}(x,y) = (\sum_{n=0}^{N1s} Term_5 + \sum_{m=0}^{N2s} Term_6)\sqrt{\frac{k_z^{Ihc}(x)}{k_z^{IIhs}(y)}} \tag{G.7}$$

$$\begin{aligned} Term_5 = \; & P_{q,p}^{(Ihc)} P_{n,r}^{(IIhs)} \\ & \cdot \left(\int_0^a \frac{nq}{\rho} J_q(k_{z_{q,p}}^{Ihc}\rho) J_n(k_{z_r}^{IIhs}\rho) d\rho \int_\alpha^{2\pi+\alpha} -\cos q o \sin n(o-\alpha) do \right. \\ & \left. + J_q'(k_{z_{q,p}}^{Ihc}\rho) J_n'(k_{z_r}^{IIhs}\rho)\rho d\rho \int_\alpha^{2\pi+\alpha} \sin q o \cos n(o-\alpha) do \right) \end{aligned} \tag{G.8}$$

$$\begin{aligned} Term_6 = \; & P_{q,p}^{Ihc} P_{m,r}^{IIhs} \int_a^b -\frac{lq}{\rho^2} J_q(k_{z_{q,p}}^{Ihc}\rho)[J_l(k_{z_r}^{IIhs}\rho) N_l'(k_{z_r}^{IIhs}b) \\ & - J_l'(k_{z_r}^{IIhs}b) N_l(k_{z_r}^{IIhs}\rho)]\rho d\rho \cdot 2 \int_{\alpha+\theta}^{\pi+\alpha-\theta} \cos q o \sin l(o-\alpha-\theta) do \\ & + P_{q,p}^{(Ihs)} P_{m,r}^{(IIhs)} \int_a^b J_q'(k_{z_{q,p}}^{Ihc}\rho)[J_l'(k_{z_r}^{IIhs}\rho) N_l'(k_{z_r}^{IIhs}b) \\ & - J_l'(k_{z_r}^{IIhs}b) N_l'(k_{z_r}^{IIhs}\rho)]\rho d\rho \cdot 2 \int_{\alpha+\theta}^{\pi+\alpha-\theta} \sin q o \cos l(o-\theta) do \end{aligned} \tag{G.9}$$

where $l = \frac{m\pi}{(\pi-2\theta)}$

$$L_{hh}^{sc}(x,y) = \left(\sum_{n=1}^{N1c} Term_7 + \sum_{m=0}^{N2c} Term_8\right)\sqrt{\frac{k_z^{Ihs}(x)}{k_z^{IIhc}(y)}} \tag{G.10}$$

$$\begin{aligned} Term_7 = \; & P_{q,p}^{(Ihs)} P_{n,r}^{(IIhc)} \\ & \cdot \left(\int_0^a \frac{nq}{\rho} J_q(k_{z_{q,p}}^{Ihs}\rho) J_n(k_{z_r}^{IIhc}\rho) d\rho \int_\alpha^{2\pi+\alpha} -\sin q o \cos n(o-\alpha) do \right. \\ & \left. + J_q'(k_{z_{q,p}}^{Ihs}\rho) J_n'(k_{z_r}^{IIhc}\rho)\rho d\rho \int_\alpha^{2\pi+\alpha} \cos q o \sin n(o-\alpha) do \right) \end{aligned} \tag{G.11}$$

$$\begin{aligned} Term_8 \;=\; & P_{q,p}^{Ihs} P_{m,r}^{IIhc} \int_a^b \frac{lq}{\rho^2} J_q(k_{c_{q,p}}^{Ihs}\rho)[J_l(k_{c_r}^{IIhc}\rho)N_l'(k_{c_r}^{IIhc}b) \\ & -J_l'(k_{c_r}^{IIhc}b)N_l(k_{c_r}^{IIhc}\rho)]\rho d\rho \cdot 2\int_{\alpha+\theta}^{\pi+\alpha-\theta} \sin q\phi \sin l(\phi-\alpha-\theta)d\phi \\ & +P_{q,p}^{(Ihs)} P_{m,r}^{(IIhc)} \int_a^b J_q'(k_{c_{q,p}}^{Ihs}\rho)[J_l'(k_{c_r}^{IIhc}\rho)N_l'(k_{c_r}^{IIhc}b) \\ & -J_l'(k_{c_r}^{IIhc}b)N_l'(k_{c_r}^{IIhc}\rho)]\rho d\rho \cdot 2\int_{\alpha+\theta}^{\pi+\alpha-\theta} \cos q\phi \cos l(\phi-\theta)d\phi \qquad \text{(G.12)} \end{aligned}$$

where $l = \frac{m\pi}{(\pi-2\theta)}$